COMPUTATIONAL AND THEORETICAL STUDIES OF METALLIC DUST TRANSPORT IN TOKAMAKS

NOPPARIT SOMBOONKITTICHAI

Submitted in partial fulfilment of the requirements for the degree of Doctor of Philosophy of Imperial College London and for the Diploma of Membership of Imperial College.

Department of Physics
The Blackett Laboratory
Imperial College London
London SW7 2AZ.

May 7, 2015

The copyright of this thesis rests with the author and is made available under a Creative Commons Attribution-Non Commercial-No Derivatives licence. Researchers are free to copy, distribute or transmit the thesis on the condition that they attribute it, that they do not use it for commercial purposes and that they do not alter, transform or build upon it. For any reuse or distribution, researchers must make clear to others the licence terms of this work.

DECLARATION OF ORIGINALITY

I certify that the work in the thesis is my own and the external materials are appropriately referenced.

NOPPARIT SOMBOONKITTICHAI

Abstract

The plasma facing surfaces of the ITER are going to contain beryllium for the first wall and tungsten for the divertors [1–3]. To test their benefits for the future operations, the JET [1–3] is now run with the ITER-like walls. The ASDEX Upgrade [4–6] has placed full tungsten surfaces inside it, so a large amount of tungsten dust grains are produced. The WEST divertor was recently set up in the Tore-Supra [7,8]. There are some tokamaks which may not use the ITER-like materials but still metal, e.g. the FTU. Also the diagnostic tool [22] can provide metallic dust grains in a chamber. With the high heat output of the future metallic tokamaks, much more metallic dust grains should be produced, the situation of which never occurs.

We focus on studying two phenomena related to metallic dust grains in a plasma: the avalanche erosion done by high velocity impacts; and the misty plasma physics for charged droplet and bubble. For the former, we use the dust transport code, DTOKS [9–13] to simulate iron dust grains re-entering the plasma, corresponding to the FTU, from the bottom. We find that only certain ranges of core plasma flow speed, launch direction and initial dust size result in acheiving a high velocity dust grain.

In misty plasma, for a large droplet, we modify the electrostatic stability limit by the use of the MOML theory [42] and the liquid pressure by the use of the conservation of the ion momentum flux. The bubble in the plasma may originate from the boiling molten layer on plasma facing surfaces or the transformation from the superheated droplets. We calculate the bubble electrostatic stability limit by the Lord Rayleigh's approach [53,58–60]. It is surprisingly that the basic instability initiates at $\ell = 3$ rather than $\ell = 2$.

Acknowledgements

My deepest appreciation is for Dr. M. Coppins, who supervised and supported me throughout my postgraduate study at Imperial College London in every possible ways. He did not only teach me physics but also welfare. Many thanks to Prof. J.E. Allen and Dr. M. Bacharis for co-supervising throughout my study, to Prof. U. De Angelis for co-supervising the research of high velocity dust grains in a tokamak and to Dr. C.T.N. Willis, Dr. N. Rizopoulou, C. Stavrou, D. Thomas, R. Cameron, J. Gibson and J. Holgate, all of which are the colleagues in the dusty plasma team at Imperial College London for good discussion and also friendship. Many thanks to Dr. S.N. Bland for providing me the good advices during working as a teaching assistant and also the knowledge of wire array Z-pinch. Many thanks to the plasma physics group at Imperial College London for providing me the place to study and do research and also to every people in the research group for friendship. Many thanks to the Royal Thai Government for supporting my postgraduate study in UK. Many thanks to Assoc. Prof. Dr. M.A. Allen, Assist. Prof. Dr. R. Chittaree, Dr. W. Chunwachirasiri, Assoc. Prof. Dr. T. Onjun, Assist. Prof. C. Soankwan and every teachers who taught me in Thailand for supporting me before arriving in UK for the postgraduate study. Many thanks to T. Deesuwan, S. Ponglertsakul, E. Pongophas, Dr. C. Puncreobutr, S. Aiemkong, C. Usaku, P. Wongsureerat, Dr. W. Chaisaklert, T. Chanwimalueang, Dr. P. Charoen, Dr. J. Dejvises, Dr. P. Kaewpet, Dr. K. Segkhoonthod, Dr. T. Thongkamwitoon, Dr. P. Watcharapichat, O. Ariyarit, H. Chenboonthai, K. Jongjairuksa, N. Rujeerapaiboon, T. Phairatana, C. Puchongkawarin, N. Srimongkolpithak, A. Teppitaksak and every friends of mine for supporting me and also for friendship. Finally, my deepest appreciations are for my parent, S. Somboonkittichai and T. Supsinmunkong, and my family for supporting and taking care of me throughout my life.

Contents

Abstract **2**

Acknowledgements **3**

1 INTRODUCTION TO DUST IN TOKAMAKS **12**

1.1 Macroparticles in tokamaks 12

1.2 Dust transport code, DTOKS 17

2 HIGH VELOCITY DUST **22**

2.1 Introduction to high velocity dust grains 22

2.2 DTOKS simulation set-ups 24

2.3 Results and discussions 27

2.4 Conclusions 34

3 INTRODUCTION TO MISTY PLASMAS **35**

3.1 Classic electrostatic breakup of a charged droplet 35

3.1.1 Rayleigh's linear stability analysis 36

3.1.2 Laboratory observations 58

3.2 Electrostatic breakup of a charged droplet in a misty plasma 59

3.2.1 Stability of a small droplet in a plasma 60

3.2.2 Pressures on a small droplet in a plasma 62

Pressure due to surface tension 62

Electrostatic pressure 63

Ion and electron pressures 63

Pressure due to neutral recombination 76

4 STABILITY OF A LARGE DROPLET IN A PLASMA **79**

4.1 Validity of Rayleigh's droplet stability limit in a plasma 79

4.2 Derivation 80

4.3 Results 83

4.3.1 Scenario 1: Fusion plasmas in tokamaks 87

4.3.2 Scenario 2: Low pressure plasmas 91

4.3.3 Scenario 3: High pressure plasmas 94

4.4 Discussions and conclusions 97

5 PRESSURE ON A LARGE DROPLET IN A PLASMA **101**

5.1 Derivation of pressures on a large droplet in a plasma 101

5.2 Modified Laplace Equation (MLE) 105

5.3 Results and discussions 106

5.4 Conclusions 111

6 A BUBBLE IN A PLASMA **113**

6.1 A charged bubble in a plasma 113

6.2 Electrostatic stability limit of a charged bubble in a plasma 114

6.3 Results and discussions 117

6.4 Conclusions 126

7 FUTURE WORK **127**

A Symbols **140**

B Abbreviations **144**

List of Figures

2.1 The simple picture showing the FTU where the thick blue line shows its poloidal cross-section and the thick red line shows its toroidal cross-section. The picture is drawn by N. Somboonkittichai. 24

2.2 The picture shows the projections of the FTU shown in figure 2.1 in terms of (a) the poloidal cross-section and (b) the toroidal cross-section. R_0 is a major radius measured from the centre of torus while r_w and r_a are minor radii of the wall and LCMS positions measured from the centre of the circular poloidal chamber. The picture is drawn by N. Somboonkittichai. 24

2.3 The simple picture illustrates the model plasma toroidal velocity, $v_{p,\phi}$, against the minor radius, r, of the FTU. The picture is drawn by N. Somboonkittichai. 27

2.4 The picture shows the probabilities for dust grains to acquire high velocity (1 km/s) varied with the poloidal angle (θ). The core plasma flow speed (v_0) and initial dust size are 100 km/s and 1.0 μm. The dust-wall collision is characterized by isotropic COR, $\epsilon = 1.0$ and 0.7. 28

2.5 The picture shows the probabilities obtaining high velocity varied with core plasma flow velocity (v_0) for dust grains with the initial dust size 0.1 μm. The pictures provide the trends of Class 1, (a) isotropic COR and (b) normal COR and Class 2, (c) isotropic COR and (d) normal COR. 29

2.6 The picture shows the probabilities obtaining high velocity varied with core plasma flow velocity (v_0) for dust grains with the initial dust size 1.0 μm. The pictures provide the trends of Class 1, (a) isotropic COR and (b) normal COR and Class 2, (c) isotropic COR and (d) normal COR. 29

2.7 The picture shows the probabilities obtaining high velocity varied with core plasma flow velocity (v_0) for dust grains with the initial dust size 10.0 μm. The pictures provide the trends of Class 1, (a) isotropic COR and (b) normal COR and Class 2, (c) isotropic COR and (d) normal COR. 30

2.8 The pictures show the final velocity of dust grains varied by the launch angle (γ) for v_0 = 100 km/s where (a) is for the initial dust size 1.0 μm and (b) is for the initial dust size 10.0 μm. 31

2.9 The pictures shows (a) the dust trajectories in plasmas which have v_0 = 20, 100, 180 km/s and the time evolutions of (b) the dust radius and (c) the dust velocity where the initial dust size is 1 μm. All dust grains are injected in $\gamma = 50^\circ$ and collide with the wall by $\epsilon = 0.8$. 32

2.10 The figure shows (a) the trajectories of 1-μm dust grains represented (1) $\gamma = 20^\circ$, (2) $\gamma = 48^\circ$, (3) $\gamma = 120^\circ$ and (4) $\gamma = 165^\circ$ and the associate time evolution of (b) the dust radius and (c) the dust velocity. The plasma has v_0 = 100 km/s and the dust-wall collisions is controlled by $\epsilon = 0.6$. 33

2.11 The figure shows (a) the trajectories of 10-μm dust grains represented (1) $\gamma = 20^\circ$, (2) $\gamma = 38^\circ$, (3) $\gamma = 120^\circ$ and (4) $\gamma = 165^\circ$ and the associate time evolution of (b) the dust radius and (c) the dust velocity. The plasma has v_0 = 100 km/s and the dust-wall collisions is controlled by $\epsilon = 0.6$. 33

3.1 The picture simply illustrates the main features during an electrostatic breakup of a charged droplet in a vacuum. The picture is drawn by N. Somboonkittichai. 59

3.2 The above picture simply illustrates a droplet surrounded by a collisionless plasma where r_d is a droplet radius, R is the position where the droplet electric field is negligible and v, v_r and v_ϕ are the velocity of a plasma particle and its components, i.e. in the radial (r) and azimuthal (ϕ) direction, respectively. The lower picture shows velocity space at the position R where v_1 and v_2 are two examples of particle velocities in the three dimensions. v_r, v_ϕ and v_θ are the speed in the radial (r), azimuthal (ϕ) and polar (θ) directions. The pictures are drawn by N. Somboonkittichai. 66

3.3 The picture shows the symmetry of $\phi_{crit,min}$ and $\phi_{crit,max}$ around $\phi = 0$, which can be used to reduce the work on the integration, i.e. $\int_{\phi_{crit,min}}^{\phi_{crit,max}} = 2 \cdot \int_{\phi_{crit}}^{\pi}$. The picture is drawn by N. Somboonkittichai. 70

4.1 The simple picture explaining the main features on the electrostatic breakup of a charged droplet *in a vacuo*. (This picture is drawn by N. Somboonkittichai.) 81

4.2 The simple picture explaining the main features on the electrostatic breakup of a charged droplet in a misty plasma. (This picture is drawn by N. Somboonkittichai.) 82

4.3 The plot between the ratio of ϕ_d and T_e (T_e in eV unit) and β by the OML (——) and MOML (-·-·-) charging model for hydrogen (H), argon (Ar) and xenon (Xe) plasmas. 84

4.4 The plot between the ratio of ϕ_d and T_e (T_e in eV unit) and atomic mass number (A) by the OML (——) and MOML (-·-·-) charging model for $\beta =$ 0.01, 0.1, 1.0, and 5.0. 84

4.5 Plots of $r_{d,min}$ against T_e under the conditions of fusion plasmas in tokamaks ($\beta =$ 0.1, 1.0, 2.5 and 5.0, deuterium (D) plasma, $n = 10^{18}, 10^{20}$, and $10^{22}\, m^{-3}$) for some well-known plasma facing materials: tungsten (W); iron (Fe); beryllium (Be); and lithium (Li) and the charging models: OML (——); and MOML (-·-·-) and also the plots of Debye lengths (λ_D), corresponding to $n = 10^{18}$ (——), 10^{20} (-·-·-), and 10^{22} (- - -) m^{-3} and T_e. 90

4.6 Plots of $r_{d,min}$ against T_e under the conditions of low temperature and density plasmas ($\beta =$ 0.01, hydrogen (H), nitrogen (N), argon (Ar), and xenon (Xe) plasmas, $n = 10^{12}, 10^{14}$, and $10^{16}\, m^{-3}$) for some low surface-tension materials: water; ethanol; and n-hexane and the charging models: OML (——); and MOML (-·-·-) and also the plots of Debye lengths (λ_D), corresponding to $n = 10^{12}$ (——), 10^{14} (-·-·-), and 10^{16} (- - -) m^{-3} and T_e. 93

4.7 Plots of $r_{d,min}$ against T_e under the conditions of a high pressure plasma represented by plasma spraying, ($\beta = 0.1$, hydrogen (H), nitrogen (N), oxygen (O), and argon (Ar) plasmas, $n = 10^{23}$, and $10^{25}\, m^{-3}$) for some coating materials: molybdenum (Mo); chromium (Cr); aluminium oxide (Al_2O_3); and silicon oxide (SiO_2) and the charging models: OML (——); and MOML (-·-·-) and also the plots of Debye lengths (λ_D), corresponding to $n = 10^{23}$ (——), and 10^{25} (- - -) m^{-3} and T_e. 96

5.1 The figure shows the trends of liquid pressures when the droplets allow evaporation, where the tungsten (W), beryllium (Be), lithium and n-hexane droplets are in the plasma of $n = 10^{16}$ m^{-3} and $T_e = 1 - 1000$ eV. The solid lines correspond to OML. The dashed lines correspond to MOML. 108

5.2 The figure shows the trends of liquid pressures when the droplets allow evaporation, where the tungsten (W), beryllium (Be), lithium and n-hexane droplets are in the plasma of $n = 10^{20}$ m^{-3} and $T_e = 1 - 1000$ eV. The solid lines correspond to OML. The dashed lines correspond to MOML. 109

5.3 The figure shows the trends of liquid pressures when the droplets allow evaporation, where the tungsten (W), beryllium (Be), lithium and n-hexane droplets are in the plasma of $n = 10^{24}$ m^{-3} and $T_e = 1 - 1000$ eV. The solid lines correspond to OML. The dashed lines correspond to MOML. 110

6.1 The plots of a critical radius ($r_{d,crit}$) of a charged tungsten (W) bubble and mode number (ℓ) of the surface perturbation in hydrogen (H^+) plasma with $\beta = 1.0$, $T_e = 10.0, 100.0, 1000.0$ and 10000.0 eV and plasma number density ($n_i = n_e = n$) = 10^{13}, 10^{16}, 10^{19}, 10^{22} and 10^{25} m^{-3}. 120

6.2 The plots of a critical radius ($r_{d,crit}$) of a charged iron (Fe) bubble and mode number (ℓ) of the surface perturbation in hydrogen (H^+) plasma with $\beta = 1.0$, $T_e = 10.0, 100.0, 1000.0$ and 10000.0 eV and plasma number density ($n_i = n_e = n$) = 10^{13}, 10^{16}, 10^{19}, 10^{22}. and 10^{25} m^{-3} 121

6.3 The plots of a critical radius ($r_{d,crit}$) of a charged beryllium (Be) bubble and mode number (ℓ) of the surface perturbation in hydrogen (H^+) plasma with $\beta = 1.0$, $T_e = 10.0, 100.0, 1000.0$ and 10000.0 eV and plasma number density $(n_i = n_e = n) = 10^{13}$, 10^{16}, 10^{19}, 10^{22}. and 10^{25} m^{-3} 122

6.4 The plots of a critical radius ($r_{d,crit}$) of a charged lithium (Li) bubble and mode number (ℓ) of the surface perturbation in hydrogen (H^+) plasma with $\beta = 1.0$, $T_e = 10.0, 100.0, 1000.0$ and 10000.0 eV and plasma number density $(n_i = n_e = n) = 10^{13}$, 10^{16}, 10^{19}, 10^{22}. and 10^{25} m^{-3} 123

6.5 The plots of a critical radius ($r_{d,crit}$) of a charged n-hexane (C_6H_{14}) bubble and mode number (ℓ) of the surface perturbation in hydrogen (H^+) plasma with $\beta = 1.0$, $T_e = 10.0, 100.0, 1000.0$ and 10000.0 eV and plasma number density $(n_i = n_e = n) = 10^{13}$, 10^{16}, 10^{19}, 10^{22} and 10^{25} m^{-3}. 124

6.6 The plots of a critical radius ($r_{d,cri}$) of a charged n-hexane (C_6H_{14}) bubble and mode number (ℓ) of the surface perturbation in hydrogen (H^+), argon (Ar^+) and xenon (Xe^+) plasmas with $\beta = 1.0$, $T_e = 10.0$ and 100.0 eV and plasma number density $(n_i = n_e = n) = 10^{13}$ and 10^{25} m^{-3}. 125

List of Tables

2.1 The plasma parameters used in the DTOKS simulation of high velocity dust grains corresponding to ref. [48–50] 25

4.1 The values of surface tension (σ) of various droplet materials at given droplet temperatures (T_d) 87

4.2 The set-up parameters of the fusion plasmas for scenario 1 in section 4.3.1 88

4.3 The approximated electron temperature (T_e) ranges for charged droplets are stable with the various ratio of ion and electron temperatures (β) 89

4.4 The set-up parameters of the low pressure plasmas for scenario 2 in section 4.3.2 91

4.5 The set-up parameters of the high pressure plasmas for scenario 3 in section 4.3.3 [76–78] 94

4.6 Summary the appropriate use of charging models in various scenarios 97

5.1 The set-up parameters of the works shown in figures 5.1-5.3 106

6.1 The set-up parameters of the works shown in figures 6.1-6.5 118

Chapter 1

INTRODUCTION TO DUST IN TOKAMAKS

This chapter is going to review what macroparticles in tokamaks are and how they affect the efficiency and safety of tokamak operations. The details are in section 1.1 Furthermore, a review of the dust transport code, DTOKS [9–13], used in all of the related studies in this works is provided in section 1.2.

1.1 Macroparticles in tokamaks

In a tokamak, a magnetically confined fusion (MCF) reactor, although the complex magnetic field confines the hot fusion plasma, heat and plasma particles still escape. This is because various phenomena, mainly related to various plasma instabilities, initiate heat transport towards plasma facing surfaces. Radiation and plasma transport [14] are possible ways to carry the heat towards these surfaces. They then erode the inner-wall surfaces through plasma surface interactions. Dust grains represent impurity macroparticles produced from the erosion of plasma facing surfaces. Wall erosion, which directly results in dust generation can be produced by a plasma disruption, ELMs (edge localized modes), unipolar arcs and vertical instabilities.

A plasma disruption [14, 15] leads to the end of tokamak operations, and deposits the plasma energy on the plasma facing surfaces and induce the heavy erosion (see ref. [16] and its figures 2 and 3 for the plasma-disruption-equivalent erosion performed by electron

beam in the experimental simulation). This occurs together with the decrease in plasma current. This results from the increase in the resistance of the fusion plasma due to the decrease in the plasma temperature. Then it results in the difficulty to preserve the discharge due to the fact that the high plasma resistance cannot be compensated by the limited power input.

Edge localized modes (ELMs) [14, 15] are periodic heat and hot plasma particle ejections from the dense core plasma inside an edge transport barrier acheiving in the ELMy high confinement mode (H-mode). They result in heat reaching plasma facing surfaces. ELMs may be initiated by the great pressure gradient in an edge transport barrier. They transport energy from the core towards the plasma facing surfaces, and can be energetic enough to destroy the plasma facing surfaces at e.g. the first wall, limiter and divertor. The most serious surface erosion results from Type I ELMs, the largest periodic expulsions of a core energy compared with Type II and III ELMs [17]. This is because Type I ELMs carry up to one-tenth of the energy stored in the core plasma [17] and subsequently this leads to the heaviest surface erosion compared to the other ELM types.

The vertical instability [14] causes the whole core plasma to move from the proper position upwards and then erode the upper tiles inside the tokamak.

To produce an unipolar arc [14,15], we require a large sheath electric field produced around roughness spots on plasma facing surfaces. A roughness spot creates such an electric field because the curvature of the spot is much higher than that of the plane. This leads to the fact that the roughness of a surface increases the surface area. However, the surface charges configure themselves to produce an equipotential over the rough surface. Thus a non-uniform sheath electric field is set up. The spot is ohmically heated due to the strong electric field and thermally emits electrons [14]. Furthermore, the strong electric field results in the field electron emission through quantum tunneling [14]. Combined with the discharge environment in an edge tokamak plasma, the two electron emission processes eventually lead to the strong incoming currents which later erode the surfaces at the spots. Figure 22 in ref. [15] is recommended for the summary of the main features of an unipolar arc. Furthermore, ref. [18–21] are recommended for the observations of the actual arc traces on the plasma facing surfaces in ASDEX Upgrade and DIII-D. It is noticeable that arc elongated marks are the sets of arc craters and the propagation is produced by the

effect of magnetic force on the arc current and the parallel magnetic field (see Figure 22 in ref. [15]).

The examples of plasma surface interactions mentioned above are directly related to the nature of impurity production via the heat flux depositing on plasma facing surfaces. The heat flux produces several kinds of impurities, e.g. sputtered ions, atoms and molecules and macroparticles, i.e. solid dust grains and molten droplets, and also initiate recycling and loss processes [14, 15]. These multiple forms of impurities can interchange their phase or appearances, determined by the spatially varying conditions in the background fusion plasma.

Sputtered impurity gases can redeposit [22], plasma facing surfaces and the surfaces of diagnostic tools. The thin films so formed are termed redeposited (depositing on the different material surfaces) or self-deposited (depositing on the same material surfaces). If the surface is hot, thermal effects can loosen the thin films causing them to flake. This process is expected to be responsible for the thin and elongated dust generation.

Thermal effects and sublimation [23, 24] can directly produce solid dust grains ejecting into the tokamak chamber, which can occur if the plasma facing surface is carbon. The associated processes are called brittle destruction, resposible for the production of large carbon dust grains, and sublimation, resposible for the production of small carbon dust grains [23, 24]. (See figure 1 in ref. [24].) The reason for this results from the fact that there is no melting of the carbon material. Therefore, sublimation dominates the production of small dust grains. Moreover, the thermal stress then causes the crack and breakup the carbon material directly and subsequently produce large dust grains.

The accumulation of impurity free vapour particles can be initiated if the impurity vapour is saturately dense. Solid carbon dust grains can be produced from the accumulation of many carbon molecules, for instance the form of a chain cluster [22, 25, 26].

It is also possible to form a material compound dust grains, e.g. tungsten dust grains mixed with carbon and boron found in the ASDEX Upgrade reported in [27] and its figure 2 and hydrocarbon dust grains found in TEXTOR-94 [22, 25].

In this thesis, we choose to focus on metallic materials as the plasma facing surfaces which allow melting and boiling. They can be melted, generating molten layers, and also boiled. As a result, liquid molten droplets are released. (See figure 1 in ref. [24]) For instance,

figure 2 in ref. [28] clearly shows molten layers produced by the heat flux, the energy of which is on the order of that of the ELMs, and cracks produced by thermal stress. With the help of some effects, e.g. various forces and interface instabilities, the droplets may scatter from molten layers and molten droplets can travel into a fusion plasma. Depending on the condition of a fusion plasma, molten droplets can solidify near the edge of the core, i.e. near a last closed magnetic surface (LCMS), in a scrape-off layer (SOL) and at plasma facing surfaces. However, solid metallic particles, whether produced by solidification of molten droplets or expelled directly from the wall a solid dust grain, can melt in the plasma. Deeper than the LCMS, the molten droplets keep their liquid phase and travel until going back to the edge region or the end of the tokamak operation. At the end of tokamak operation, all droplets solidify. The dust grains used to be liquid droplets will exhibit spherical shape, due to surface tension, which keeps the droplet to be at the smallest surface area for the given volume i.e. a sphere. This results in the production of metallic spherical dust grains. The observation of spherical dust grains indicate that molten droplets occur in fusion plasmas.

Dust grains can be collected by a probe collector, a vacuum machine and even binding tape. The dust size distribution is analysed. The size distribution is varied in different tokamaks, which may have different properties of inner surface materials. Since this thesis emphasizes on metallic dust grains, we highlight the tungsten dust grains collected in the ASDEX Upgrade reported in N. Endstrasser *et al* (2011) [5]. The tungsten dust size distribution can be seen in figures 3 and 4 in N. Endstrasser *et al* (2011) [5]. Ref. [5] also reported that the average diameters of the tungsten spherical dust grains and the tungsten flake-like dust grains are 1.7-2.2 μm and 0.2-0.6 μm for the 2007-2009 ASDEX Upgrade operations. In addition, the quantity of collected spherical dust grains is much less than that of the collected flake-like dust grains. In chapter 3, we consider the role of misty plasma effect in determining the size distribution of spherical metal particles.

In practice, after the end of each tokamak operation, we can observe and collect dust grains for further analysis from the bottom of the tokamak chamber. Nearly all solid dust grains end up there because they fall under gravity. (See figure 2 in ref. [29] for dust concentration analysis conducted in ASDEX-Upgrade) Unfortunately, in general we can know the size distribution of collected dust grains but not that of initial wall-released dust grains. Thus it is difficult to determine the accurate initial condition for dust simulations.

Dust grains affect the efficiency of the tokamak operations. They also affect the safety of the operations because they are potentially harmful to humans and the environment in certain ways. These generally depend on the size, the concentration and the penetration property of the leftover dust grains in tokamak chambers, all of which govern the total surface area. To show this, some critical situations for illustrating how serious dust issues are for tokamak operations is given below.

Chemical reactions with certain substrates can initiate explosive events. We give two classic examples. Beryllium dust grains can react with water leaking from the cooling system and to produce beryllium-oxide (BeO), which is dangerous to humans because it is toxic, and hydrogen gas (H_2), which can damage the tokamak chamber because of explosion [30, 31]. Dust explosion, which happens via a reaction with air penetrating into a tokamak chamber, may also occur at a certain concentration of accumulated dust grains and energy [31].

Fuel retention on dust grains is another significant problem. Deuterium and tritium can deposit on not only on plasma facing surfaces [32–34] but also dust grains [31,35]. This enhances the loss of fuel because of an increase in a surface area of plasma interacting surfaces. Furthermore, an even more serious problem arises with regard to the loss of tritium. Tritium is expensive because it is rare in nature because of its short half-life and it has to be produced through the lithium-neutron reaction, which is designed to be taken place on the surfaces of the tritium-breeding blanket [14]. In addition, losing tritium to dust grains, especially if the dust grains have carbon [31, 34], initiates a further problem regarding a transport of radioactive tritium, into the environment. This is possible when a tokamak chamber is opened for some reasons. Moreover, the problem becomes serious because the sizes of dust grains are relatively small so that they are easily to be blown away from the tokamak chamber.

Radiation cooling can be a serious problem in a fusion plasma. This is caused by impurities originating from plasma facing materials or even helium ions from the nuclear fusion reaction [14]. Dust grains greatly enhance the severity of this problem. Dust grains are significantly mobilized by a plasma flow, i.e. mainly by the ion drag force, the trends of which can be seen in figure 7 in ref. [11] and figures 4 and 8 in ref. [36]. The associated momentum becomes so great that they are driven to go deeper away from their origins. (See

figure 32 in ref. [37] for understanding the impurity deposition profile of dust compared to that of sputtering.) They can pass through the scrape-off layer (SOL), and reach the core plasma. The evaporation on the way deposits impuritiy vapour in the fusion plasma. Eventually, they leads to impurity radiation, which cools down the fusion plasma. The radiation is strong in the SOL if dust grains mainly contain low atomic number materials; however in the core plasma, strong radiation results from high atomic number materials [14], which can be contained in e.g. metallic dust grains. The radiation cooling affects tokamak operations in terms of the initiation of a plasma disruption [14]. The plasma is cooled down by radiation and its electrical resistivity is enhanced. Therefore, it is harder to preserve the suitable plasma temperature, causing by a disruption instability and eventually leading to the operation shut-down. In addition, the remaining energy flows towards plasma facing surfaces generate further extreme erosion.

1.2 Dust transport code, DTOKS

DTOKS is a dust transport code, developed at Imperial College London. In this section, we review and summarise the physical theories underlying the DTOKS code. DTOKS has three main physical models, related to charging, heating and equation of motion with various forces. This is to simulate the motion of dust gains under tokamak plasma conditions. As a result of this, it has to be combined with a plasma background profiles in each tokamak. The review in this section is based on the works of J.D. Martin *et al* [9, 10] and M. Bacharis *et al* [11–13]. Because this section provides the summary of the main physical models used in the DTOKS, ref. [9–13] are recommended for more details and are the main references for the DTOKS review in this section.

The orbital motion limited (OML) theory [38–40] takes care of the charging model, determining the floating potential (ϕ_d) at the steady state. Strictly speaking, OML is only valid if the dust radius (r_d) is much smaller than the Debye length of the plasma (λ_D), $r_d \ll \lambda_D$. However, C.T.N. Willis *et al* [41] have shown that even when the dust radius is close to the Debye length, $r_d \to \lambda_D$, OML theory is still a good approximation for a fully ionized plasma with $T_i = T_e$ (where T_i and T_e are ion and electron temperatures, respectively). This should be satisfied with fusion plasma conditions. However, it is possible that OML is inapplicable if we assume that an initial dust is ejected from plasma facing

surfaces with too large a size (larger than a few tens of μm). Apart from near plasma facing surfaces it is still the good approximation for evaluating ϕ_d by the help of the OML theory. This is because $r_d < \lambda_D \propto \left(\frac{T_e}{n}\right)^{\frac{1}{2}}$. Although the initial dust size is too large, large electron temperature (T_e) as well as large ion temperature (T_i) and plasma number density (n), which can be generally found in a hot fusion plasma, enhances the evaporation rate by a great net energy flux on a dust grain. This reduces the dust size to the OML limtation, $r_d < \lambda_D$, and the condition is appromately fullfilled for most of the dust motion period. Thus, the floating potential evaluation by the OML theory is acceptable. From this, the convenient OML formula for evaluating the floating potential, $\phi_{d,OML}$, of a dust grain in a plama can be written as

$$(1-\delta_{tot})\exp\left(\frac{\phi_{d,OML}}{T_e[eV]}\right) = \sqrt{\frac{\beta m_e}{m_i}}\left(1-\frac{\phi_{d,OML}}{\beta T_e[eV]}\right), \tag{1.1}$$

where $T_e[eV]$ is an electron temperature in the unit of eV, $\beta = \frac{T_i}{T_e}$ is the ratio of ion and electron temperatures, and m_i and m_e are a single ion and electron mass, respectively. Furthermore, it is possible to have addtional electron emissions, so the emission yieid, δ_{tot}, is added to the OML formula seen in eq. 1.1. In the DTOKS, thermionic emission (THE) and secondary emission (SEE) are taken into consideration. If there is no electron emission, $\delta_{tot} = 0$. The OML formula originates from the steady state condition of total currents and also the electron emisson current, $I_{emission}$. In other words,

$$\frac{dQ}{dt} = I_i + I_e + I_{emission} = I_i + (1+\delta_{tot})I_e = 0. \tag{1.2}$$

The ion and electron currents are determined by the OML currents [38–40, 42],

$$I_i = -4\pi r_d^2 n_{i,0} e\sqrt{\frac{kT_i}{2\pi m_i}}\left(1-\frac{e\phi_d}{kT_i}\right) \tag{1.3}$$

$$I_e = 4\pi r_d^2 n_{e,0} e\sqrt{\frac{kT_e}{2\pi m_e}}\exp\left(\frac{e\phi_d}{kT_e}\right). \tag{1.4}$$

The principle of the OML theory [38–40] is to calculate a charge flux or a current density, $j = q\Gamma$, where q is a charge of interest, with an appropriate the cross-section area (A_{cs}) for each type of plasma particles, i.e. ions and electrons, depositing on the dust grain. By this method, the current of ions and electrons, $I = j \cdot A_{cs}$, on a dust grain can be found. The

cross-section area (A_{cs}) can be determined by the use of the conservation law of angular momentum and energy of a single particle motion. The current densities of both plasma species are calculated by the use of the first moment of the Maxwellian distribution function integration, $j = q \int \mathbf{v} f(\mathbf{r}, \mathbf{v}) d^3\mathbf{v}$.

For the DTOKS [9–13], we consider the possible heating and cooling mechanisms at the steady state. In the DTOKS we include two heating mechanisms. First, in a plasma, heating is acheived by the depositions of hot ions and electrons. The ion and electron energy fluxes continuously heat a dust grain with the steady state rate controlled by the floating potential, ϕ_d. For the second heating mechanism, the steady ion and electron currents deposited on the dust surface create addition heat released from the recombination, $2\mathrm{H}^+ + 2\mathrm{e}^- \rightarrow \mathrm{H}_2$, where hydrogen and its isotopes are common fusion fuels. The main cooling mechanisms is the thermal radiation. In addition, there is the cooling by the energy loss acheived by the electron emissions, i.e. thermionic electron emission (THE) and secondary electron emission (SEE), and the backscattering process. The dust temperature (T_d) is evolved by the net energy flux (Ξ_{net}) done by all heating and cooling mechanisms mentioned so far with a time variable (t) because it is not steady state. We can write the heat equation with the dust variables as

$$
\begin{aligned}
Q_{net} &= m_d c \delta T_d && (1.5)\\
\Xi_{net} 4\pi r_d^2 \delta t &= \rho_d \frac{4}{3} \pi r_d^3 \delta T_d && (1.6)\\
\frac{dT_d}{dt} &= \frac{3\Xi_{net}}{\rho_d r_d}, && (1.7)
\end{aligned}
$$

where Q_{net} is a net energy on a dust grain, ρ_d is a density of a main dust material and c is a specific heat capacity. Slow evaporation in a liquid phase is not taken into consideration. However, if the energy flux is enough to rise the temperature of the dust grain to the boiling temperature, then strong evaporation at the boiling temperature occurs. In DTOKS, this is described by the heat equation with the latent heat of vaporization (L_v),

$$
\begin{aligned}
Q_{net} &= \delta m_d L_v && (1.8)\\
\Xi_{net} 4\pi r_d^2 \delta t &= \rho_d 4\pi r_d^2 \delta r_d L_v && (1.9)\\
\frac{dr_d}{dt} &= \frac{\Xi_{net}}{\rho_d L_v}. && (1.10)
\end{aligned}
$$

We fix the values of ρ_d, c and L_v assuming no temperature and pressure variations.

The equation of a dust motion used in the DTOKS [9–13] consists of the influences of a gravitational force, $m_d\mathbf{g}$, an electromagnetic force, $Q_d(\mathbf{E}+\mathbf{v_d}\times\mathbf{B})$ and an ion drag force ($\mathbf{F_{id}}$). The ion drag force generally consists of two conponents originating from different kinds of the momentum transfer between ions and a dust body. We name the "scattered" component of $\mathbf{F_{id}}$, $\mathbf{F_{id,s}}$, if the momentum transfers via the electrostatic scattering between the charged ions and the dust electric field, and the "collected" component of $\mathbf{F_{id}}$, $\mathbf{F_{id,c}}$, if the momentum transfers through the physical depositions of the ions onto the dust body. The simple form of the force equation obeying the second law of the Newtononian mechanics is

$$\frac{d\mathbf{v_d}}{dt} = \mathbf{g} + \frac{Q_d}{m_d}(\mathbf{E} + \mathbf{v_d} \times \mathbf{B}) + \mathbf{F_{id,c}} + \mathbf{F_{id,s}} \, , \tag{1.11}$$

where $\mathbf{v_d}$ is a single dust velocity. In the DTOKS, there is no consideration of electron, impurity and neutral drag forces.

For the heat equations (eq. 1.7 and 1.10) and the dust equation of motion (eq. 1.11), the first-order time-discretized finite difference method is used to solve for the time evolution of the interested dust variables, i.e. T_d, r_d and $\mathbf{v_d}$, which explain the dust motion. For the formula of the OML theory determining the floating potential, ϕ_d (eq. 1.1), we have to use some iteration method to solve the solution, i.e. ϕ_d, because eq. 1.1 is nonlinear. The basic method, which is also used in the DTOKS, is the Newton iteration method [43],

$$\phi_{d,i+1} = \phi_{d,i} - \frac{f(\phi_{d,i})}{f'(\phi_{d,i})}, \tag{1.12}$$

where the subscript i and $i+1$ refer to the current and the next iteration steps. To apply the method to solve for ϕ_d, we have the function

$$f(\phi_d) = (1-\delta_{tot})\exp\left(\frac{\phi_d}{T_e[eV]}\right) - \sqrt{\frac{\beta m_e}{m_i}}\left(1 - \frac{\phi_d}{\beta T_e[eV]}\right) = 0. \tag{1.13}$$

We also need to write its derivative $f'(\phi_d)$ with respect to ϕ_d,

$$f'(\phi_d) = \frac{df(\phi_d)}{d\phi_d} \tag{1.14}$$

$$= \frac{(1-\delta_{tot})}{T_e[eV]} \exp\left(\frac{\phi_d}{T_e[eV]}\right) + \left(\frac{1}{\beta T_e[eV]}\right)\sqrt{\frac{\beta m_e}{m_i}}. \tag{1.15}$$

The calculation of eq. 1.12 combined with $f(\phi_d)$ (eq. 1.13) and its derivative, $f'(\phi_d)$ (eq. 1.15), are iteratively conducted until the values of $\phi_{d,i+1}$ and $\phi_{d,i}$ are not significantly different or differ in some acceptable order.

Chapter 2

HIGH VELOCITY DUST

Several tokamaks, e.g. FTU [44, 45] and HT-7 [46, 47], have reported observations which suggest the presence of dust grains with very high velocities (> 1 km/s). In this chapter, we use DTOKS to explore the conditions necessary for such high velocity particles to occur. In section 2.1, the FTU and HT-7 results are reviewed together with the brief discussion of a serious possible problem associated with these high velocity particles, namely avalanche erosion of plasma facing surfaces. The parameters used in the DTOKS simulations are outlined in section 2.2. Sections 2.3 and 2.4 present the results and discuss their implications.

2.1 Introduction to high velocity dust grains

This section reviews high velocity dust grains and recent observations. Apart from the general problems caused by dust grains, it has been suggested that high velocity dust grains can cause an impact induced avalanche surface erosion [46]. Avalanche erosion would occur if, on average, each high velocity dust grain impact on the wall and produce more than one secondary dust grains, which is subsequently accelerated to high velocity. During a high velocity impact, a crater with liquid molten material is produced by the heat generated during the impact. In other words, a transient melt layer can be formed in the crater. The high velocity dust grain push the liquid out of the crater through its rim. The ejected liquid can become secondary droplets or dust grains. If the new secondary dust grains are accelerated to high velocity later then further erosion happens. This is why this situation is called an avalanche erosion. If this occurs, it represents a desperate problem because it

reduces the quality of the plasma facing surface tiles placed inside the tokamak. This could be a very serious problem for future tokamaks with higher power inputs (e.g. ITER) since the larger amounts of dust grains are produced by the heavier heat loads on plasma facing surfaces.

The dust experiments conducted in the FTU, the tokamak in Italy [44, 45], and the HT-7, the tokamak in China [46, 47] were specifically designed to observe high velocity dust grains. The former has steel walls, the latter carbon. In both experiments, evidence for high velocity dust grains was found. In the experiment conducted in the HT-7 [46, 47], an aerogel receptor was used to collect dust grains. The craters in which the dust grains penetrate have been analyzed, the diameters of the craters related to the speed of the collected dust grains. The analysis suggests the presence of having abnormally high speed dust grains (upto 1 km/s). In contrast, in the experiment conducted in the FTU [44, 45], a probe was placed at the outer-wall equatorial position and used to measure the saturated ion current contributed from impact ionization. The impact ionization results from the collision between a dust grain and the probe. Based on the measurement gathering by the probe, the experiment found that there were spikes of abnormally high ion current on the probe. These current spikes are believed to originate from the high speed impact between dust grains and the probe. Moreover, after performing the surface analysis, it is found that the probe surface exhibits some craters. It is suggested that high speed impacts lead to crater formation and it also supports the existence of high velocity dust grains because the finding suggests that the number of the observed craters and the number of the abnormal high levels of the ion current measured by the probe are satisfied with each other. Furthermore, the further analysis was proceeded in the way of computation done by I. Proverbio *et al* (2011) [48]. The computational study supported the experimental finding of the FTU that it was possible to find high velocity dust grains.

The main factors leading to the production of dust grains are unclear. Therefore, in this thesis, we concentrate on the main factors accelerating dust grains to high speed. Understanding the conditions necessary to accelerate dust grains to high velocity allows us to assess the significance of this phenomenon, for instance whether or not avalanche erosion is likely to be a problem in ITER.

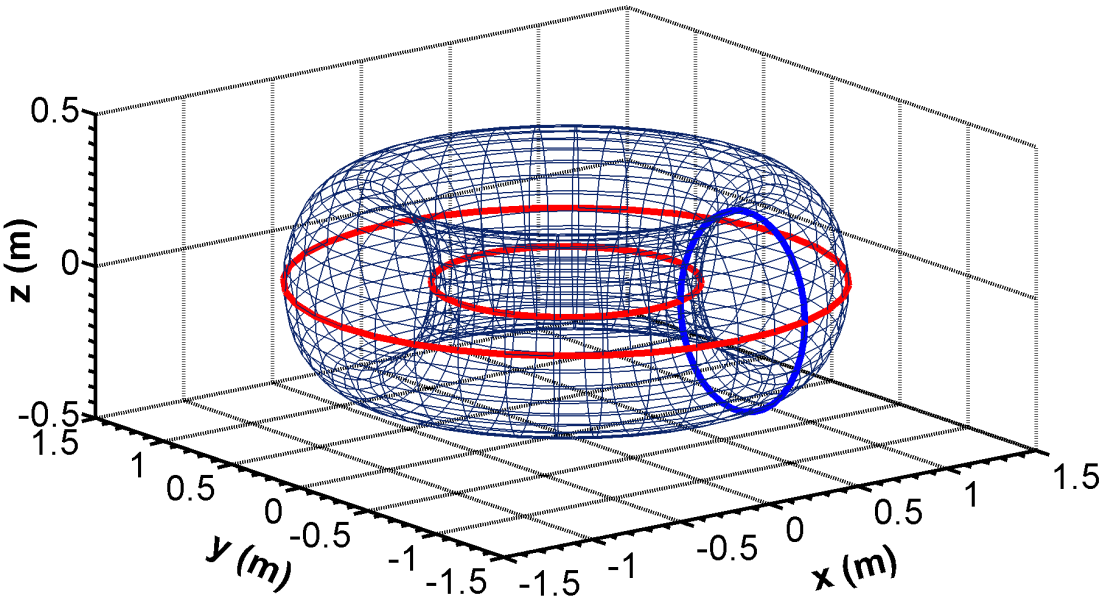


Figure 2.1: The simple picture showing the FTU where the thick blue line shows its poloidal cross-section and the thick red line shows its toroidal cross-section. The picture is drawn by N. Somboonkittichai.

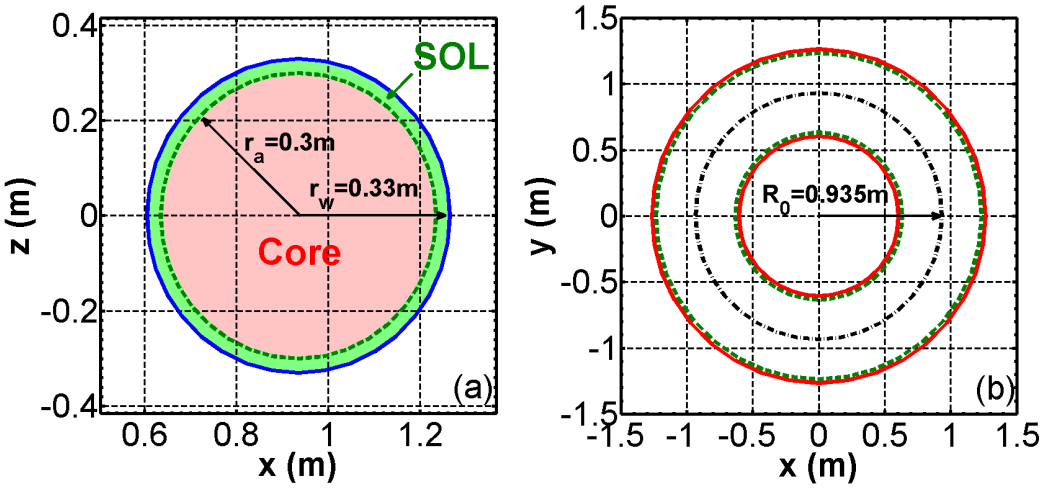


Figure 2.2: The picture shows the projections of the FTU shown in figure 2.1 in terms of (a) the poloidal cross-section and (b) the toroidal cross-section. R_0 is a major radius measured from the centre of torus while r_w and r_a are minor radii of the wall and LCMS positions measured from the centre of the circular poloidal chamber. The picture is drawn by N. Somboonkittichai.

2.2 DTOKS simulation set-ups

We computationally study high velocity dust grains with the dust transport code, DTOKS [9–13]. The review of the code can be found in section 1.2.

The FTU and the HT-7 tokamaks are similar in size and aspect ratio ($\frac{R_0}{r_w}$) where

R_0 is the major radius and r_w is the minor radius (see figures 2.1 and 2.2). The aspect ratios of FTU and HT-7 are 4.5 and 2.8 respectively. The sizes of FTU are $R_0 = 0.935$ m and $r_w = 0.33$ m [45, 48] and the sizes of the HT-7 are $R_0 = 1.22$ m and $r_w = 0.27$ m [46, 47]. In addition, these two tokamaks both have a circular poloidal cross-section. In view of this similarity, we choose our computational tokamak to be FTU. We consider the FTU inner-tokamak iron surfaces as the main dust material because dust grains are produced from the erosion of the main plasma facing surfaces. The iron dust grains move in the tokamak and can interact with the plasma facing surfaces via physical collisions only. The momentum change during each collisions are simply characterised by the coefficient of restitution (COR), categorized in two types: the coefficient of normal restitution, the ratio of normal velocities ($v_\perp$) after and before a collision, $\epsilon_n = \frac{v_{\perp,after}}{v_{\perp,before}}$; and the coefficient of an isotropic restitution, the ratio of speeds (v) after and before a collision, $\epsilon = \frac{v_{after}}{v_{before}}$. We use the simple dust-wall collision characterization via ϵ and ϵ_n to model what are actually extremely complicated dust-wall interaction. For instance, the walls of tokamaks have limiters, divertors and diagnostic tools. We neglect the geometries of those instruments and just use a simple toroidal wall with a perfect circular poloidal cross-section. The simple geometry is shown in figures 2.1 and 2.2. As can be seen in figure 2.2, we define an effective scrape-off layer (SOL) at the position outwardly beyond $r > r_a = 0.3$ m although we do not apply the limiter configuration in the simulation.

Table 2.1: The plasma parameters used in the DTOKS simulation of high velocity dust grains corresponding to ref. [48–50]

Major radius, R_0	0.935 m
Minor radius at LCMS, r_a	0.3 m
Minor radius at the wall, r_w	0.33 m
Minor radius for $E_r = 0$, r_0	0.295 m
Temperature decay length, λ_T	0.03
Number density decay length, λ_n	0.02
Central plasma temperature, T_0	2.0×10^3 eV
LCMS plasma temperature, T_a	30 eV
Central plasma number density, n_0	1.0×10^{20} m^{-3}
LCMS plasma number density, n_a	4.0×10^{18} m^{-3}
Central toroidal magnetic field, B_0	7.0 T
LCMS poloidal magnetic field, B_a	0.24 T
Peak value of radial electric field in core plasma, E_0	6.0×10^3 V/m
Peak value of radial electric field in SOL plasma, E_a	3.0×10^3 V/m

The plasma conditions in our study are adopted from the core and SOL steady state radial functions of the FTU's plasma temperature, $T(r)$, plasma number density, $n(r)$, radial electric field, $E_r(r)$, and magnetic field in both toroidal, $B_\phi(R)$, and poloidal, $B_\theta(r)$, directions, which are already provided in ref. [48,49] and also with the communication [50]. We also assume $T(r) = T_i(r) = T_e(r)$ and $n(r) = n_i(r) = n_e(r)$ everywhere. We refer to ref. [48–50] as the main references of the FTU plasma conditions used in this study and for the further details. The forms of the plasma background functions [48–50] mentioned above are

$$T(r) = \begin{cases} T_0\left(1-\zeta_a^2\right)^{1.5} + T_a, & \zeta_a \le 1, \\ T_a \exp\left(\frac{1-\zeta_a}{\lambda_T}\right), & \zeta_a > 1, \end{cases} \tag{2.1}$$

$$n(r) = \begin{cases} n_0\left(1-\zeta_a^2\right)^{0.75} + n_a, & \zeta_a \le 1, \\ n_a \exp\left(\frac{1-\zeta_a}{\lambda_n}\right), & \zeta_a > 1, \end{cases} \tag{2.2}$$

$$E_r(r) = \begin{cases} 3E_0\left(\frac{4}{3\zeta_0}\right)^4 (\zeta-\zeta_0)\,\zeta^3, & \zeta \le \zeta_0 \\ E_a \frac{4}{(1-\zeta_0)^2}(\zeta-1)(\zeta_0-\zeta), & \zeta > \zeta_0, \end{cases} \tag{2.3}$$

$$B_\phi(R) = \frac{B_0 R_0}{R} \tag{2.4}$$

$$B_\theta(r) = \begin{cases} B_a\left(\frac{1-\left(1-\zeta_a^2\right)^{1.5}}{\zeta_a}\right), & \zeta_a \le 1, \\ \frac{B_a}{\zeta_a}, & \zeta_a > 1. \end{cases} \tag{2.5}$$

Table 2.1 summarises the definitions and values of the plasma parameters used in this study. We also define for this chapter that r is a tokamak minor radius of a position, $\zeta_a = \frac{r}{r_a}$, $\zeta = \frac{r}{r_w}$ and $\zeta = \frac{r}{r_0}$.

We focus on the use of the toroidal plasma flow in the simulation. This is because in general, the toroidal component of the plasma flow is largest. In this work, we use a simple model for the toroidal plasma velocity ($v_{p,\phi}$), as can be seen in figure 2.3,

$$v_{p,\phi} = \begin{cases} v_0 = \text{constant}, & r \le r^*, \\ \frac{v_0(r-r_w)}{(r^*-r_w)}, & r > r^*, \end{cases} \tag{2.6}$$

where v_0 is a central constant velocity and r^* is defined as the velocity drop-point position. With regard to this plasma velocity profile, the velocity in the central region of the fusion plasma is assumed flat. The trend is continuous from the centre of the core plasma to $r = r^*$,

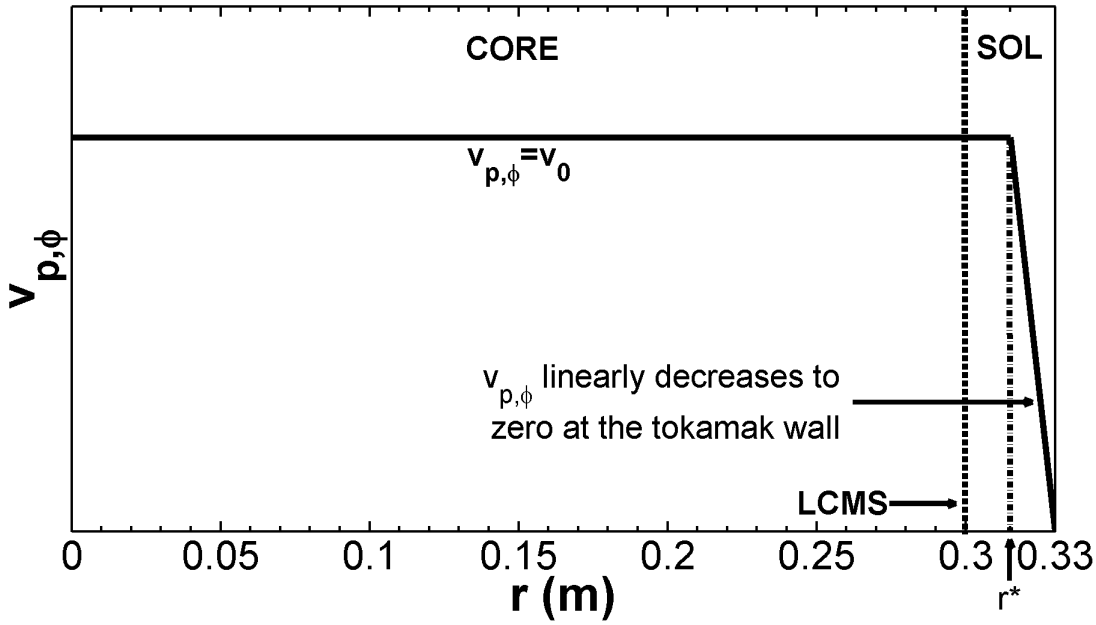


Figure 2.3: The simple picture illustrates the model plasma toroidal velocity, $v_{p,\phi}$, against the minor radius, r, of the FTU. The picture is drawn by N. Somboonkittichai.

in the SOL. Beyond r^*, the plasma velocity linearly decreases to be zero at the tokamak wall. We get two benefits from this plasma velocity model. First, neutral beam injection (NBI) can be used to drive and preserve the plasma rotation and assumed the plasma velocity model (i.e. flat in the core and decreasing to zero at the wall) approximately corresponds to the NBI-induced plasma flow trend (see figure 4 in ref. [51] as an example). Second, as we know from section 1.1 that the ion drag force is the most crucial force in the acceleration of a dust grain in the tokamak flow [11,36]. The plasma flow velocity controls the ion drag force. The velocity profile allows us to characterize the magnitude of the flow by the single parameter v_0. In other words, to adjust the ion drag force, v_0 is only free parameter we need to vary. We choose r^* to be the middle position of the SOL. Varying the position of r^* with in the SOL has little effect on the results.

2.3 Results and discussions

We consider high velocity dust grains, i.e. those which can reach a speed of 1 km/s as the final velocity. The aim of the simulation is to identify the conditions suitable for dust grains to acheive this high velocity. The conditions are characterized through 1) dust launch location, 2) initial dust size, 3) core plasma speed (v_0) and 4) launch direction (γ).

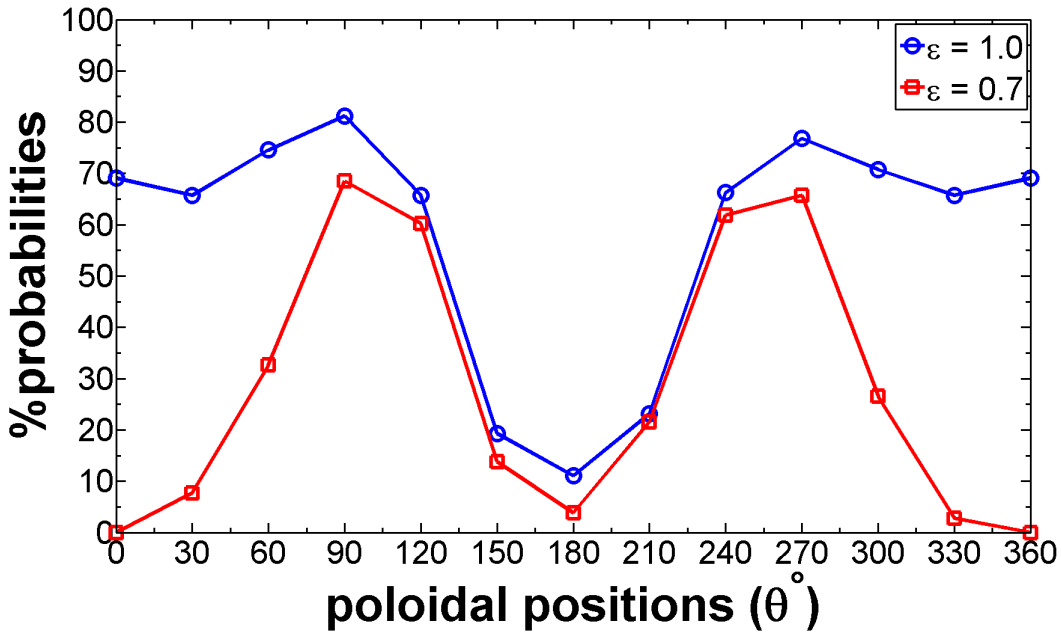


Figure 2.4: The picture shows the probabilities for dust grains to acquire high velocity (1 km/s) varied with the poloidal angle (θ). The core plasma flow speed (v_0) and initial dust size are 100 km/s and 1.0 μm. The dust-wall collision is characterized by isotropic COR, ϵ = 1.0 and 0.7.

We assume that the initial velocity of dust grains from the wall is 10 m/s throughout this section.

Some dust collection experiments, e.g. in TEXTOR-94 [22], ASDEX-Upgrade [27], HT-7 [47] and Tore-supra [52], confirm that the largest concentration of dust grains is located at the bottom. This is due to the effect of gravity. Therefore, we assume that high velocity dust grains originates from the remobilzation of the pre-existence dust grains at the bottom of the tokamak. Moreover, it is usual that limiters and divertors can be placed at the bottom. The heat flux travelling in the SOL can erode the plasma facing surface and produce new dust grains. The assumption of high velocity dust grains moving from the bottom is still reasonable in this case. However, it is crucial to know which poloidal angle (θ) of the tokamak chamber gives the highest probabilities to acquire such high velocity dust grains. The poloidal angle rotates counter-clockwise from $\theta = 0°$ located at the outer-wall equatorial plane. Figure 2.4 shows the probabilities for dust grains to acquire high velocity (1 km/s) varied with the poloidal angle (θ). (see figure 2.4 for the setup detail.) The launch positions giving the highest probabilites are $\theta = 90°$ (top) and 270° (bottom). Therefore, our assumption to launch dust grains from the bottom actually maximizes the probabilities

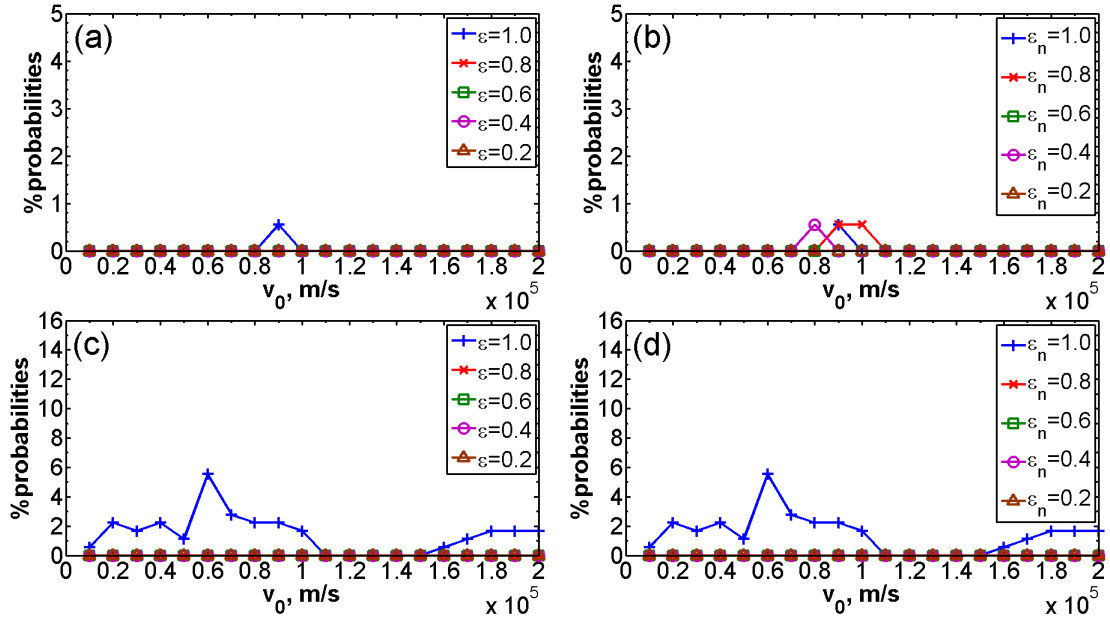


Figure 2.5: The picture shows the probabilities obtaining high velocity varied with core plasma flow velocity (v_0) for dust grains with the initial dust size 0.1 μm. The pictures provide the trends of Class 1, (a) isotropic COR and (b) normal COR and Class 2, (c) isotropic COR and (d) normal COR.

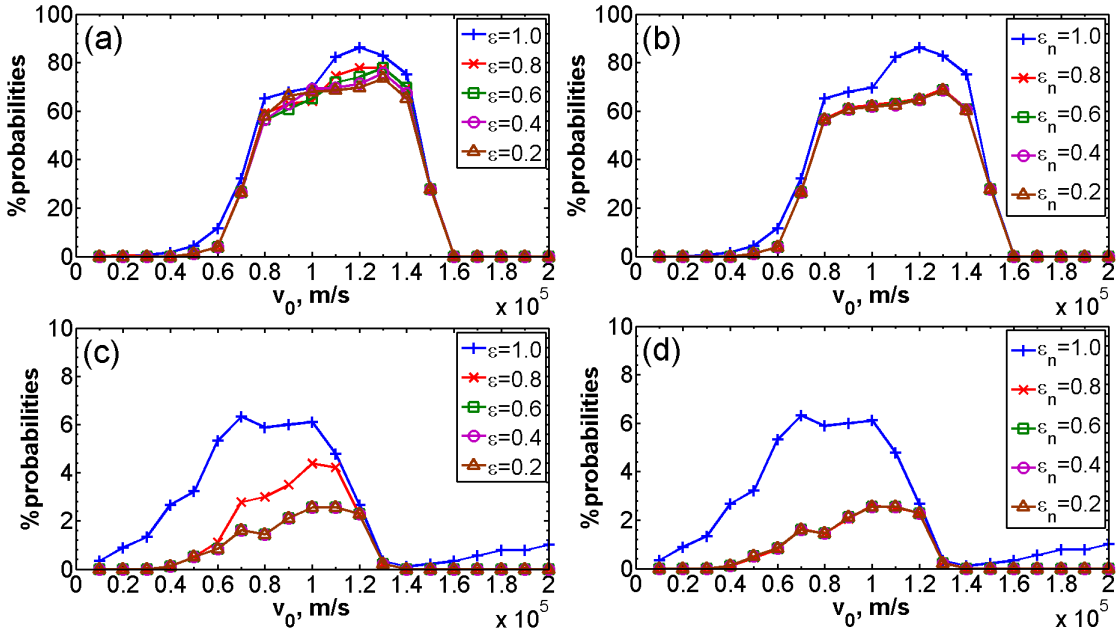


Figure 2.6: The picture shows the probabilities obtaining high velocity varied with core plasma flow velocity (v_0) for dust grains with the initial dust size 1.0 μm. The pictures provide the trends of Class 1, (a) isotropic COR and (b) normal COR and Class 2, (c) isotropic COR and (d) normal COR.

of high velocity being acheived.

Figures 2.5, 2.6 and 2.7 give the probabilities to obtain high velocity dust grains for

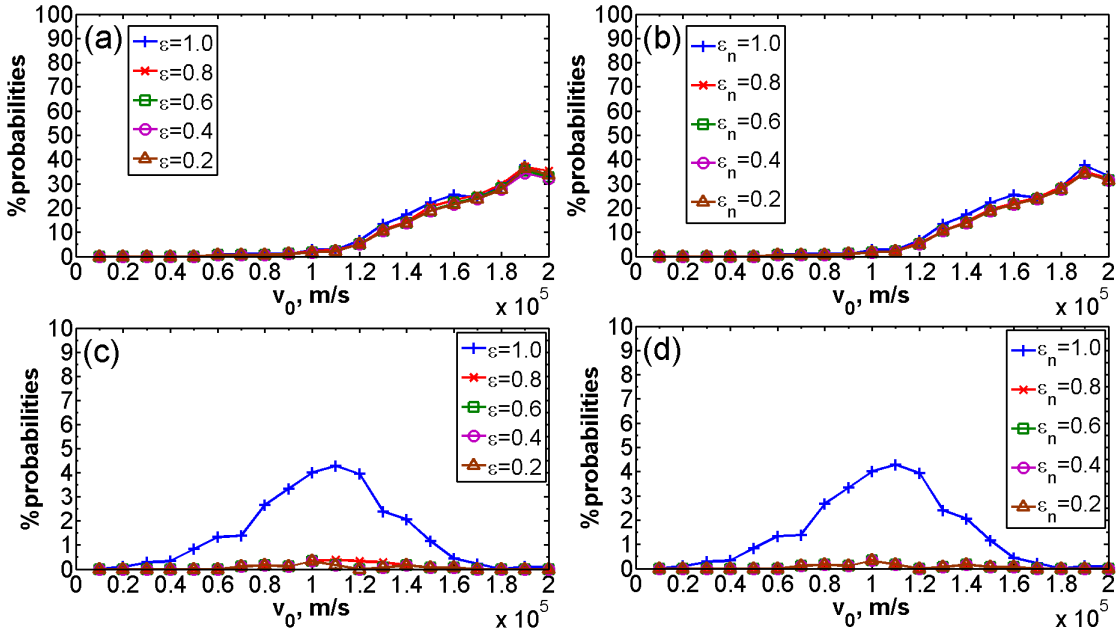


Figure 2.7: The picture shows the probabilities obtaining high velocity varied with core plasma flow velocity (v_0) for dust grains with the initial dust size 10.0 μm. The pictures provide the trends of Class 1, (a) isotropic COR and (b) normal COR and Class 2, (c) isotropic COR and (d) normal COR.

the initial dust sizes 0.1, 1.0 and 10.0 m, respectively. Based on figures 2.5, 2.6 and 2.7, we have to define categories for high velocity dust grains: Class 1 (hitting the wall); and Class 2 (completely evaporating in a plasma). As can be seen on figures 2.5, 2.6 and 2.7, for both Classes, only a certain range of core plasma velocities (v_0) are suitable for dust grains to be accelerated to high velocities. Although it appears that the cases $\epsilon = \epsilon_n = 1.0$ enhances the probabilites, they are not realistic, so we neglect them. For the 0.1 μm dust grains, we cannot obtain both high velocity dust Classes. This is because they are too small to withstand the heat load before they obtain high velocities. In contrast, for the 1.0 μm and 10.0 μm dust grains, they obtains both Classes although the probabilities of both Classes for the 10.0 μm dust grains are much lower. This may be because they are too big, so they are harder to be accelerated. From the figures, we see that the most appropriate dust size should be in an order of 1 μm which gives the highest probabilities to obtain both Classes. We are interested in only Class 2 dust grains because they can be observed at the wall and can hit the wall so that erosion may happen. The most suitable v_0 range for obtaining Class 2 dust grains for both types of COR is 40-130 km/s where the best v_0 is 100 km/s. Hence, only a narrow range of v_0 and initial dust size allows us to obtain the Class 2 dust grains.

Figure 2.8 is plotted to determine the suitable range of launching direction (γ) at the bottom for dust grains to acheive the velocity of 1 km/s. The angle γ is varied from 0° (outward direction) to 180° (inward direction). At this point, we extend Class 1 and Class 2 into 2 subclasses namely primary and extra. Class 1 primary means obtaining 1 km/s but completely evaporating, and Class 1 extra means obtaining 1 km/s after hitting with the wall but then completely evaporating. Class 2 primary means obtaining 1 km/s before hitting the wall for the first time, and Class 2 extra means obtaining 1 km/s after hitting with the wall at least once, subsequently hitting the wall again. Figure 2.8 shows only the primary subclass for both Classes because we do not consider dust-wall collisions for this figure. We consider $v_0 = 100$ km/s and initial dust sizes of 1.0 μm and 10.0 μm. It is clearly seen that using the initial dust size 1.0 μm enlarges the ranges of γ wider than those of the initial dust size 10.0 μm for both Class 1 primary (highlighted by the yellow color) and Class 2 primary (highlighted by the blue color). Therefore, without assuming dust-wall collisions, we can get high velocity dust grains before hitting the wall (Class 2

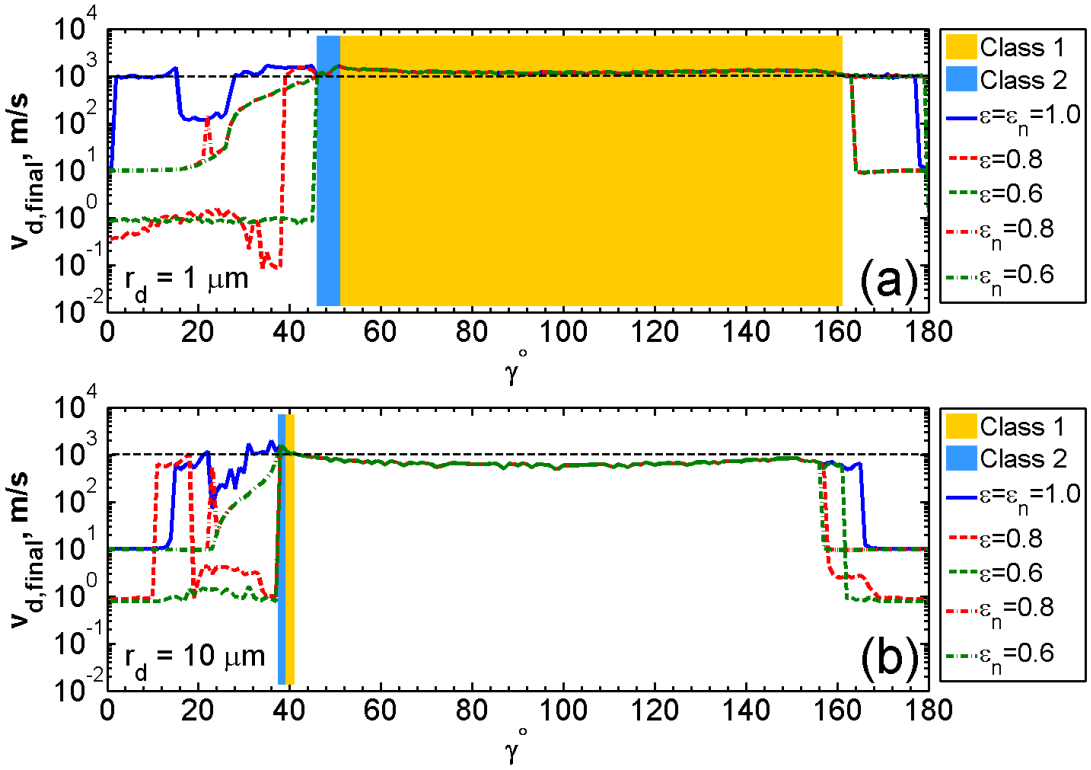


Figure 2.8: The pictures show the final velocity of dust grains varied by the launch angle (γ) for $v_0 = 100$ km/s where (a) is for the initial dust size 1.0 μm and (b) is for the initial dust size 10.0 μm.

primary highlighted by blue color). However, the ranges of Class 2 primary of initial dust size of 1.0 μm and 10 μm are very narrow.

We are interested in Class 2 primary dust grains because they can be observed at the wall and erode the wall by high speed collisions. We omit Class 2 extra because in practice, the inelestic collision causes a loss of kinetic energy everytime a dust grain collide with the wall, so this should not give much contribution to the number of Class 2 dust grains. We also neglect Class 1 extra, because it simply adds the Class 1 primary, i.e. no Class 1 particles acheive high veocity at the wall. Figure 2.9 shows that a dust grain trajectory for $v_0 = 100$ km/s can have their final velocity at the wall beyond 1 km/s without the prior wall collision. This is acheived by partial evaporation. This process allows the droplet to gain a larger acceleration in the toroidal direction. This drives the smaller dust grain back to the SOL, where it eventually collides with the wall. The dust grain trajectory for $v_0 = 20$ km/s is slightly accelerated by the ion drag force but cannot endure the evaporation because the high velocity acceleration takes a long time, while the dust grain with the trajectory of $v_0 =$ 180 km/s is greatly accelerated, but cannot endure evaporation due to high heat deposition.

Figures 2.10 and 2.11 shows four trajectories: (1) injected towards the outer wall SOL; (2) injected towards the core plasma which allows the partial evaporation; (3) injected

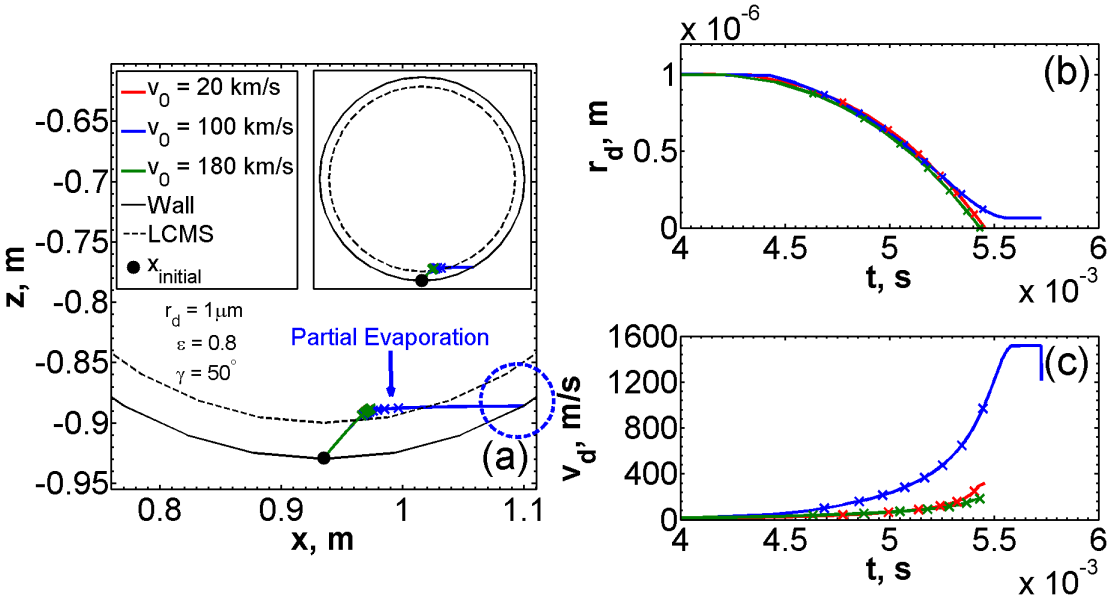


Figure 2.9: The pictures shows (a) the dust trajectories in plasmas which have $v_0 = 20$, 100, 180 km/s and the time evolutions of (b) the dust radius and (c) the dust velocity where the initial dust size is 1 μm. All dust grains are injected in $\gamma = 50°$ and collide with the wall by $\epsilon = 0.8$.

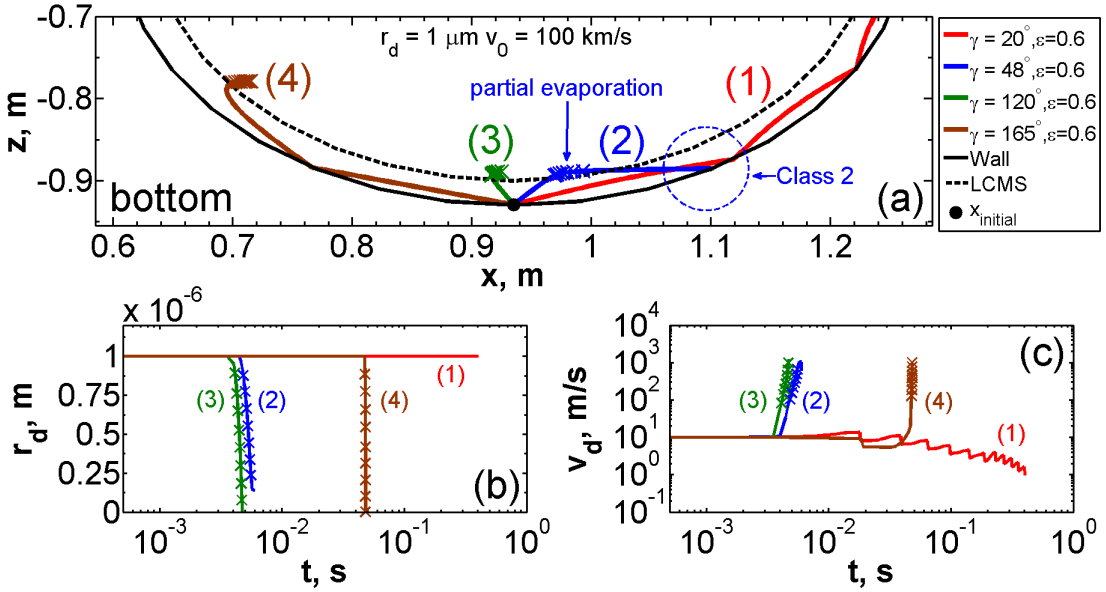


Figure 2.10: The figure shows (a) the trajectories of 1-μm dust grains represented (1) $\gamma = 20°$, (2) $\gamma = 48°$, (3) $\gamma = 120°$ and (4) $\gamma = 165°$ and the associate time evolution of (b) the dust radius and (c) the dust velocity. The plasma has $v_0 = 100$ km/s and the dust-wall collisions is controlled by $\epsilon = 0.6$.

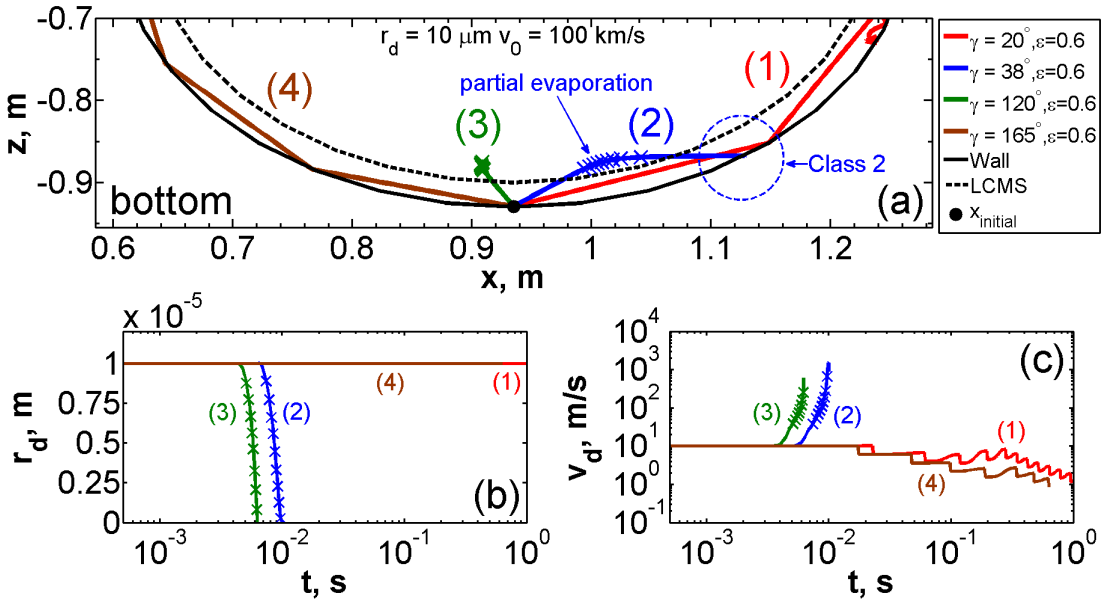


Figure 2.11: The figure shows (a) the trajectories of 10-μm dust grains represented (1) $\gamma = 20°$, (2) $\gamma = 38°$, (3) $\gamma = 120°$ and (4) $\gamma = 165°$ and the associate time evolution of (b) the dust radius and (c) the dust velocity. The plasma has $v_0 = 100$ km/s and the dust-wall collisions is controlled by $\epsilon = 0.6$.

towards the core plasma and completely evaporation; and (4) injected towards the inner wall SOL. Trajectories (1) in figures 2.10 and 2.11 do not achieve high velocities because

the dust grains keeps their size, do not undergo the appropriate acceleration and collide with the wall and lose energy. Trajectories (4) in figure 2.10 shows the smaller dust grain hits the wall and goes into the core by the influence of ion drag force and centrifugal force. It completely evaporates after reaching 1 km/s. In contrast to trajectories (4) in figure 2.11 the bigger dust grain keeps its motion in the SOL and hit the wall so that the velocity is very low. Only trajectories (2) in figures 2.10 and 2.11 can achieve high velocities and survive because of the partial evaporation.

2.4 Conclusions

To achieve high velocity, dust grains need to balance the appropriate evaporation to get the better acceleration controlled by how dust grains moves from the wall and the toroidal plasma flow speed which help dust grains moves from the hot plasma after gaining the appropriate acceleration. Therefore, to get the most suitable conditions for achieving high velocity before colliding with the wall (Class 2 primary), the appropriate ranges of v_0, γ and initial dust size should be 40-130 km/s, $46^\circ - 51^\circ$ and the order of 1 μm when the dust grains move from the bottom of a tokamak.

For avalanche erosion, from the study, it is unlikely to have such a heavy surface erosion. This is because the requirements for dust grains to be accelerated reaching high velocities are very limit on the factors, i.e. a core plasma flow speed, a launch direction, a launch position and an initial size of dust grains. In other words, they require the specific narrow range of the factors for dust grains to achieve high velocities. Moreover, with the very specific requirements, we expect that the population of high velocity dust grains may not be enough to cause a significant damage on plasma facing surfaces. If dust-wall collisions produce secondary dust grains, they must encounter the strict condition to achieve high velocities. Not every dust grain has the chance to reach high velocities by the appropriate partial evaporation. Therefore, plasma facing surfaces should not be seriously damaged by avalanche erosion.

Chapter 3

INTRODUCTION TO MISTY PLASMAS

This chapter contains a review of the classical electronstatic breakup *in vacuo* studied by Lord Rayleigh [53] (section 3.1), which comprises a detailed derivation of Rayleigh's linear stability analysis (section 3.1.1) and recent laboratory observations (section 3.1.2), and the electrostatic breakup of a charged droplet in a misty plasma [54] (section 3.2), which comprises the applicability of Rayleigh's original droplet stability for a small charged droplet in a plasma (section 3.2.1) and details of various pressures, i.e. ion and electron pressures, a pressure due to neutral recombination, a pressure due to a surface tension and an electrostatic pressure. (section 3.2.2).

3.1 Classic electrostatic breakup of a charged droplet

In 1882, Lord Rayleigh [53] showed that an charged droplet *in vacuo* can be unstable if surface charges, Q, exceed a certain value, which can be written in

$$Q \;>\; \sqrt{16\pi^2\varepsilon_0 R^3(\ell+2)\sigma}\,. \tag{3.1}$$

The aboved condition limit where R is an original droplet radius, σ is a surface tension and ℓ is an order of a perturbation surface wave function, was calculated by the use of linear stability analysis. It is suggested that beyond the limit, the outward electrostatic force acting on the droplet surface provided by the surface charges will overcome the inward

surface tension, then a kind of droplet instabilities initiates. At that point, it was unclear how the instability behaves. However, Lord Rayleigh suggested in his paper [53] that the instability is in the form of double jet ejections. The double jet ejections start to develop when the droplet deforms to be in an ellipsoidal shape with two sharp Taylor cones [55]. A tip is developed at each Taylor cone. Two jets are ejected from both tips containing many secondary fine droplets. The characteristic picture of the electrostatically instability or disintegration which Lord Rayleigh suggests have been confirmed by modern observation done by D. Duft *et al* [56, 57] and corresponds to Lord Rayleigh's prediction of the double jet formation [53].

3.1.1 Rayleigh's linear stability analysis

In this section, Rayleigh's linear stabilty analysis for electrostatically disintegration of a charged droplet *in vacuo* [53], without the presence of external pressures, is reviewed. Rayleigh's method is only outlined rather sketchily in his original paper [53] and no completely satisfactory review of it has been published subsequently. Since we apply Rayleigh's work to a situation rather different to his original problem, namely a charged liquid droplet immersed in a plasma, and also extend his approach to the new phenomenon of plasma bubbles (Chapter 6), it is important to be clear about the underlying assumption. For this reason, a very full review of Rayleigh's calculation is presented here. With the help of appendix II in ref. [58], which was later printed in Lord Rayleigh's "The Theory of Sound" [59], the derivation of the perturbed surface energy and the perturbed kinetic energy for Rayleigh's analysis is presented. Also, with the help of ref. [53, 60], we review of the way to calculate the perturbed electrostatic potential energy. Therefore, ref. [53, 58–61] are suggested for more details and are the main references in the review in this section.

To linearly analyse the instability of a charged droplet in the same way as Lord Rayleigh's [53,58], the radius (r) of the charged droplet is given an infinitesimal perturbation of the form.

$$r = \sum_{\ell=0}^{\infty} \xi_\ell(t) P_\ell(\cos\theta). \tag{3.2}$$

where $\xi_\ell(t)$ is an amplitude of surface wave with mode number of ℓ, where $\xi_\ell \ll \xi_0$ and ξ_0 is an equilibrium radius over the amplitude (ξ_ℓ) of the slight perturbation, and $P_\ell(\cos\theta)$ is

a Legendre polynomial of order ℓ, where θ is a polar angle, controlled how each mode of a surface wave behaves. There is no loss of generality to assume symmetry with respect to azimuthal angle (ϕ). We need to perturb the radius of a charged droplet. This is because the instability is mainly associated with the surface phenomena.

In the perturbation, we use the series of Legendre polynomials as the series of surface perturbation waves summed over every normal mode of oscillation. This is because it is important to know which mode of the surface waves triggers the instability first. This will show the minimum surface charge required for initiating the instability. Moreover, to initiate the instability when the situation is in unstable equilibrium, the perturbation or the fluctuation is required to drive the situation and it is always in form of the superposition of some waves with various normal modes. It is therefore possible that the sensitive perturbation of a certain normal mode can trigger the inistability very fast and faster than other normal modes of perturbation.

The radius of a charged droplet is slightly perturbed by a series of Legendre polynomials and the surface deviates from where it was. Liquid is harder to be compressed than gas, therefore, it is reasonable that in Lord Rayleigh's work [53, 58, 59], it is assumed that the liquid droplet is incompressible. This constraint ensures that the volume of the charged droplet is always constant. Although the volume is constant, the surface geometry is still slightly deformed by the introduction of the perturbation, so surface area is changed. With the change of surface area, this causes a change of surface potential energy and a change of surface charge density, where the latter will introduce the change of the electrostatic potential energy.

The surface potential energy, $(\mathrm{PE})_\mathrm{s}$, can be written as the multiplication of surface tension (σ) and surface area (A),

$$(\mathrm{PE})_\mathrm{s} = \sigma A. \tag{3.3}$$

It is clear from the eq. 3.3 that the change in surface energy, $\Delta(\mathrm{PE})_\mathrm{s}$, can be explicitly written in

$$\Delta(\mathrm{PE})_\mathrm{s} = \sigma \Delta A, \tag{3.4}$$

where surface tension (σ) is approximately constant over the infinitesimal perturbation where is in a thermal equilibrium. Hence, only the change in surface area, ΔA, has to be determined. To calculate the change in surface area and the additional surface energy in the Lord Rayleigh's way [58, 59], we initially need to refer to the surface area integral in spherical coordinates for an object with an arbitrary shape (see in Landau and Lifshitz, Fluid Mechanics [62]):

$$A = \int_0^{2\pi} \int_0^{\pi} \sqrt{r^2 + \left(\frac{\partial r}{\partial \theta}\right)^2 + \frac{1}{\sin^2\theta}\left(\frac{\partial r}{\partial \phi}\right)^2}\, r \sin\theta d\theta d\phi. \tag{3.5}$$

To evaluate the result of the integral in 3.5 for a droplet with an arbitrary shape, the radius of the droplet depends on the polar (θ) and azimuthal (ϕ) angles. Due to the azimuthal symmetry assumed in the infinitesimal perturbation, the integrand in eq. 3.5 is independent of ϕ-coordinate, so the ϕ-part of the surface integral, $\int_0^{2\pi} d\phi$, can be explicitly evaluated as 2π and the third term in the integrand becomes 0, i. e. $\frac{\partial r}{\partial \phi} = 0$. As a result, the droplet radius function depends only on the θ-coordinate, which is specified in eq. 3.2, through the use of Legendre polynomials, $P_\ell(\cos\theta)$. The surface integral in 3.5 becomes

$$\begin{aligned} A &= 2\pi \int_0^{\pi} \sqrt{r^2 + \left(\frac{\partial r}{\partial \theta}\right)^2}\, r \sin\theta d\theta & (3.6)\\ &= 2\pi \int_0^{\pi} r \sqrt{1 + \frac{1}{r^2}\left(\frac{\partial r}{\partial \theta}\right)^2}\, r \sin\theta d\theta. & (3.7) \end{aligned}$$

An approximation is needed for the integrand in eq. 3.7. By the use of eq. 3.2,

$$\begin{aligned} r &= \sum_{\ell=0}^{\infty} \xi_\ell P_\ell(\cos\theta) & (3.8)\\ &= \xi_0 + \sum_{\ell=1}^{\infty} \xi_\ell P_\ell(\cos\theta), & (3.9) \end{aligned}$$

where $P_0(\cos\theta) = 1$, we consider

$$\begin{aligned} \frac{\partial r}{\partial \theta} &= \cancelto{0}{\frac{\partial \xi_0}{\partial \theta}} + \sum_{\ell=1}^{\infty} \xi_\ell \frac{\partial P_\ell(\cos\theta)}{\partial \theta} & (3.10)\\ \frac{1}{r^2}\left(\frac{\partial r}{\partial \theta}\right)^2 &\approx \frac{1}{\xi_0^2}\left(\sum_{\ell=1}^{\infty}\sum_{m=1}^{\infty} \xi_\ell \xi_m \frac{\partial P_\ell(\cos\theta)}{\partial \theta}\frac{\partial P_m(\cos\theta)}{\partial \theta}\right) \ll 1 & (3.11) \end{aligned}$$

because $\xi_\ell \xi_m \ll \xi_0^2$, so we use the approximation of

$$(1+x)^a \approx 1 + ax, \tag{3.12}$$

where $x \ll 1$ for the integrand in eq. 3.7. Then eq. 3.7 becomes

$$A = 2\pi \int_0^\pi \left(\underbrace{r^2}_{①} + \underbrace{\frac{1}{2}\left(\frac{\partial r}{\partial \theta}\right)^2}_{②} \right) \sin\theta d\theta. \tag{3.13}$$

Next, the ① and ② terms in eq. 3.13 are separately determined. Firstly, the ① term evaluation starts from

$$\begin{aligned} ① &= 2\pi \int_0^\pi r^2 \sin\theta d\theta & (3.14)\\ &= 2\pi \int_0^\pi \left(\sum_{\ell=0}^{\infty} \xi_\ell P_\ell(\cos\theta)\right)\left(\sum_{m=0}^{\infty} \xi_m P_m(\cos\theta)\right) \sin\theta d\theta & (3.15)\\ &= 2\pi \int_0^\pi \left(\sum_{\ell=0}^{\infty} \xi_\ell^2 P_\ell^2(\cos\theta)\right) + \left(\sum\sum\nolimits_{\ell\neq m} \xi_\ell \xi_m P_\ell(\cos\theta) P_m(\cos\theta)\right) \sin\theta d\theta & (3.16) \end{aligned}$$

Using the variable transformation, $x = \cos\theta$ and $dx = -\sin\theta\, d\theta$, eq. 3.16 becomes

$$① = 2\pi \int_{-1}^{1} \left(\sum_{\ell=0}^{\infty} \xi_\ell^2 P_\ell^2(x)\right) + \left(\sum\sum\nolimits_{\ell\neq m} \xi_\ell \xi_m P_\ell(x) P_m(x)\right) dx. \tag{3.17}$$

The orthogonality of Legendre polynomials,

$$\int_{-1}^{1} P_\ell(x) P_m(x)\, dx = \frac{2}{2\ell+1}\, \delta_{\ell m}\,, \tag{3.18}$$

is applied to eq. 3.17 to cancel out the orthogonal terms, which $\ell \neq m$, but keep the terms

of $\ell = m$, so term ① in eq. 3.13 is transformed to

$$\begin{aligned} ① &= 2\pi \int_{-1}^{1} \left(\xi_0^2 + \sum_{\ell=1}^{\infty} \xi_\ell^2 P_\ell^2(x) \right) dx \\ &\quad + \cancelto{\to 0 \text{ (orthogonality)}}{\left(\sum\sum_{\ell \neq m} \xi_\ell \xi_m \int_{-1}^{1} P_\ell(x) P_m(x)\, dx \right)} \qquad (3.19) \\ &= 4\pi\xi_0^2 + 4\pi \sum_{\ell=1}^{\infty} \frac{\xi_\ell^2}{2\ell+1} \qquad (3.20) \end{aligned}$$

Secondly, we are going to calculate term ② in eq. 3.13. We start from the substitution of $\frac{\partial r}{\partial \theta}$, eq. 3.10, into term ②:

$$\begin{aligned} ② &= 2\pi \int_0^{\pi} \frac{1}{2} \left(\frac{\partial r}{\partial \theta} \right)^2 \sin\theta d\theta \qquad (3.21) \\ &= 2\pi \int_0^{\pi} \frac{1}{2} \left(\sum_{\ell=1}^{\infty} \sum_{m=1}^{\infty} \xi_\ell \xi_m \frac{\partial P_\ell(\cos\theta)}{\partial \theta} \frac{\partial P_m(\cos\theta)}{\partial \theta} \right) \sin\theta d\theta. \qquad (3.22) \end{aligned}$$

Using the same variable transformation as can be seen in the calculation of term ①, $x = \cos\theta$ and $dx = -\sin\theta\, d\theta$, we get

$$② = 2\pi \int_{-1}^{1} \frac{1}{2} \left(\sum_{\ell=1}^{\infty} \sum_{m=1}^{\infty} \xi_\ell \xi_m \frac{\partial P_\ell(x)}{\partial \theta} \frac{\partial P_m(x)}{\partial x} \right) \left(\frac{dx}{d\theta} \right)^2 dx. \qquad (3.23)$$

We find that

$$\left(\frac{dx}{d\theta} \right)^2 = \sin^2\theta = 1 - \cos^2\theta = 1 - x^2. \qquad (3.24)$$

Therefore, eq. 3.23 becomes

$$\begin{aligned} ② &= 2\pi \int_{-1}^{1} \frac{1}{2} \left(\sum_{\ell=1}^{\infty} \sum_{m=1}^{\infty} \xi_\ell \xi_m \frac{\partial P_\ell(x)}{\partial x} \frac{\partial P_m(x)}{\partial x} \right) \left(1 - x^2\right) dx \qquad (3.25) \\ &= \pi \sum_{\ell=1}^{\infty} \sum_{m=1}^{\infty} \xi_\ell \xi_m \int_{-1}^{1} \left(1 - x^2\right) \frac{\partial P_\ell(x)}{\partial x} \frac{\partial P_m(x)}{\partial x}\, dx \qquad (3.26) \\ &= \pi \left(\sum_{\ell=1}^{\infty} \xi_\ell^2 \int_{-1}^{1} \left(1 - x^2\right) \left(\frac{\partial P_\ell(x)}{\partial x} \right)^2 dx \right) + \\ &\quad \pi \left(\sum\sum_{\ell \neq m} \xi_\ell \xi_m \int_{-1}^{1} \left(1 - x^2\right) \frac{\partial P_\ell(x)}{\partial x} \frac{\partial P_m(x)}{\partial x}\, dx \right). \qquad (3.27) \end{aligned}$$

At this point, we refer to another orthogonality of Legendre polynomials which are in the derivative form,

$$\int_{-1}^{1}\left(1-x^2\right)\frac{\partial P_\ell(x)}{\partial x}\frac{\partial P_m(x)}{\partial x}\,dx=\ell(\ell+1)\int_{-1}^{1}P_\ell(x)P_m(x)\,dx=\frac{2\ell(\ell+1)}{2\ell+1}\,\delta_{\ell m}\,. \quad (3.28)$$

By using the orthogonality stated in eq. 3.28, eq. 3.27 can be written as

$$\begin{aligned}
② &= \pi\left(\sum_{\ell=1}^{\infty}\xi_\ell^2\int_{-1}^{1}\left(1-x^2\right)\left(\frac{\partial P_\ell(x)}{\partial x}\right)^2 dx\right) \\
&\quad +\pi\left(\sum\sum\nolimits_{\ell\neq m}\xi_\ell\xi_m\int_{-1}^{1}\left(1-x^2\right)\frac{\partial P_\ell(x)}{\partial x}\frac{\partial P_m(x)}{\partial x}\,dx\right) \quad (3.29)\\
&\quad \rightarrow 0 \text{ (orthogonality)} \\
&= \pi\left(\sum_{\ell=1}^{\infty}\xi_\ell^2\int_{-1}^{1}\left(1-x^2\right)\left(\frac{\partial P_\ell(x)}{\partial x}\right)^2 dx\right) \quad (3.30)\\
&= 2\pi\sum_{\ell=1}^{\infty}\frac{\ell(\ell+1)\xi_\ell^2}{2\ell+1}. \quad (3.31)
\end{aligned}$$

We can find the solutions for the integral ① (3.20) and ② (3.31) of eq. 3.13. To calculate the result for eq. 3.13, we are going to combine ① and ②,

$$\begin{aligned}
A &= 2\pi\int_0^{\pi}\left(r^2+\frac{1}{2}\left(\frac{\partial r}{\partial\theta}\right)^2\right)\sin\theta d\theta \quad (3.32)\\
&= ① + ② \quad (3.33)\\
&= 4\pi\xi_0^2+4\pi\sum_{\ell=1}^{\infty}\frac{\xi_\ell^2}{2\ell+1}+2\pi\sum_{\ell=1}^{\infty}\frac{\ell(\ell+1)\xi_\ell^2}{2\ell+1} \quad (3.34)\\
&= 4\pi\xi_0^2+2\pi\sum_{\ell=1}^{\infty}\frac{\left(\ell^2+\ell+2\right)\xi_\ell^2}{2\ell+1}. \quad (3.35)
\end{aligned}$$

Although we can find the surface area of the perturbed droplet, it is not in the desired form, an unperturbed droplet surface area (A_0) + an additional surface area due to surface perturbation (ΔA). To proceed further for the complete form of the perturbed surface area, we need to use the incompressibility condition to relate ξ_0 with R, the unperturbed (or original) radius of the droplet, i.e. we are going to write ξ_0 in the form of R. The incompressibility we mentioned can be written in

$$\nabla\cdot\mathbf{v}=0 \implies \nabla^2\phi_v=0. \quad (3.36)$$

and

$$V = \text{constant}. \tag{3.37}$$

where $\mathbf{v}$ and ϕ_v are the fluid velocity and the fluid velocity potential, respectively, and V are the droplet volume. We are also considering that the fluid is irrotational, $\nabla \times \mathbf{v} = 0$, so we obtain $\mathbf{v} = \nabla\phi_v$ and can write the fluid motion in the form of the potential flow. At this point, to calculate the relation between ξ_0 and R, we start from the use of eq. 3.37,

$$V = \text{constant} = \frac{4}{3}\pi R^3. \tag{3.38}$$

In general, we calculate the volume by using the volume integral. We calculate it in the spherical coordinate, so the volume integral is

$$\begin{aligned} V &= \int_0^{2\pi}\int_0^{\pi}\int_0^{r} r'^{\,2}\sin\theta\, dr' d\theta d\phi & (3.39)\\ &= \int_0^{2\pi}\int_0^{\pi}\int_0^{r(\theta)=\xi_0+\sum_{\ell=1}^{\infty}\xi_\ell P_\ell(\cos\theta)} r'^{\,2}\sin\theta\, dr' d\theta d\phi. & (3.40) \end{aligned}$$

Again, we choose the perturbation caused by the series of Legendre polynomials, so the perturbation is symmestric in the ϕ-part coordinate. Then, using the variable transformation, $x = \cos\theta$ and $dx = -\sin\theta\, d\theta$, we get

$$\begin{aligned} V &= \frac{2\pi}{3}\int_0^{\pi} \left(r'^{\,3}\right)_0^{r(\theta)=\xi_0+\sum_{\ell=1}^{\infty}\xi_\ell P_\ell(\cos\theta)} \sin\theta\, d\theta & (3.41)\\ &= \frac{2\pi}{3}\int_{-1}^{1}\left(\xi_0 + \sum_{\ell=1}^{\infty}\xi_\ell P_\ell(x)\right)^3 dx. & (3.42) \end{aligned}$$

We use the identity, $(u+v)^3 = u^3 + 3u^2v + 3uv^2 + v^3$, for the integrand in eq. 3.42. Eq.

3.42 can be expanded in

$$V = \frac{2\pi}{3}\int_{-1}^{1} \underbrace{\xi_0^3}_{①} + \underbrace{\left(3\xi_0^2\sum_{\ell=1}^{\infty}\xi_\ell P_\ell(x)\right)}_{②} + \underbrace{\left(3\xi_0\sum_{\ell=1}^{\infty}\sum_{m=1}^{\infty}\xi_\ell\xi_m P_\ell(x)P_m(x)\right)}_{③} + \underbrace{\left(\sum_{\ell=1}^{\infty}\sum_{m=1}^{\infty}\sum_{n=1}^{\infty}\xi_\ell\xi_m\xi_n P_\ell(x)P_m(x)P_n(x)\right)}_{④} dx. \tag{3.43}$$

$\xrightarrow{\quad} 0$ (negligible)

Term ④ is negligible because $\xi_\ell\xi_m\xi_n \ll \xi_0^3$ or R^3. The term ① becomes

$$① = \frac{2\pi}{3}\int_{-1}^{1}\xi_0^3\,dx = \frac{4}{3}\pi\xi_0^3\,. \tag{3.44}$$

With the use of the orthogonality of Legendre polynomial in eq. 3.18, terms ② and ③ in eq. 3.43 become

$$② = 2\pi\xi_0^2\sum_{\ell=1}^{\infty}\xi_\ell\int_{-1}^{1}P_\ell(x)\,dx \tag{3.45}$$

$$= 2\pi\xi_0^2\sum_{\ell=1}^{\infty}\xi_\ell\int_{-1}^{1}P_\ell(x)P_0(x)\,dx \;\;;\;\; P_0(x)=1 \tag{3.46}$$

$$= 4\pi\xi_0^2\sum_{\ell=1}^{\infty}\frac{\xi_\ell}{2\ell+1}\delta_{\ell 0} \tag{3.47}$$

$$= 0 \tag{3.48}$$

$$③ = 2\pi\xi_0\sum_{\ell=1}^{\infty}\sum_{m=1}^{\infty}\xi_\ell\xi_m\int_{-1}^{1}P_\ell(x)P_m(x)\,dx \tag{3.49}$$

$$= 4\pi\xi_0\sum_{\ell=1}^{\infty}\frac{\xi_\ell\xi_m}{2\ell+1}\delta_{\ell m} \tag{3.50}$$

$$= 4\pi\xi_0\left(\sum_{\ell=1}^{\infty}\frac{\xi_\ell^2}{2\ell+1}\delta_{\ell\ell} + \sum\sum_{\ell\neq m}\frac{\xi_\ell\xi_m}{2\ell+1}\delta_{\ell m}\right) \tag{3.51}$$

$= 0$

$$= 4\pi\xi_0\sum_{\ell=1}^{\infty}\frac{\xi_\ell^2}{2\ell+1}. \tag{3.52}$$

Because we already determine terms ① (eq. 3.44), ② (eq. 3.48) and ③ (eq. 3.52) in eq.

3.43 , the incompressibility condition in eq. 3.38 can be written in

$$
\begin{aligned}
V &= ① + ② + ③ && (3.53)\\
\frac{4}{3}\pi R^3 &= \frac{4}{3}\pi\xi_0^3 + 4\pi\xi_0 \sum_{\ell=1}^{\infty} \frac{\xi_\ell^2}{2\ell+1} && (3.54)\\
R^3 &= \xi_0^3\left(1 + \frac{3}{\xi_0^2}\sum_{\ell=1}^{\infty}\frac{\xi_\ell^2}{2\ell+1}\right) = \xi_0^3\left(1 + \frac{1}{\xi_0^2}\sum_{\ell=1}^{\infty}\frac{\xi_\ell^2}{2\ell+1}\right)^3 && (3.55)\\
R^2 &= \xi_0^2\left(1 + \frac{1}{\xi_0^2}\sum_{\ell=1}^{\infty}\frac{\xi_\ell^2}{2\ell+1}\right)^2 = \xi_0^2 + 2\sum_{\ell=1}^{\infty}\frac{\xi_\ell^2}{2\ell+1} && (3.56)\\
R &= \xi_0\left(1 + \frac{1}{\xi_0^2}\sum_{\ell=1}^{\infty}\frac{\xi_\ell^2}{2\ell+1}\right) = \xi_0 + \frac{1}{\xi_0}\sum_{\ell=1}^{\infty}\frac{\xi_\ell^2}{2\ell+1}. && (3.57)
\end{aligned}
$$

We come back to eq. 3.35 and use $\xi_0^2 = R^2 - 2\sum_{\ell=1}^{\infty}\frac{\xi_\ell^2}{2\ell+1}$,

$$
\begin{aligned}
A &= 4\pi R^2 - 2\pi\sum_{\ell=1}^{\infty}\frac{4\xi_\ell^2}{2\ell+1} + 2\pi\sum_{\ell=1}^{\infty}\frac{\left(\ell^2+\ell+2\right)\xi_\ell^2}{2\ell+1} && (3.58)\\
&= 4\pi R^2 + 2\pi\sum_{\ell=1}^{\infty}\frac{\left(\ell^2+\ell-2\right)\xi_\ell^2}{2\ell+1} && (3.59)\\
&= 4\pi R^2 + 2\pi\sum_{\ell=1}^{\infty}\frac{(\ell+2)(\ell-1)\xi_\ell^2}{2\ell+1} && (3.60)\\
&= A_0 + \Delta A. && (3.61)
\end{aligned}
$$

By comparison, we can find the original (or unperturbed) surface area, $A_0 = 4\pi R^2$ and the additional surface area done by the perturbation, $\Delta A = 2\pi\sum_{\ell=1}^{\infty}\frac{(\ell+2)(\ell-1)\xi_\ell^2}{2\ell+1}$. The addition surface area results in the additional surface energy (eq. 3.4), which is

$$
\begin{aligned}
\Delta(\mathrm{PE})_\mathrm{s} &= \sigma\Delta A && (3.62)\\
&= 2\pi\sigma\sum_{\ell=1}^{\infty}\frac{(\ell+2)(\ell-1)\xi_\ell^2}{2\ell+1}. && (3.63)
\end{aligned}
$$

At this point, we can determine the additional surface energy, $\Delta(\mathrm{PE})_\mathrm{s}$ shown in eq. 3.63, done by the perturbation, which is the same as that is shown in ref. [58, 59].

Next we are going to proceed in the calculation of the perturbed electrostatic potential, following ref's. [53, 60]. In the vacuum surrounding the droplet, the electrostatic

potential satisfies Laplace's equation:

$$\nabla^2 \phi_E = 0. \tag{3.64}$$

We are going to consider the Laplace equation, eq. 3.64, in the spherical coordinates, which appropriately corresponds to the droplet problem. We also consider azimuthal symmetry, independent of the ϕ coordinate. The general solution of the Laplace equation in the spherical cooridinates [63], which is found by the seperation of variables method, $\phi_E(r,\theta) = F_1(r)F_2(\theta)$, can be written in

$$\phi_E(r,\theta) = \sum_{\ell=0}^{\infty} \left(A_\ell r^\ell + \frac{B_\ell}{r^{\ell+1}} \right) P_\ell(\cos\theta), \tag{3.65}$$

which is known as the multipole expansion. Furthermore, the multipole expansion stated in eq. 3.65 provides an electrostatic potential of an object with an arbitrary shape. We need to consider the boundary conditions to keep the reasonable coefficients remaining in the multipole expansion. We are interested in the electrostatic potential at the droplet surface or outside the droplet, so $A_\ell = 0$ is chosen because the term $A_\ell r^\ell$ diverges inside the droplet. Then,

$$\phi_E = \sum_{\ell=0}^{\infty} \frac{B_\ell}{r^{\ell+1}} P_\ell(\cos\theta) \tag{3.66}$$

$$= \underbrace{\frac{Q}{4\pi\varepsilon_0 r}}_{monopole} + \underbrace{\sum_{\ell=1}^{\infty} \frac{B_\ell}{r^{\ell+1}} P_\ell(\cos\theta)}_{multipoles}. \tag{3.67}$$

From eq. 3.67, it is noticeable that the monopole term corresponds the electrostatic potential of a perfect sphere while the multipole terms correspond to the shape variation from the perfect sphere. We aim to find the perturbed electrostatic potential, which is now replaced by the notation of ϕ_E, of a droplet with the infinitesimal perturbation. The spherical droplet, which is in a equilibrium spherical shape controlled by a surface tension (σ), is slightly deformed to an ellipsoidal droplet by the use of the series of Legendre polynomial, which is referred to eq. 3.2. This means that the multipole terms represent the change in the electrostatic potential from the perturbation of the droplet. From this point, we are going to determine the coefficients, B_ℓ, and eventually the perturbed electrostatic potential,

ϕ_E, of a deformed charged droplet. It should be beneficial to think that the perturbation coefficients of the charged droplet radius, ξ_ℓ are related to those of the electrostatic potential, B_ℓ, in some way. Surface charges are introduced on a droplet surface and strictly located on the surface because of the assumption that a charged droplet is assumed to be a perfect conductor. This results in a self electric field and an electrostatic potential. To find the perturbed electrostatic potential in Lord Rayleigh's way, the help of ref. [53, 60] is needed. Firstly, we need to expand eq. 3.67 by the use of eq. 3.2, which becomes

$$\phi_E = \frac{Q}{4\pi\varepsilon_0 \left(\xi_0 + \sum_{\ell=1}^{\infty} \xi_\ell P_\ell(\cos\theta)\right)} + \sum_{m=1}^{\infty} \frac{B_m}{\left(\xi_0 + \sum_{\ell=1}^{\infty} \xi_\ell P_\ell(\cos\theta)\right)^{m+1}} P_m(\cos\theta), \quad (3.68)$$

where Q is the total of the charged droplet, which always stay constant. We are going to use two approximations. First, the change in the electrostatic potential of a charged droplet is done by the perturbation of the droplet radius. Second, we are interested in the perturbed electrostatic potential in the form of the unperturbed droplet radius (R) not ξ_0. We use eq. 3.57 substituted into eq. 3.2,

$$\begin{aligned} r &= \xi_0 + \sum_{\ell=1}^{\infty} \xi_\ell P_\ell(\cos\theta) && (3.69)\\ &= R - \frac{1}{\xi_0} \sum_{\ell=1}^{\infty} \frac{\xi_\ell^2}{2\ell+1} + \sum_{\ell=1}^{\infty} \xi_\ell P_\ell(\cos\theta) \quad \xi_\ell^2 \to 0 \text{ (negligible)} && (3.70)\\ &\approx R + \sum_{\ell=1}^{\infty} \xi_\ell P_\ell(\cos\theta). && (3.71) \end{aligned}$$

We neglect the second order term (ξ_ℓ^2) because $\frac{\xi_\ell^2}{\xi_0} \ll 0$, so we aim to make the approximation only with the accuracy of the first order term (ξ_ℓ). With these two approximations, eq. 3.72 can be changed to

$$\phi_E = \frac{Q}{4\pi\varepsilon_0 \left(R + \sum_{\ell=1}^{\infty} \xi_\ell P_\ell(\cos\theta)\right)} + \sum_{m=1}^{\infty} \frac{B_m}{\left(R + \sum_{\ell=1}^{\infty} \xi_\ell P_\ell(\cos\theta)\right)^{m+1}} P_m(\cos\theta). \quad (3.72)$$

From this point, we are going to use the approximation shown in eq. 3.12, because $\frac{\xi_\ell}{R} \ll 1$,

and proceed further for the expression of B_ℓ,

$$\begin{aligned}
\phi_E &= \frac{Q}{4\pi\varepsilon_0 R}\left(1+\sum_{\ell=1}^{\infty}\frac{\xi_\ell P_\ell(\cos\theta)}{R}\right)^{-1} \\
&\quad + \sum_{m=1}^{\infty}\frac{B_m}{R^{m+1}}\left(1+\sum_{\ell=1}^{\infty}\frac{\xi_\ell P_\ell(\cos\theta)}{R}\right)^{-(m+1)} P_m(\cos\theta) \qquad (3.73)\\
\phi_E &= \frac{Q}{4\pi\varepsilon_0 R}\left(1-\sum_{\ell=1}^{\infty}\frac{\xi_\ell P_\ell(\cos\theta)}{R}\right) \\
&\quad + \sum_{m=1}^{\infty}\frac{B_m}{R^{m+1}}\left(1-(m+1)\sum_{\ell=1}^{\infty}\frac{\xi_\ell P_\ell(\cos\theta)}{R}\right) P_m(\cos\theta) \qquad (3.74)\\
\phi_E &= \underbrace{\frac{Q}{4\pi\varepsilon_0 R}}_{①} - \underbrace{\frac{Q}{4\pi\varepsilon_0 R^2}\sum_{\ell=1}^{\infty}\xi_\ell P_\ell(\cos\theta)}_{②} + \underbrace{\sum_{m=1}^{\infty}\frac{B_m P_m(\cos\theta)}{R^{m+1}}}_{③} \\
&\quad \underbrace{-\sum_{\ell=1}^{\infty}\sum_{m=1}^{\infty}(m+1)\frac{\xi_\ell B_m P_\ell(\cos\theta)\cancel{P_m(\cos\theta)}}{R^{m+2}}}_{④} \to 0 \text{ (negligible)}. \qquad (3.75)
\end{aligned}$$

We neglect term ④ of eq. 3.75, which is the second order perturbation, because we aim for the accuracy of the first order perturbation. As shown in eq. 3.75, term ① indicates the unperturbed (or equilibrium) electrostatic potential at the spherical surface while term ②+③ indicates the first order perturbation away from the equilibrium electrostatic potential, which is $\phi_{E,0} = \frac{Q}{4\pi\varepsilon_0 R}$, where the subscript "0" means the equilibrium point. The Taylor's expansions of the electrostatic potential about the equilibrium point, $\phi_{E,0}$, at each θ, we discover that

$$\begin{aligned}
\phi_E(r) &= \phi_{E,0} + \phi_{E,1} + \phi_{E,2} + \ldots \qquad (3.76)\\
&= \underbrace{\phi_{E,0}}_{equilibrium} + \underbrace{(r-R)\left(\frac{\partial\phi_E}{\partial r}\right)_0}_{1^{st}\,order} + \underbrace{(r-R)^2\left(\frac{\partial^2\phi_E}{\partial r^2}\right)_0}_{2^{nd}\,order} + \ldots \qquad (3.77)
\end{aligned}$$

In general, at the steady state where the charges on the droplet config itself to be electrostatic, the equilibrium acheives, so at the equilibrium, $\left(\frac{\partial\phi_E}{\partial r}\right)_0 = 0$. From this, we can say that

$$\phi_E(r) \approx \phi_{E,0} = \frac{Q}{4\pi\varepsilon_0 R} \qquad (3.78)$$

with the accuracy of the first order term. By relating eq. 3.75 with eq. 3.77 and the fact that $\left(\frac{\partial \phi_E}{\partial r}\right)_0 = 0$, we understand that

$$\begin{aligned} ② + ③ &= 0 && (3.79)\\ -\frac{Q}{4\pi\varepsilon_0 R^2}\sum_{\ell=1}^{\infty}\xi_\ell P_\ell(\cos\theta) + \sum_{\ell=1}^{\infty}\frac{B_\ell P_\ell(\cos\theta)}{R^{\ell+1}} &= 0 && (3.80)\\ B_\ell &= \frac{Q\xi_\ell R^{\ell-1}}{4\pi\varepsilon_0}. && (3.81) \end{aligned}$$

By substituting 3.81 into eq. 3.67, now we can find the perturbed electrostatic potential, $\phi_{E,0}$, with the terms containing the single Legendre polynomial,

$$\phi_E = \frac{Q}{4\pi\varepsilon_0 r} + \frac{Q}{4\pi\varepsilon_0}\sum_{\ell=1}^{\infty}\frac{\xi_\ell R^{\ell-1}}{r^{\ell+1}}P_\ell(\cos\theta). \quad (3.82)$$

The perturbed electrostatic potential shown in eq. 3.82 is not the final form we aim for because it still has the single Legendre polynomials and this does not correspond to the work done by Lord Rayleigh [53]. We need to perform the cancellation of these Legendre polynomials by the use of the orthogonality of Legendre polynomials suggested by and also referred to ref. [60]. Before going further in detail, we would like to mention about how we calculate the electrostatic potential by using path integral of electric field, **E**. We start from

$$\phi_E(\mathbf{r}) = -\int_{\text{ref.}\to\infty}^{\mathbf{r}} \mathbf{E}\cdot d\mathbf{l}. \quad (3.83)$$

First, we consider a small amount of charges, δQ, which provide radial electric electric field, $\delta\mathbf{E} = \frac{\delta Q}{4\pi\varepsilon_0 r^2}\hat{r}$. The electrostatic potential at any distance done by the existence of δQ can be found by eq. 3.83,

$$\begin{aligned} \phi_E(\mathbf{r}) &= -\int_{\text{ref.}\to\infty}^{\mathbf{r}} \mathbf{E}\cdot d\mathbf{l} && (3.84)\\ \delta\phi_E(r) &= -\int_{\text{ref.}\to\infty}^{r} \delta E dr && (3.85)\\ &= -\int_{\text{ref.}\to\infty}^{r} \frac{\delta Q}{4\pi\varepsilon_0 r^2} dr && (3.86)\\ &= \frac{\delta Q}{4\pi\varepsilon_0 r}. && (3.87) \end{aligned}$$

We can also use the superposition principle to find the total electrostatic potential, $\sum_{i=1}^{n} \delta\phi_{E,i}$ done by each group of a small charges, δQ_i placed at any distances, r_i, so

$$\phi_E = \sum_{i=1}^{n} \delta\phi_{E,i} \tag{3.88}$$

$$= \frac{1}{4\pi\varepsilon_0} \sum_{i=1}^{n} \frac{\delta Q_i}{r_i}. \tag{3.89}$$

With regards to eq. 3.89, we are interested in calculating the total electrostatic potential at the distances of a perturbed droplet surface, where is controlled by $r = \xi_0 + \sum_{\ell=1}^{\infty} \xi_\ell P_\ell(\cos\theta)$, done by infinitesimal charge elements, dQ, also continuously located on the perturbed droplet surface. Eq. 3.89 becomes

$$\phi_E = \frac{1}{4\pi\varepsilon_0} \oint_{surface} \frac{dQ}{r}. \tag{3.90}$$

The charges on the surface is constant but the perturbation changes the charge configuration, i.e. surface charge density, α. This later results in the fluctuation of the equilibrium electric field because the curvature of the charged droplet is varied in the θ variable controlled by the Legendre polynomials of any order used in the perturbation. Eventually, the new electrostatic potential and also electrostatic potential energy are set up. Eq. 3.90 can be also written in

$$\phi_E = \frac{1}{4\pi\varepsilon_0} \oint_{surface} \frac{\alpha}{r} dA \tag{3.91}$$

$$= \frac{1}{4\pi\varepsilon_0} \int_0^{2\pi} \int_0^{\pi} \frac{\alpha}{r} R^2 \sin\theta \, d\theta d\phi \tag{3.92}$$

$$= \frac{1}{4\pi\varepsilon_0} \int_0^{2\pi} \int_0^{\pi} \frac{\alpha}{R\left(1 + \sum_{\ell=1}^{\infty} \frac{\xi_\ell P_\ell(\cos\theta)}{R}\right)} R^2 \sin\theta \, d\theta d\phi \tag{3.93}$$

$$= \frac{1}{4\pi\varepsilon_0} \int_0^{2\pi} \int_0^{\pi} \alpha \left(1 - \sum_{\ell=1}^{\infty} \frac{\xi_\ell P_\ell(\cos\theta)}{R}\right) R \sin\theta \, d\theta d\phi \; ; \; \frac{\xi_\ell}{R} \ll 1. \tag{3.94}$$

We can use the initial perturbed electrostatic potential, ϕ_E in eq. 3.82, for calculating the

perturbed surface charge density, α in eq. 3.94, through the use of Gauss' Law,

$$\oint \mathbf{E} \cdot d\mathbf{A} = \frac{Q}{\varepsilon_0} \tag{3.95}$$

$$\oint \mathbf{E} \cdot d\mathbf{A} = \oint \frac{\alpha dA}{\varepsilon_0} \tag{3.96}$$

$$\oint (-\nabla \phi_E) \cdot d\mathbf{A} = \oint \frac{\alpha dA}{\varepsilon_0}. \tag{3.97}$$

We approximate that the integral of the Gauss' law in eq. 3.92 and 3.97 is performed over the unperturbed droplet surface. This results in

$$\oint (-\nabla \phi_E) \cdot \hat{r} dA = \oint \frac{\alpha dA}{\varepsilon_0} \tag{3.98}$$

$$\frac{\partial \phi_E}{\partial r} = -\frac{\alpha}{\varepsilon_0} \tag{3.99}$$

$$-\frac{Q}{4\pi\varepsilon_0 r^2} - \frac{Q}{4\pi\varepsilon_0} \sum_{\ell=1}^{\infty} \frac{(\ell+1)\xi_\ell R^{\ell-1}}{r^{\ell+2}} P_\ell(\cos\theta) = -\frac{\alpha}{\varepsilon_0} \tag{3.100}$$

$$\frac{Q}{4\pi r^2} + \frac{Q}{4\pi} \sum_{\ell=1}^{\infty} \frac{(\ell+1)\xi_\ell R^{\ell-1}}{r^{\ell+2}} P_\ell(\cos\theta) = \alpha. \tag{3.101}$$

Furthermore, by substituting eq. 3.71, $r \approx R + \sum_{\ell=1}^{\infty} \xi_\ell P_\ell(\cos\theta)$, into eq. 3.101, we obtain

$$\alpha = \frac{Q}{4\pi \left(R + \sum_{\ell=1}^{\infty} \xi_\ell P_\ell(\cos\theta)\right)^2} + \frac{Q}{4\pi} \sum_{\ell=1}^{\infty} \frac{(\ell+1)\xi_\ell R^{\ell-1}}{\left(R + \sum_{m=1}^{\infty} \xi_m P_m(\cos\theta)\right)^{\ell+2}} P_\ell(\cos\theta) \tag{3.102}$$

$$= \frac{Q}{4\pi R^2} \left(1 + \sum_{\ell=1}^{\infty} \frac{\xi_\ell P_\ell(\cos\theta)}{R}\right)^{-2} + \frac{Q}{4\pi} \sum_{\ell=1}^{\infty} \frac{(\ell+1)\xi_\ell R^{\ell-1}}{R^{\ell+2}} \left(1 + \sum_{m=1}^{\infty} \frac{\xi_m P_m(\cos\theta)}{R}\right)^{-(\ell+2)} P_\ell(\cos\theta) \tag{3.103}$$

$$= \frac{Q}{4\pi R^2} \left(1 - 2\sum_{\ell=1}^{\infty} \frac{\xi_\ell P_\ell(\cos\theta)}{R}\right) + \frac{Q}{4\pi} \sum_{\ell=1}^{\infty} \frac{(\ell+1)\xi_\ell R^{\ell-1}}{R^{\ell+2}} \left(1 - (\ell+2)\sum_{m=1}^{\infty} \frac{\xi_m P_m(\cos\theta)}{R}\right) P_\ell(\cos\theta) \tag{3.104}$$

$$= \frac{Q}{4\pi R^2} - \frac{Q}{4\pi} \sum_{\ell=1}^{\infty} \frac{2\xi_\ell P_\ell(\cos\theta)}{R^3} + \frac{Q}{4\pi} \sum_{\ell=1}^{\infty} \frac{(\ell+1)\xi_\ell P_\ell(\cos\theta)}{R^3} - \frac{Q}{4\pi} \sum_{\ell=1}^{\infty} \sum_{m=1}^{\infty} \frac{(\ell+1)(\ell+2)\xi_\ell \xi_m P_\ell(\cos\theta) P_m(\cos\theta)}{R^4}. \tag{3.105}$$

$\to 0$ (negligible)

As can be seen in eq. 3.105, the final term with $\frac{\xi_\ell \xi_m}{R^4}$ is neglected because $\frac{\xi_\ell \xi_m}{R^4} \ll 1$, very small. We therefore obtain the perturbed surface charge density,

$$\alpha = \frac{Q}{4\pi R^2} + \frac{Q}{4\pi} \sum_{\ell=1}^{\infty} \frac{(\ell-1)\xi_\ell P_\ell(\cos\theta)}{R^3}. \tag{3.106}$$

The equation of the perturbed surface charge density, α, in eq. 3.106 have to be substituted into eq. 3.94. The perturbed variables, i.e. α and r, is integrated over the unperturbed surface.

$$\begin{aligned} \phi_E = \frac{1}{4\pi\varepsilon_0} \int_0^{2\pi} \int_0^{\pi} \left(\frac{Q}{4\pi R^2} + \frac{Q}{4\pi} \sum_{\ell=1}^{\infty} \frac{(\ell-1)\xi_\ell P_\ell(\cos\theta)}{R^3} \right) \cdot \\ \left(1 - \sum_{\ell=1}^{\infty} \frac{\xi_\ell P_\ell(\cos\theta)}{R} \right) R \sin\theta \, d\theta d\phi. \end{aligned} \tag{3.107}$$

Using the variable transformation, $x = \cos\theta$ and $dx = -\sin\theta \, d\theta$, eq. 3.107 becomes

$$\begin{aligned} \phi_E = \frac{1}{2\varepsilon_0} \int_{-1}^{1} \Bigg(& \underbrace{\frac{Q}{4\pi R}}_{①} + \underbrace{\frac{Q}{4\pi} \sum_{\ell=1}^{\infty} \frac{(\ell-1)\xi_\ell P_\ell(x)}{R^2}}_{②} - \underbrace{\frac{Q}{4\pi} \sum_{\ell=1}^{\infty} \frac{\xi_\ell P_\ell(x)}{R^2}}_{③} \\ & \underbrace{- \frac{Q}{4\pi} \sum_{\ell=1}^{\infty} \sum_{m=1}^{\infty} \frac{(\ell-1)\xi_\ell \xi_m P_\ell(x) P_m(x)}{R^3}}_{④} \Bigg) \, dx. \end{aligned} \tag{3.108}$$

We are going to determine the expression for each term in eq. 3.108:

$$① = \frac{Q}{4\pi\varepsilon_0 R} \tag{3.109}$$

$$② = \frac{1}{2\varepsilon_0} \int_{-1}^{1} \frac{Q}{4\pi} \sum_{\ell=1}^{\infty} \frac{(\ell-1)\xi_\ell P_\ell(x) P_0(x)}{R^2} \, dx \tag{3.110}$$

$$= 0 \quad ; \text{because } \int_{-1}^{1} P_\ell(x) P_0(x) \, dx = 0 \text{ and } P_0(x) = 1 \tag{3.111}$$

$$③ = \frac{1}{2\varepsilon_0} \int_{-1}^{1} \frac{Q}{4\pi} \sum_{\ell=1}^{\infty} \frac{\xi_\ell P_\ell(x)}{R^2} \, dx \tag{3.112}$$

$$= 0 \quad ; \text{because } \int_{-1}^{1} P_\ell(x) P_0(x) \, dx = 0 \text{ and } P_0(x) = 1 \tag{3.113}$$

$$④ = \frac{Q}{8\pi\varepsilon_0}\int_{-1}^{1}\sum_{\ell=1}^{\infty}\left(\frac{(\ell-1)\xi_\ell^2 P_\ell^2(x)}{R^3} + \cancelto{0}{\sum\sum_{\ell\neq m}\frac{(\ell-1)\xi_\ell\xi_m P_\ell(x)P_m(x)}{R^3}}\right)dx. \quad (3.114)$$

With the othogonality of Legendre polynomial in eq. 3.18,

$$④ = \frac{Q}{8\pi\varepsilon_0}\sum_{\ell=1}^{\infty}\frac{(\ell-1)\xi_\ell^2}{R^3}\frac{2}{2\ell+1} \quad (3.115)$$

$$= \frac{Q}{4\pi\varepsilon_0}\sum_{\ell=1}^{\infty}\frac{(\ell-1)\xi_\ell^2}{(2\ell+1)R^3}. \quad (3.116)$$

After identifying the terms ①, ②, ③ and ④ of eq. 3.108, the final form of the perturbed electrostatic potential, ϕ_E, without the Legendre polynomials is

$$\phi_E = \frac{Q}{4\pi\varepsilon_0 R} - \frac{Q}{4\pi\varepsilon_0}\sum_{\ell=1}^{\infty}\frac{(\ell-1)\xi_\ell^2}{(2\ell+1)R^3}, \quad (3.117)$$

and the perturbed electrostatic potential energy, $(\mathrm{PE})_\mathrm{E}$, is

$$(\mathrm{PE})_\mathrm{E} = \frac{1}{2}Q\phi_E = \frac{Q^2}{8\pi\varepsilon_0 R} - \frac{Q^2}{8\pi\varepsilon_0}\sum_{\ell=1}^{\infty}\frac{(\ell-1)\xi_\ell^2}{(2\ell+1)R^3}, \quad (3.118)$$

where $\frac{Q^2}{8\pi\varepsilon_0 R}$ is the electrostatic potential energy of the unperturbed spherical droplet, and the change in the unperturbed electrostatic potential energy, $\Delta(\mathrm{PE})_\mathrm{E}$, contributed from the perturbation is

$$\Delta(\mathrm{PE})_\mathrm{E} = -\frac{Q^2}{8\pi\varepsilon_0}\sum_{\ell=1}^{\infty}\frac{(\ell-1)\xi_\ell^2}{(2\ell+1)R^3}. \quad (3.119)$$

This corresponds to the perturbed electrostatic potential energy of Lord Rayleigh's work [53]. To determine the total change of potential energy, $\Delta(\mathrm{PE})$ done by the surface perturbation, the changes in surface energy, $\Delta(\mathrm{PE})_\mathrm{s}$ in eq. 3.63, and electrostatic potential energy, $\Delta(\mathrm{PE})_\mathrm{E}$ in eq. 3.119 are combined,

$$\Delta(\mathrm{PE}) = \Delta(\mathrm{PE})_\mathrm{s} + \Delta(\mathrm{PE})_\mathrm{E} \quad (3.120)$$

$$= 2\pi\sigma\sum_{\ell=1}^{\infty}\frac{(\ell+2)(\ell-1)\xi_\ell^2}{2\ell+1} - \frac{Q^2}{8\pi\varepsilon_0}\sum_{\ell=1}^{\infty}\frac{(\ell-1)\xi_\ell^2}{(2\ell+1)R^3}. \quad (3.121)$$

The change in total potential energy of the surface-perturbed charged droplet

surface indicates the perturbation of the system from the equilibrium. Because of the conservation of energy, the change in total potential energy, Δ(PE), changes its form to the addtional kinetic energy, Δ(KE), which drives the motion of the droplet surface. With the assumption that the droplet fluid is irrotational, we can use the potential flow, where $\mathbf{v} = \nabla\phi_v$, idea to find the total additional kinetic energy. Therefore,

$$\begin{aligned} \Delta(\mathrm{KE}) &= \frac{1}{2}mv^2 && (3.122)\\ &= \frac{1}{2}\rho\int_{volume} v^2 dV && (3.123)\\ &= \frac{1}{2}\rho\int_{volume} \nabla\phi_v\cdot\nabla\phi_v\, dV. && (3.124) \end{aligned}$$

The incompressibility is assumed in this work, so $\nabla^2\phi_v = 0$, so

$$\begin{aligned} \Delta(\mathrm{KE}) &= \frac{1}{2}\rho\int_{volume}\Big(\nabla\cdot(\phi_v\nabla\phi_v) - \cancelto{0}{\phi_v\nabla^2\phi_v}\Big)dV && (3.125)\\ &= \frac{1}{2}\rho\int_{volume}\nabla\cdot(\phi_v\nabla\phi_v)\; dV && (3.126)\\ &= \frac{1}{2}\rho\oint_{surface}(\phi_v\nabla\phi_v)_s\cdot d\mathbf{A} \quad \text{(using divergence theorem)}, && (3.127) \end{aligned}$$

where the subscript s in the integrand of eq. 3.127 means considering at the droplet surface. At first sight it appears as if we may use the time derivative of the perturbed droplet radius as the perturbed velocity; however, it is not applicable because the incompressibility need to be applied through the perturbed velocity potential expression (see the integrand of eq 3.125). If the fluid stays at rest, the fluid velocity is zero, i.e. velocity potential is constant, $\phi_v = A_0'$ (see eq. 3.129). If a pertubation is introduced on a droplet surface, the inner fluid cannot stay at rest and start to move responding to the perturbation. Because the fluid of the droplet is assumed to be incompressible and irrotational and the suitable coordinates for the droplet instability problem is the spherical coordinates, we can consider the Laplace equation, $\nabla^2\phi_v = 0$, in the spherical coordinates where the general solution can be referred to the multipole expansion, eq. 3.65, used for $\nabla^2\phi_E = 0$, eq. 3.64. From this, the general solution, ϕ_v, of the perturbed potential flow in the droplet is

$$\phi_v(r,\theta) = \sum_{\ell=0}^{\infty}\left(A_\ell' r^\ell + \frac{B_\ell'}{r^{\ell+1}}\right)P_\ell(\cos\theta). \qquad (3.128)$$

The suitable boundary conditions of the potenial flow in the droplet are that the fluid remains at rest at the centre of the droplet, i.e. ϕ_v = constant at $r = 0$ and the largest fluid flow occurs near the surface of the perturbed droplet. This implies that inside the perturbed droplet, the fluid flow velocity and the associated velocity potential increases from the centre to the surface of the droplet. Therefore, this results in $B'_\ell = 0$ and

$$\phi_v(r,\theta) = \underbrace{A'_0}_{unperturbed} + \underbrace{\sum_{\ell=1}^{\infty} A'_\ell r^\ell P_\ell(\cos\theta)}_{perturbed}. \tag{3.129}$$

From eq. 3.127, to find the additional kinetic energy, we integrate the integrand over the unperturbed surface, so

$$\Delta(\mathrm{KE}) = \frac{1}{2}\rho \int_0^{2\pi}\int_0^{\pi} (\phi_v \nabla\phi_v)_s \cdot \hat{r}\, R^2 \sin\theta\, d\theta d\phi \tag{3.130}$$

$$= \frac{1}{2}\rho \int_0^{2\pi}\int_0^{\pi} \left(\phi_v \frac{\partial\phi_v}{\partial r}\right)_s R^2 \sin\theta\, d\theta d\phi. \tag{3.131}$$

Referring to the perturbed droplet radius written in eq. 3.2, we can add the time evolution to each ℓ-th mode amplitude, $\xi_\ell = \xi_\ell(t)$. Therefore, the perturbed droplet radius, r, and the perturbed surface velocity, $\left(\frac{dr}{dt}\right)_s$, can be

$$r = \xi_0 + \sum_{\ell=1}^{\infty} \xi_\ell(t) P_\ell(\cos\theta) \tag{3.132}$$

$$\left(\frac{dr}{dt}\right)_s = \sum_{\ell=1}^{\infty} \frac{d\xi_\ell(t)}{dt} P_\ell(\cos\theta), \tag{3.133}$$

where later we can write $\frac{d\xi_\ell(t)}{dt}$ as $\dot{\xi}_\ell$. We can also write the perturbed velocity (ϕ_v) as

$$\frac{\partial\phi_v}{\partial r} = \sum_{\ell=1}^{\infty} \ell A'_\ell r^{\ell-1} P_\ell(\cos\theta) \tag{3.134}$$

and

$$\left(\frac{\partial\phi_v}{\partial r}\right)_s = \sum_{\ell=1}^{\infty} \ell A'_\ell R^{\ell-1} P_\ell(\cos\theta), \tag{3.135}$$

which is evaluated at the unperturbed surface, when the droplet surface motion initiates.

By combining eq. 3.129 for ϕ_v and 3.134 for $\frac{\partial \phi_v}{\partial r}$, we obtain the integrand of eq. 3.131 as

$$\left(\phi_v \frac{\partial \phi_v}{\partial r}\right)_s = A_0' \sum_{\ell=1}^{\infty} \ell A_\ell' R^{\ell-1} P_\ell(\cos\theta) + \sum_{\ell=1}^{\infty} \ell A_\ell'^2 R^{2\ell-1} P_\ell^2 + \sum\sum_{\ell \neq m} \ell A_\ell' A_m' R^{\ell-1} R^m P_\ell(\cos\theta) P_m(\cos\theta), \tag{3.136}$$

where the integrand in the integral of eq. 3.131 are considered based on the unperturbed surface at the initiation of the perturbed surface motion. Equating eq. 3.133 and 3.135, we can write the integrand in terms of $\dot{\xi}_\ell$,

$$\left(\phi_v \frac{\partial \phi_v}{\partial r}\right)_s = A_0' \sum_{\ell=1}^{\infty} \dot{\xi}_\ell P_\ell(\cos\theta) + \sum_{\ell=1}^{\infty} \frac{\dot{\xi}_\ell^{\,2} R}{\ell} P_\ell^2 + \sum\sum_{\ell \neq m} \frac{\dot{\xi}_\ell \dot{\xi}_m R}{m} P_\ell(\cos\theta) P_m(\cos\theta). \tag{3.137}$$

Using the variable transformation, $x = \cos\theta$ and $dx = -\sin\theta\, d\theta$ and eq. 3.137, eq. 3.131 becomes

$$\Delta(\mathrm{KE}) = \frac{1}{2}(2\pi)\rho \int_0^{\pi} \left(\phi_v \frac{\partial \phi_v}{\partial r}\right)_s R^2 \sin\theta\, d\theta \tag{3.138}$$

$$= \pi\rho \int_{-1}^{1} \left(\phi_v \frac{\partial \phi_v}{\partial r}\right)_s R^2\, dx \tag{3.139}$$

$$= \pi\rho R^2 \left(\underbrace{A_0'^2 \sum_{\ell=1}^{\infty} \dot{\xi}_\ell \int_{-1}^{1} P_\ell(x) P_0(x)\, dx}_{①} + \underbrace{\sum_{\ell=1}^{\infty} \frac{\dot{\xi}_\ell^{\,2} R}{\ell} \int_{-1}^{1} P_\ell^2(x)\, dx}_{②} + \underbrace{\sum\sum_{\ell \neq m} \frac{\dot{\xi}_\ell \dot{\xi}_m R}{m} \int_{-1}^{1} P_\ell(x) P_m(x)\, dx}_{③} \right), \tag{3.140}$$

where the terms ① and ③ are zero because of the orthogonality of Legendre polynomial (see eq. 3.18). Due to the orthogonality of Legendre polynomial shown in eq. 3.18, we can determine the additional kinetic energy, $\Delta(\mathrm{KE})$, by determining the term ②, so

$$\Delta(\mathrm{KE}) = 2\pi\rho R^3 \sum_{\ell=1}^{\infty} \frac{\dot{\xi}_\ell^2}{\ell(2\ell+1)} = 2\pi\rho R^3 \sum_{\ell=1}^{\infty} \frac{1}{\ell(2\ell+1)} \left(\frac{\partial \xi_\ell}{\partial t}\right)^2. \tag{3.141}$$

Eq. 3.141 gives the change in the kinetic energy of the droplet where the surface starts to

deviate from the equilibrium position.

At this point, we know both the change in the potential energy, $\Delta(\mathrm{PE})$ (see eq. 3.121), and the change in the kinetic energy, $\Delta(\mathrm{KE})$ (see eq. 3.141), introduced by the surface perturbation. A pertubation shifts the position from the equilibrium. This changes the potential energy. However, the conservation is always valid. We also assume that the droplet fluid is inviscid. This results in the fact that the change in the potential energy transforms to the additional kinetic energy. We can adopt the Lagrange equation to find the equation of motion of the perturbed droplet surface in a manner similar to the case of a spring motion. First, the Lagrange equation [64] is

$$\frac{d}{dt}\left(\frac{\partial \mathcal{L}}{\partial \dot{\xi}_\ell}\right) - \frac{\partial \mathcal{L}}{\partial \xi_\ell} = 0 \quad ; \quad \dot{\xi}_\ell = \frac{\partial \xi_\ell}{\partial t}. \tag{3.142}$$

Next, as we already determined both $\Delta(\mathrm{PE})$ (see eq. 3.121) and $\Delta(\mathrm{KE})$ (see eq. 3.141), so we can determine Lagrangian, $\mathcal{L}$,

$$\begin{aligned} \mathcal{L} &= \Delta(\mathrm{KE}) - \Delta(\mathrm{PE}) && (3.143)\\ &= 2\pi\rho R^3 \sum_{\ell=1}^{\infty} \frac{1}{\ell(2\ell+1)} \left(\frac{\partial \xi_\ell}{\partial t}\right)^2 - 2\pi\sigma \sum_{\ell=1}^{\infty} \frac{(\ell+2)(\ell-1)\xi_\ell^2}{2\ell+1} \\ &\quad + \frac{Q^2}{8\pi\varepsilon_0} \sum_{\ell=1}^{\infty} \frac{(\ell-1)\xi_\ell^2}{(2\ell+1)R^3} && (3.144) \end{aligned}$$

and each term in eq. 3.142:

$$\begin{aligned} \frac{\partial \mathcal{L}}{\partial \xi_\ell} &= -4\pi\sigma\xi_\ell \frac{(\ell+2)(\ell-1)}{2\ell+1} + \frac{Q^2\xi_\ell}{4\pi\varepsilon_0 R^3} \frac{(\ell-1)}{2\ell+1} && (3.145)\\ \frac{d}{dt}\left(\frac{\partial \mathcal{L}}{\partial \dot{\xi}_\ell}\right) &= \frac{4\pi\rho R^3}{\ell(2\ell+1)} \frac{d^2\xi_\ell}{dt^2}. && (3.146) \end{aligned}$$

The terms stated in eq. 3.145 and 3.146 have to be substituted in the Lagrange equation which is in eq. 3.142. From this, we obtain the equation describing the surface evolution, which is

$$\frac{d^2\xi_\ell}{dt^2} + \frac{\ell(\ell-1)\xi_\ell}{\rho R^3}\left((\ell+2)\sigma - \frac{Q^2}{16\pi^2\varepsilon_0 R^3}\right) = 0. \tag{3.147}$$

It is reasonable to assume that the perturbation amplitude, ξ_ℓ, can be the time evolution function with the angular frequency, ω, so $\xi_\ell(t) \propto \exp(i\omega t)$ and $\frac{d^2\xi_\ell}{dt^2} = -\omega^2 \exp(i\omega t)$. From

this, we can solve for the dispersion relation by substituting $\xi_\ell(t)$ and $\frac{d^2\xi_\ell}{dt^2}$ to eq. 3.147, so the dispersion relation is

$$\omega^2 = \frac{\ell(\ell-1)}{\rho R^3}\left((\ell+2)\sigma - \frac{Q^2}{16\pi^2\varepsilon_0 R^3}\right), \tag{3.148}$$

which is Rayleigh's result [53, 59, 60]. By considering the dispersion relation in eq. 3.148, if $\ell = 0$ and 1, $\omega = 0$ always. This means that neither surface instability nor oscillation occurs if the perturbation are with the 0^{th} and 1^{st} modes. Therefore, the mode with $\ell \geq 2$ causes the motion of the surface. If $\omega^2 > 0$, the surface is stable with the oscillation. However, if $\omega^2 < 0$, there is an exponentially growing unstable solution. The stability limit is given by $\omega^2 = 0$, i.e.

$$(\ell+2)\sigma = \frac{Q^2}{16\pi^2\varepsilon_0 R^3} \tag{3.149}$$

$$Q = \sqrt{16\pi^2\varepsilon_0 R^3(\ell+2)\sigma}\,. \tag{3.150}$$

A charged droplet is unstable if

$$Q > \sqrt{16\pi^2\varepsilon_0 R^3(\ell+2)\sigma} \tag{3.151}$$

or

$$R < \left(\frac{Q^2}{16\pi^2\varepsilon_0(\ell+2)\sigma}\right)^{\frac{1}{3}} = r_{d,min}, \tag{3.152}$$

which is obtained by the rearrangement of eq. 3.151. $r_{d,min}$ is the minimum (or critical) droplet radius. The charged droplet undergoes instability if the surface charges are too much that the surface tension at the certain radius cannot overcome the electric force at the surface. It is clearly seen in eq. 3.151 and 3.152 that $\ell = 2$ is the most basic mode which allows the instability to initiate before other ℓ. In general, any practical perturbation is the superposition of the fundamental normal modes. (This is the reason that the perturbations in this study need to have a summation sign.) An arbitrary perturbation will include a component corresponding to the $\ell = 2$ mode. It is reasonable to use the stability limit of the 2^{nd} mode as the minimum requirement to initiate the charged droplet instability. In

this case, for $\ell = 2$, the droplet undergoes instability if

$$Q \;>\; \sqrt{64\pi^2\varepsilon_0 R^3\sigma} \tag{3.153}$$

or

$$R \;<\; \left(\frac{Q^2}{64\pi^2\varepsilon_0\sigma}\right)^{\frac{1}{3}} \;=\; r_{d,min}. \tag{3.154}$$

It is noticeable that $\ell = 2$ gives the biggest mimimum droplet radius prior to the instability initiation. In other words, $\ell = 2$ is the most sensitive mode for inducing the electrostatic instability.

3.1.2 Laboratory observations

Based on the work of Lord Rayleigh [53, 59], the instability of an excessively charged droplet, calculated from linear stability analysis, are predicted to behave in the form of ellipsoidal deformation with a pairs of jets ejecting from a pair of tips, which are called Taylor cones and located at the opposite ends. Each jet contains a group of secondary droplets, the size of which are much smaller than the primary droplet. However, in Rayleigh's time, practical observation was lacking to confirm the prediction.

The recent observation of an electrostatic breakup of a perturbed ethylene-glycol droplet by D. Duft *et al*, reported in ref. [56,57], are the first actual time-evolution pictures of the electrostatic breakup of a perturbed droplet. Those pictures have confirmed the prediction of the form of the electrostatic instability suggested by Lord Rayleigh [53, 59]. Also, D. Duft *et al* [56,57] reported that the jet transports out very small amount of mass, because each secondary droplet is very small compared to their mother droplet, i.e. the size of a secondary droplet can be a few orders smaller than that of a micron-size mother droplet, but carries a significant charge. The jets expel $\sim$ 33% of its charge, but only $\sim$ 0.3% of its mass [57]. After losing this charge, the primary droplet can re-stabilise. Hence, the very slightly smaller droplet reverses back to be stable with the smaller charge. Further (or repetitive) instabilities can be triggered by evaporation with the surface charge conservation. To see how the electrostatic breakup of a charged droplet behaves in detail, for that of an ethylene-glycol droplet, figure 1 of ref. [57], figures 1 and 4 of ref. [65] and

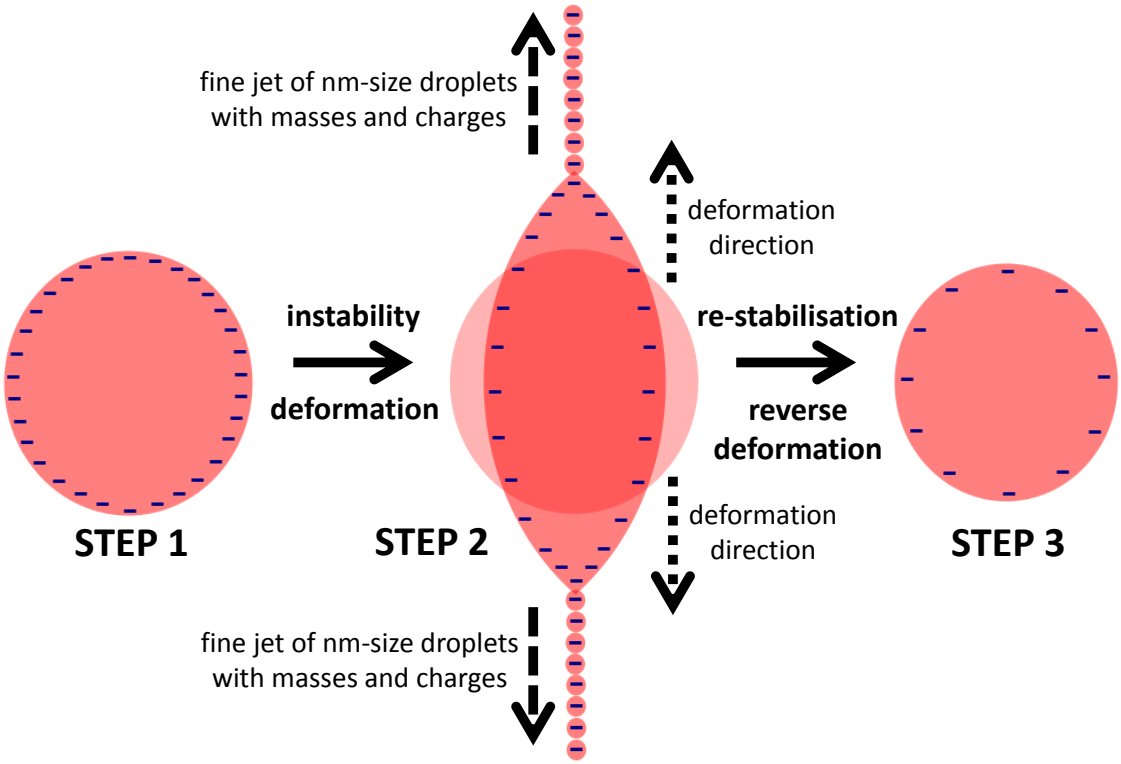


Figure 3.1: The picture simply illustrates the main features during an electrostatic breakup of a charged droplet in a vacuum. The picture is drawn by N. Somboonkittichai.

figure 4 of [66] are suggested and for that of a supercooled water droplet, figure 5 of ref. [66] is also suggested. The overall trend of very small mass loss but very large charge loss during each electrostatic instability are illustrated by figure 1 of ref. [56] and figure 2 of ref. [66]. However, we provide a simple picture as can be seen in figure 3.1, which contains the main steps appearing in the electrostatic breakup of a general charged droplet, for understanding.

3.2 Electrostatic breakup of a charged droplet in a misty plasma

A "misty plasma", defined by M. Coppins in ref. [54], is a plasma containing liquid droplets. A misty plasma shares many aspects of the physics of a dusty plasma. However, additional physics need to be considered. This results from the fact that a droplet in a plasma is mainly charged by electron deposition and then strongly responds to an electro-

magnetic field. From this, it is likely that electromagnetically induced hydrodynamics, i.e. electro- and magnetohydrodynamics, phenomena occur.

In this section, we concentrate on the determinations of the electrostatic stability limit of a droplet which is charged by a plasma. Also, the deposition of charged particles (ions and electrons) from the plasma can contribute momentum and then various momentum fluxes end up on the droplet and give rise to various pressures. In this section, we review the derivations of various pressures acting on the droplet surface. Ref. [54, 67] are the main references in the review in this section.

3.2.1 Stability of a small droplet in a plasma

As mentioned in eq. 3.152 in section 3.1, a charged droplet *in a vacuo* is unstable if

$$r_d \;<\; \left(\frac{Q^2}{16\pi^2\varepsilon_0(\ell+2)\sigma}\right)^{\frac{1}{3}} \;=\; r_{d,min}, \tag{3.155}$$

where r_d represents a droplet radius and $r_{d,min}$ is a minimum possible droplet radius prior to the instability initiation, which corresponds to the stability limit of any ℓ-th mode pertubation. In order to use it for the case of a droplet in a plasma, M. Coppins [54] modifies it in terms of a droplet floating potential, ϕ_d, a potential at which the rate of total charges deposited on the droplet is steady, independent of time. In order to obtain this form, we start by changing the charge, Q, on a droplet with

$$C \;=\; \frac{Q}{\phi_d}. \tag{3.156}$$

A stable droplet is perfectly spherical influenced by a surface tension. The capacitance, C, of a sphere is known as

$$C \;=\; 4\pi\varepsilon_0 r_d. \tag{3.157}$$

By eq. 3.156 and 3.157, Q can be stated as

$$4\pi\varepsilon_0 r_d = \frac{Q}{\phi_d} \tag{3.158}$$

$$Q = 4\pi\varepsilon_0 r_d \phi_d. \tag{3.159}$$

From this, we can transform the stability limit in the original form, stated in eq. 3.155, to the more appropriate form for being used in a plasma and it is

$$r_{d,min} = \left(\frac{Q^2}{16\pi^2\varepsilon_0(\ell+2)\sigma}\right)^{\frac{1}{3}} \tag{3.160}$$

$$r_{d,min} = \left(\frac{(4\pi\varepsilon_0 r_{d,min}\phi_d)^2}{16\pi^2\varepsilon_0(\ell+2)\sigma}\right)^{\frac{1}{3}} \tag{3.161}$$

$$r_{d,min}^3 = \frac{\varepsilon_0 r_{d,min}^2 \phi_d^2}{(\ell+2)\sigma} \tag{3.162}$$

$$r_{d,min} = \frac{\varepsilon_0 \phi_d^2}{(\ell+2)\sigma} \quad ; \quad \ell \geq 2, \tag{3.163}$$

where we assume $\ell \geq 2$ since the $\ell = 1$ mode is stable (see discussion following eq. 3.148) (adding after the PhD viva). For any ℓ, a charged droplet becomes unstable when $r_d < r_{d,min}$ where the surface tension of this size of droplet is not enough to overcome the repulsive electrostatic force. To be more specific for the case of $\ell = 2$,

$$r_{d,min} = \frac{\varepsilon_0 \phi_d^2}{4\sigma}, \tag{3.164}$$

which corresponds to ref. [54]. Since this equation has assumed the vacuum capacitance of a sphere (eq. 3.157), it is still valid only for very small ($r_d \ll \lambda_D$) droplets. In this limit, we can use the OML to obtain ϕ_d.

When a droplet is surrounded by a plasma, the Rayleigh electrostaic breakup should behave differently. Based on ref. [67], we expect that the restabilisation of the primary droplet in a plasma, after a large amount of charge is transported out of the Taylor cones, never occurs. This is because of the continuous charging by ion and electron depositions provided by a plasma environment. The floating potential, ϕ_d, remains constant, and as the unstable droplet becomes smaller it moves further from the stability boundary. Thus the charged droplet in the plasma completely disintegrates. With regard to the charged droplet *in vacuo*, the repetitive electrostatic instabilities and the associated restabilisations

remain until the droplet completely evaporates with the evaporation timescale. In contrast, the continuous single electrostatic instability completely disintegrates a charged droplet if the droplet is submerged in a plasma. This is a very rapid process with the electrostatic instability timescale not the evaporation timescale. This leads to the fact that at which the droplet undergoes electrostatic disintegration, the evaporation cannot compete with the electrostatic disintegration. For the examples of both timescales, the work of M. Coppins (2010) [54] is suggested for the clear understanding.

3.2.2 Pressures on a small droplet in a plasma

On a droplet, the general inwards pressure is done by a surface tension. This keeps a droplet to be spherical as a stable shape. If charges are introduced on the droplet, an outwards electrostatic pressure, when the charges configuration is steady with respect to time, is set up. These two pressures are general for the cases of a vacuum and a plasma. It is special for the case that a droplet is in a plasma because ions and electrons deposit on the droplet and give rise to extra pressures, i.e. ion and electron pressures, provided by ion and electron momentum fluxes. Moreover, ions and electrons accumulated on the droplet can recombined and provide an additional pressure after the neutral re-enters into a plasma. The last three pressures together with the surface tension are inwards and in the opposite direction to the electrostatic pressure. All pressures are considered at the steady state.

All pressures mentioned aboved are reviewed in this section. Based on ref.'s [54,67], especially, the electrostatic, ion, electron and neutral recombination pressures. Ref. [54, 67] are the main references in this section.

Pressure due to surface tension

Surface tension contributes produces a droplet with the lowest surface area for the given volume, which is achieved by being spherical in shape. If surface tension is the only extra force, it balances outwards resultant liquid pressure and then hydrostatic equilibrium is achieved. The surface tension results from the force provided by an interfacial liquid layer. In other words, the surface tension is provided by the intermolecular bonding force. The pressure due to surface tension depends on the size of the droplet. The general expression

of the pressure due to a surface tension, which can be found in ref. [68–70], is

$$P_{st} = N\sigma\left(\frac{r_1 + r_2}{r_1 r_2}\right), \tag{3.165}$$

where N is the number of interfacial layers, σ is a surface tension (N/m), and r_1 and r_2 are the principal curvature radii. A spherical droplet has only one principal radius, a droplet radius (r_d), and only one interfacial layer, $N = 1$. From this, the pressure due to surface tension is

$$P_{st} = \frac{2\sigma}{r_d}. \tag{3.166}$$

This is the pressure due to a surface tension of a stable spherical droplet.

Electrostatic pressure

The general expression of an electrostatic pressure [63] is

$$P_{es} = \frac{1}{2}\varepsilon_0 E^2, \tag{3.167}$$

where E is an electric field. An electric field of a spherical droplet can be written in

$$E = \frac{\phi_d}{r_d}. \tag{3.168}$$

An electrostatic pressure of a spherical droplet is

$$P_{es} = \frac{\varepsilon_0 \phi_d^2}{2r_d^2}, \tag{3.169}$$

where ϕ_d and r_d are an electrostatic potential on a droplet surface and a droplet radius, respectively. If a droplet is in a plasma, plasma particle depositions charge the droplet to the floating potential, ϕ_d, at steady state.

Ion and electron pressures

Ion and electron depositions govern not only charging mechanism on a droplet, reflected in the floating potential (ϕ_d), but also additional pressures. Ion and electron

pressures are provided by the physical momemtum fluxes from random (or thermal) ions and electrons. The depositions are controlled by the electric field corresponding to the floating potential (ϕ_d) on the droplet.

At a certain distance from a droplet, R, which is far enough to assume that the magnitude of the electric field produced from the droplet is negligible, a plasma particle moves randomly with a velocity, $v(R)$. A plasma particle is freely to move and get closer to the droplet. From this, it is expected that the plasma particle is eventually influenced by the electric field by the droplet. The plasma particle then responds to the electric field in a way which depends on its charge, i.e. a positive ion is either attracted towards the droplet or attractively scattered around the droplet, a low energy electron is repulsively scattered away from the droplet and a high energy electron can be successful in reaching the droplet. Along the way, we assume that the plasma particles have few collisions, i.e. we are considering a collisionless plasma. Another assumption is that there is no source and sink in the plasma, e.g. no production and loss by any mechanisms in the system. We can use the continuity equation to find the relationship between the particle flux at R and that at the droplet surface, r_d. Therefore, we starts from the continuity equation,

$$\frac{\partial n}{\partial t} + \nabla \cdot (n\mathbf{v}) \quad = \quad s. \tag{3.170}$$

There is no source and sink in the plasma fluid, $s = 0$, and the steady state is considered, so $\frac{\partial n}{\partial t} = 0$. We obtain

$$\nabla \cdot (n\mathbf{v}) \quad = \quad 0, \tag{3.171}$$

where n is a number density and $n\mathbf{v}$ is the particle flux (Γ) or the number of particles per unit time per unit area. Assuming spherical symmetry, eq. 3.171 becomes

$$\frac{1}{r^2}\frac{d}{dr}\left(r^2\Gamma_r\right) = 0, \tag{3.172}$$

where Γ_r is the radial component of the particle flux. Based on the conservation of the r-direction particle flux, at any time period the number of plasma particles passed through

the spherical cross-section area, $4\pi r^2$, the distances of R and r_d are constant, so we get

$$\Gamma_r(R)\,4\pi R^2\,\Delta t = \Gamma_r(r_d)\,4\pi r_d^2\,\Delta t \tag{3.173}$$

$$\Gamma_r(r_d) = \frac{R^2}{r_d^2}\Gamma_r(R), \tag{3.174}$$

where $\Gamma_r(R)$ and $\Gamma_r(r_d)$ are the radial particle flux at the radial distance R and r_d, both of which reach a droplet. In general, $\Gamma = \int_{all\ velocity\ space} \mathbf{v} f(\mathbf{r},\mathbf{v}) d^3\mathbf{r}$, where f is a distribution function at any $(\mathbf{r},\mathbf{v})$. To evaluate the pressure (or normal stress), P, we need to know the distribution functions of ions and electrons at the droplet surface, which are already distorted from the Maxwellian distribution function due the electric field of the droplet. For a simple picture about the distortion, figure 2.5 in P.C. Stangeby's book [17] is recommended. The Maxwellian distribution function is valid for both ions and electrons if they stay far enough from the charged droplet, i.e. the distance is R or further. Therefore, eq. 3.174 derived from the continuity equation can be used instead of $\Gamma_r(r_d)$ to avoid the mentioned problem. We are going to write the general expression of a pressure in terms of a moment integral of a distribution function [54], so the pressure are

$$P(r_d) = \frac{R^2}{r_d^2}\int_{all\ possible\ velocity\ space} m v_{r,d}\, v_{r,R} f(R,v)\, v_R^2 \sin\phi\, dv_R d\theta d\phi, \tag{3.175}$$

where m is a single mass of a particular plasma particle, either an ion or an electron and f is the Maxwellian distribution function at the radial distance R. The subscript R indicates the evaluation of any variable at the radial distance R, while the subscript d indicates the evaluation of any variable at the droplet surface. The coordinates used in eq. 3.175 satisfy the spherical coordinate system shown in figure 3.2, which is applied to both the cases of ion and electron pressures in this review.

First, we are going to calculate an ion pressure on a droplet with the use of the OML theory [38–40] where $r_d \ll \lambda_D$. The OML theory is used to calculate the ion current through the ion flux. The ion pressure is defined as deposited ion momentum flux. Therefore, to evaluate the ion pressure in same way as the ion current by the OML theory, we change from e, an elementary charge of a hydrogen ion or any singly charged ion, to $mv_{r,d}$, a single ion momentum at a droplet surface. We refer to the general pressure integral in eq. 3.175 with the neglect of the subscript R, i.e. $v_R \to v$. We evaluate an ion pressure at the droplet

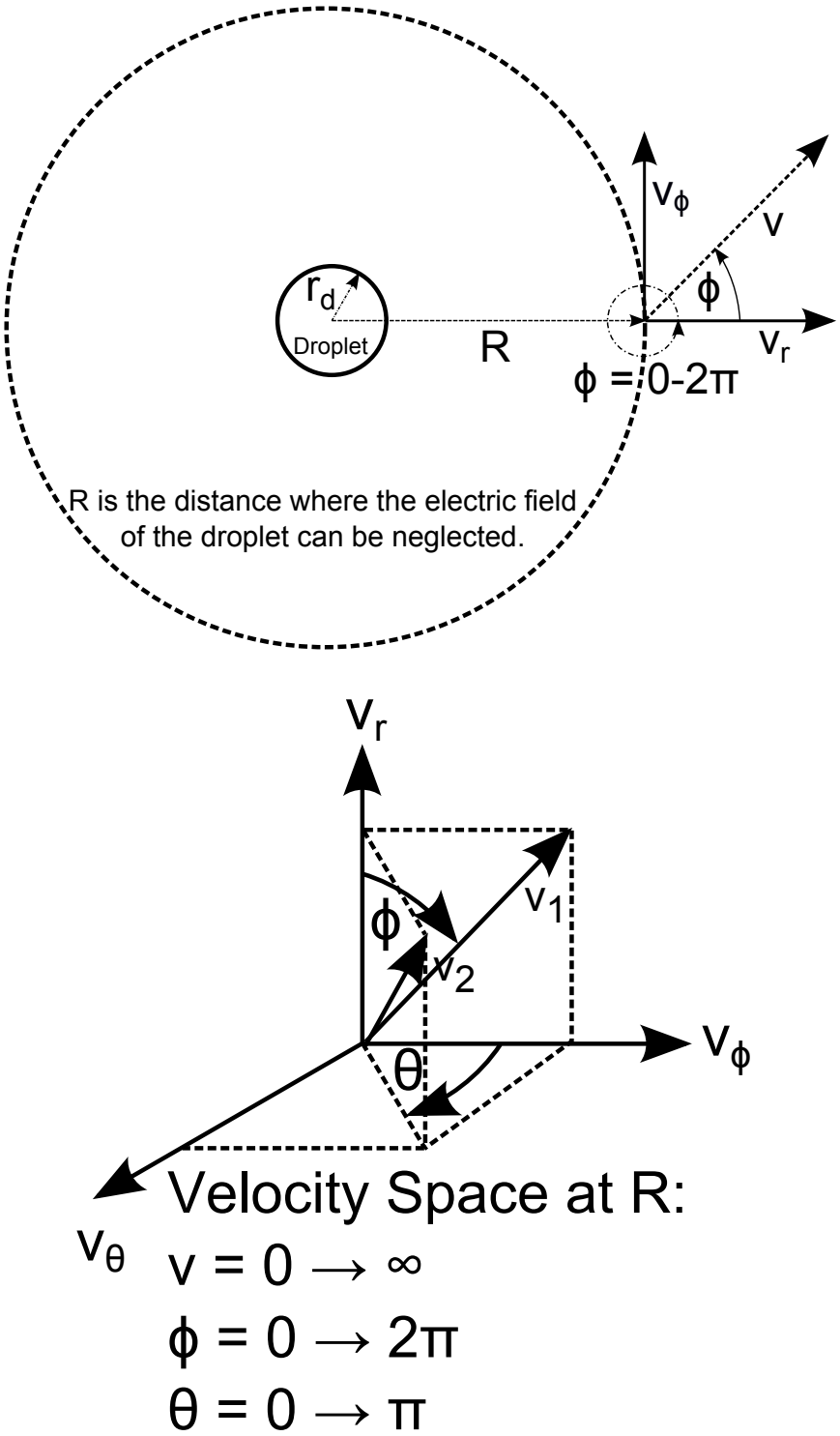


Figure 3.2: The above picture simply illustrates a droplet surrounded by a collisionless plasma where r_d is a droplet radius, R is the position where the droplet electric field is negligible and v, v_r and v_ϕ are the velocity of a plasma particle and its components, i.e. in the radial (r) and azimuthal (ϕ) direction, respectively. The lower picture shows velocity space at the position R where v_1 and v_2 are two examples of particle velocities in the three dimensions. v_r, v_ϕ and v_θ are the speed in the radial (r), azimuthal (ϕ) and polar (θ) directions. The pictures are drawn by N. Somboonkittichai.

surface with the variables of a faraway plasma. This can be achieved with the help of the conservation of angular momentum and energy of a collisionless single ion. With this, we can use a Maxwellian distribution function (f_M),

$$f_M = n_{i,0}\left(\frac{m_i}{2\pi kT_i}\right)^{\frac{3}{2}} \exp\left(-\frac{m_i v^2}{2kT_i}\right). \tag{3.176}$$

The ion pressure (eq. 3.175) with the Maxwellian distribution function (eq. 3.176) for ions can be written as

$$\begin{aligned} P_i(r_d) &= \frac{R^2}{r_d^2}\int_0^{\pi}\int_{\phi_1}^{\phi_2}\int_{v_1}^{v_2} m_i v_{r,d}\, v_r f_M\, v^2 \sin\phi\, dv d\phi d\theta & (3.177)\\ &= \frac{R^2}{r_d^2} m_i \pi \int_{\phi_1}^{\phi_2}\int_{v_1}^{v_2} v_{r,d}\, v \cos\phi f_M\, v^2 \sin\phi\, dv d\phi & (3.178)\\ &= \frac{R^2}{r_d^2} m_i \pi n_{i,0}\left(\frac{m_i}{2\pi kT_i}\right)^{\frac{3}{2}} \int_{v_1}^{v_2}\int_{\phi_1}^{\phi_2} \exp\left(-\frac{m_i v^2}{2kT_i}\right) v_{r,d}\, v^3 \cdot \\ &\quad \sin\phi\cos\phi\, d\phi dv. & (3.179) \end{aligned}$$

Due to the symmetry in the velocity space of a single ion in the θ-coordinate and that of a spherical dust grain, we can reduce the problem into two dimension of the velocity space, involved with the v- and ϕ-coordinates. Therefore, the integral of the θ-coordinate in eq. 3.179 is simply π. We need to change $v_{r,d}$ by the use of the conservation of angular momentum and energy of a collisionless single ion. We are considering a collisionless plasma. We are considering a single ion at the distance R, which is far enough from the charged droplet and the effect from the droplet electric field is negligible, the electrostatic potential, ϕ_E, $\to 0$, and the droplet surface, r_d. The conservation of energy of a single ion is therefore

$$\frac{1}{2}m_i v^2 = \frac{1}{2}m_i v_{r,d}^2 + \frac{1}{2}m_i v_{\phi,d}^2 + e\phi_d. \tag{3.180}$$

After a few rearrangements of eq. 3.180, we obtain

$$\begin{aligned} v_{r,d}^2 &= v^2 - v_{\phi,d}^2 - \frac{2e\phi_d}{m_i} & (3.181)\\ v_{r,d} &= \pm v\sqrt{1 - \frac{v_{\phi,d}^2}{v^2} - \frac{2e\phi_d}{m_i v^2}}. & (3.182) \end{aligned}$$

We choose

$$v_{r,d} = -v\sqrt{1-\frac{v_{\phi,d}^2}{v^2}-\frac{2e\phi_d}{m_i v^2}} \tag{3.183}$$

because we are considering the inward ion momentum flux at a droplet surface, so $v_{r,d}$ which is determined at the droplet surface should be in an inwards direction, i.e. the negative value. We adopt the conservation of angular momentum of a single ion to eliminate $v_{\phi,d}$. Because we reduce the problem to two dimension problem with the symmestries, the conservation of angular momentum of a single ion at at the distance R from the droplet and the droplet surface, r_d is thus

$$m_i(\mathbf{v}\times R\,\hat{r}) = m_i(\mathbf{v_d}\times r_d\,\hat{r}) \tag{3.184}$$

$$v_\phi R\,\hat{\theta} = v_{\phi,d} r_d\,\hat{\theta} \tag{3.185}$$

$$v_{\phi,d} = \frac{v_\phi R}{r_d}. \tag{3.186}$$

By substituting 3.186 into 3.183 and $v_\phi = v\sin\phi$, eq. 3.183 becomes

$$v_{r,d} = -v\sqrt{1-\frac{R^2}{r_d^2}\sin^2\phi-\frac{2e\phi_d}{m_i v^2}}. \tag{3.187}$$

By substituting 3.187 into 3.179,

$$P_i(r_d) = -\frac{R^2}{r_d^2} m_i \pi n_{i,0}\left(\frac{m_i}{2\pi k T_i}\right)^{\frac{3}{2}}\int_{v_1}^{v_2}\int_{\phi_1}^{\phi_2}\exp\left(-\frac{m_i v^2}{2kT_i}\right)v^4\cdot \sqrt{1-\frac{R^2}{r_d^2}\sin^2\phi-\frac{2e\phi_d}{m_i v^2}}\,\sin\phi\cos\phi\,d\phi dv. \tag{3.188}$$

The variable transformation, $u=\sqrt{\frac{m_i}{2kT_i}}v$ and $du=\sqrt{\frac{m_i}{2kT_i}}dv$, is required for the integration shown in eq. 3.188. Also, because the droplet is negatively charged with respect to the faraway plasma where the electrostatic potential is set up to be zero, the droplet then interacts with ions through an attractive force. This means that ions with all possible speed can be attracted through the electric field, so $v_1 = 0$ and $v_2 \to \infty$. After the use of the variable transformation mentioned above, $u_1 = 0$ and $u_2 \to \infty$. We also need to evaluate the values of ϕ_1 and ϕ_2. We start from the conservation of energy shown in eq. 3.187.

$v_{r,d} = 0$ is the condition where an ion just grazes the droplet surface and get deposited. This gives the critical angle limits, $\phi_{crit,min}$ and $\phi_{crit,max}$, where ions are collected over the range $\phi_{crit,min} \leq \phi \leq \phi_{crit,max}$.

$$
\begin{aligned}
v_{r,d} &= 0. && (3.189)\\
0 &= -v\sqrt{1-\frac{R^2}{r_d^2}\sin^2\phi_{crit}-\frac{2e\phi_d}{m_i v^2}}\,. && (3.190)\\
\sin^2\phi_{crit} &= \left(\frac{r_d}{R}\right)^2\left(1-\frac{2e\phi_d}{m_i v^2}\right). && (3.191)\\
\sin^2\phi_{crit} &= \left(\frac{r_d}{R}\right)^2\left(1-\frac{e\phi_d}{kT_i u^2}\right) \quad ; \quad u=\sqrt{\frac{m_i}{2kT_i}}v. && (3.192)\\
\phi_{crit} &= \sin^{-1}\left(\pm\frac{r_d}{R}\sqrt{1-\frac{e\phi_d}{kT_i u^2}}\right). && (3.193)
\end{aligned}
$$

Eq. 3.193 gives two values of ϕ_{crit}: $\phi_{crit,min} = \sin^{-1}\left(\frac{r_d}{R}\sqrt{1-\frac{e\phi_d}{kT_i u^2}}\right)$;and $\phi_{crit,max} = \sin^{-1}\left(-\frac{r_d}{R}\sqrt{1-\frac{e\phi_d}{kT_i u^2}}\right) = 2\pi - \sin^{-1}\left(\frac{r_d}{R}\sqrt{1-\frac{e\phi_d}{kT_i u^2}}\right)$. With these, the ion pressure integral in eq. 3.188 becomes

$$
\begin{aligned}
P_i(r_d) &= -\frac{R^2}{r_d^2}m_i\pi n_{i,0}\left(\frac{m_i}{2\pi kT_i}\right)^{\frac{3}{2}}\left(\frac{2kT_i}{m_i}\right)^{\frac{5}{2}}\int_0^\infty\int_{\phi_{crit,min}}^{\phi_{crit,max}}\exp\left(-u^2\right)u^4\cdot\\
&\quad\sqrt{1-\frac{R^2}{r_d^2}\sin^2\phi-\frac{e\phi_d}{kT_i u^2}}\,\sin\phi\cos\phi\,d\phi du. && (3.194)
\end{aligned}
$$

The symmetry around $\phi = 0$ allow $\int_{\phi_{crit,min}}^{\phi_{crit,max}}$ becoming $2\cdot\int_{\phi_{crit}}^{\pi}$ where $\phi_{crit,min}$ collapses to

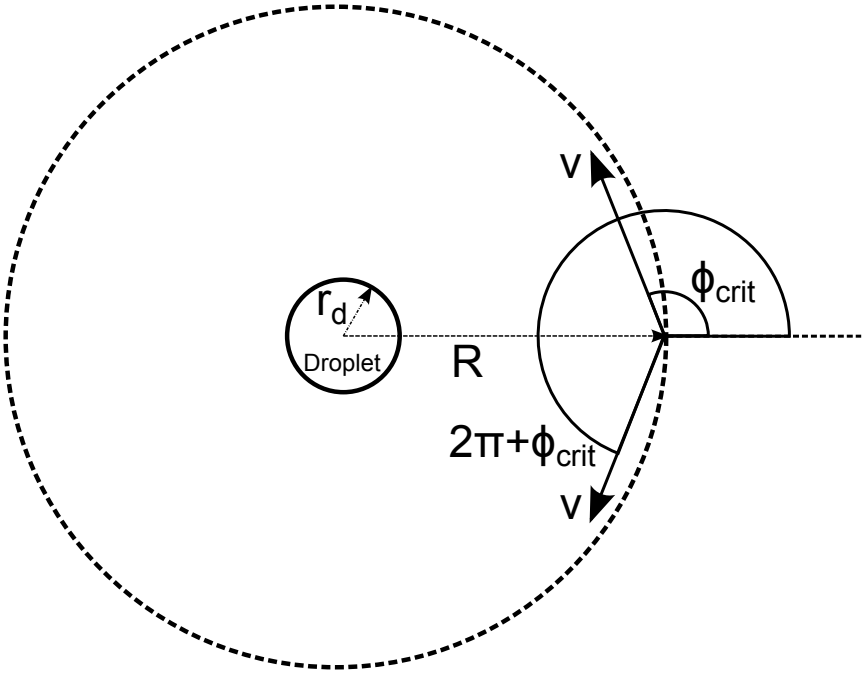


Figure 3.3: The picture shows the symmetry of $\phi_{crit,min}$ and $\phi_{crit,max}$ around $\phi = 0$, which can be used to reduce the work on the integration, i.e. $\int_{\phi_{crit,min}}^{\phi_{crit,max}} = 2 \cdot \int_{\phi_{crit}}^{\pi}$. The picture is drawn by N. Somboonkittichai.

ϕ_{crit}, which is clearly seen in figure 3.3. With this,

$$\begin{aligned} P_i(r_d) &= -2\frac{R^2}{r_d^2}\frac{n_{i,0}}{\sqrt{\pi}}\,2kT_i \int_0^\infty \int_{\phi=\phi_{crit}}^{\pi} \exp\left(-u^2\right) u^4 \cdot \\ &\quad \sqrt{1 - \frac{R^2}{r_d^2}\sin^2\phi - \frac{e\phi_d}{kT_i u^2}}\,\sin\phi\, d(\sin\phi)\, du \qquad (3.195) \\ P_i(r_d) &= -2\frac{R^2}{r_d^2}\frac{n_{i,0}}{\sqrt{\pi}}\,2kT_i \int_0^\infty \exp\left(-u^2\right) u^4 \cdot \\ &\quad \int_{\phi=\phi_{crit}}^{\pi} \frac{R}{r_d}\sqrt{\left(\frac{r_d}{R}\right)^2\left(1 - \frac{e\phi_d}{kT_i u^2}\right) - \sin^2\phi}\,\sin\phi\, d(\sin\phi)\, du \qquad (3.196) \\ P_i(r_d) &= -2\frac{R^3}{r_d^3}\frac{n_{i,0}}{\sqrt{\pi}}\,2kT_i \int_0^\infty \exp\left(-u^2\right) u^4 \cdot \\ &\quad \underbrace{\int_{\phi=\phi_{crit}}^{\pi} \sqrt{\left(\frac{r_d}{R}\right)^2\left(1 - \frac{e\phi_d}{kT_i u^2}\right) - \sin^2\phi}\,\sin\phi\, d(\sin\phi)}_{①}\, du. \qquad (3.197) \end{aligned}$$

With regard to term ① in eq. 3.197, the integral form of

$$\int \sqrt{c^2 - x^2}\, x dx = -\frac{1}{3}\left(c^2 - x^2\right)^{\frac{3}{2}}, \qquad (3.198)$$

which can be determined by the use of the variable transformation, $w^2 = c^2 - x^2$, where $x = \sin\phi$, so term ① in eq. 3.197 is

$$\begin{aligned} ① &= -\frac{1}{3}\left[\left(\left(\frac{r_d}{R}\right)^2\left(1-\frac{e\phi_d}{kT_iu^2}\right)-\sin^2\phi\right)^{\frac{3}{2}}\right]_{\phi_{crit}}^{\pi} && (3.199)\\ &= -\frac{1}{3}\left(\left(\frac{r_d}{R}\right)^2\left(1-\frac{e\phi_d}{kT_iu^2}\right)-\underbrace{\sin^2\pi}_{=0}\right)^{\frac{3}{2}} \\ &\quad +\frac{1}{3}\left(\underbrace{\left(\frac{r_d}{R}\right)^2\left(1-\frac{e\phi_d}{kT_iu^2}\right)-\sin^2\phi_{crit}}_{=0}\right)^{\frac{3}{2}} && (3.200)\\ &= -\frac{1}{3}\left(\frac{r_d}{R}\right)^3\left(1-\frac{e\phi_d}{kT_iu^2}\right)^{\frac{3}{2}}. && (3.201)\end{aligned}$$

By substituting term ① above into eq. 3.197, we obtain

$$P_i(r_d) = \frac{4}{3}\frac{n_{i,0}}{\sqrt{\pi}}kT_i\int_0^\infty \exp\left(-u^2\right)u^4\left(1-\frac{e\phi_d}{kT_iu^2}\right)^{\frac{3}{2}}du \qquad (3.202)$$

$$P_i(r_d) = \frac{4}{3}\frac{n_{i,0}}{\sqrt{\pi}}kT_i\underbrace{\int_0^\infty u\,\exp\left(-u^2\right)\left(u^2-\frac{e\phi_d}{kT_i}\right)^{\frac{3}{2}}du}_{②}. \qquad (3.203)$$

To solve term ② in eq. 3.203, the variable transformation, $w^2 = u^2 - \frac{e\phi_d}{kT_i}$ is required. From this,

$$\begin{aligned} ② &= \int_0^\infty u\,\exp\left(-u^2\right)\left(u^2-\frac{e\phi_d}{kT_i}\right)^{\frac{3}{2}}du && (3.204)\\ &= \exp\left(-\frac{e\phi_d}{kT_i}\right)\int_{\sqrt{-\frac{e\phi_d}{kT_i}}}^\infty w^4\exp\left(-w^2\right)dw && (3.205)\\ &= \exp\left(-\frac{e\phi_d}{kT_i}\right)\left[-\frac{w^3}{2}\exp\left(-w^2\right)-\frac{3}{4}w\exp\left(-w^2\right)\right]_{\sqrt{-\frac{e\phi_d}{kT_i}}}^\infty \\ &\quad +\frac{3}{4}\exp\left(-\frac{e\phi_d}{kT_i}\right)\int_{\sqrt{-\frac{e\phi_d}{kT_i}}}^\infty\exp\left(-w^2\right)dw && (3.206)\end{aligned}$$

by the use of the integration by parts. After substituting the limit of the integrations and the relationship, $\mathrm{erfc}(x) = 1 - \mathrm{erf}(x) = \frac{2}{\sqrt{\pi}}\int_x^\infty \exp\left(-t^2\right)dt$, where $\mathrm{erf}(x)$ is an error

function and erfc(x) is a complementary error function, we obtain

$$② = -\frac{1}{2}\frac{e\phi_d}{kT_i}\sqrt{-\frac{e\phi_d}{kT_i}} + \frac{3}{4}\sqrt{\frac{-e\phi_d}{kT_i}} + \frac{3}{4}\exp\left(-\frac{e\phi_d}{kT_i}\right)\frac{\sqrt{\pi}}{2}\,\mathrm{erfc}\left(\sqrt{-\frac{e\phi_d}{kT_i}}\right). \quad (3.207)$$

For the convenience of writing the ion pressure, we define $\Phi_d = -\frac{e\phi_d}{kT_e}$ and $\hat{\Phi}_d = -\frac{e\phi_d}{kT_i} = \frac{\Phi_d}{\beta}$, where $\beta = \frac{T_i}{T_e}$. By substituting the term ② in eq. 3.207 back into eq. 3.203 combined with a few rearrangements, we obtain the OML ion pressure, which can be written as

$$P_i(r_d) = \frac{1}{2}n_{i,0}kT_i\left(2\left(\frac{2}{3}\hat{\Phi}_d + 1\right)\sqrt{\frac{\hat{\Phi}_d}{\pi}} + \exp\left(\hat{\Phi}_d\right)\mathrm{erfc}\left(\sqrt{\hat{\Phi}_d}\right)\right). \quad (3.208)$$

This is the OML ion pressure for $r_d \leq \lambda_D$. We note that if $T_i = T_e$, $\Phi_d = \hat{\Phi}_d$.

Next, we are going to calculate the OML electron pressure at a droplet surface, $P_e(r_d)$. Most steps of the calculations are the same as those of the OML ion pressure. From this, we are going to summarise the calculation of the OML electron pressure in fewer steps. We starts with the use of an electron Maxwellian distribution function (f_M),

$$f_M = n_{e,0}\left(\frac{m_e}{2\pi kT_e}\right)^{\frac{3}{2}}\exp\left(-\frac{m_e v^2}{2kT_e}\right), \quad (3.209)$$

and eq. 3.209 is substituted into the general pressure integration in eq. 3.175. We also use the same assumptions of the symmetries used in the calculation of the OML ion pressure mentioned above and f_M in eq. 3.209 is substituted into 3.211, so

$$P_e(r_d) = \frac{R^2}{r_d^2}\int_0^{\pi}\int_{\phi_1}^{\phi_2}\int_{v_1}^{v_2} m_e v_{r,d}\, v_r f_M\, v^2 \sin\phi\, dv d\phi d\theta \quad (3.210)$$

$$= \frac{R^2}{r_d^2} m_e \pi \int_{v_1}^{v_2}\int_{\phi_1}^{\phi_2} v_{r,d}\, v_r f_M\, v^2 \sin\phi\, d\phi dv \quad (3.211)$$

$$= \frac{R^2}{r_d^2} m_e \pi n_{e,0}\left(\frac{m_e}{2\pi kT_e}\right)^{\frac{3}{2}}\int_{v_1}^{v_2}\int_{\phi_1}^{\phi_2}\exp\left(-\frac{m_e v^2}{2kT_e}\right) v_{r,d}\, v^3 \cdot \sin\phi\cos\phi\, d\phi dv, \quad (3.212)$$

where $v_r = v\cos\phi$. Again, similar to the case of ions, the subscripts d and R refer to the positions at a droplet surface and at the far enough from the droplet where the electric field of the droplet is negligible. In addition, v_R is collapsed to v. The conservation of energy of

a collisionless single electron, where a collisionless plasma is assumed,

$$\frac{1}{2}m_e v^2 = \frac{1}{2}m_e v_{r,d}^2 + \frac{1}{2}m_e v_{\phi,d}^2 - e\phi_d. \tag{3.213}$$

With a few rearrangements, we obtain

$$v_{r,d}^2 = v^2 - v_{\phi,d}^2 + \frac{2e\phi_d}{m_e} \tag{3.214}$$

$$v_{r,d} = \pm v\sqrt{1 - \frac{v_{\phi,d}^2}{v^2} + \frac{2e\phi_d}{m_e v^2}}\,. \tag{3.215}$$

We choose $v_{r,d} = -v\sqrt{1 - \frac{v_{\phi,d}^2}{v^2} + \frac{2e\phi_d}{m_e v^2}}$ because the electron momentum flux is in an inwards direction. Also referring to the conservation of angular momentum of a single ion, that of a single momentum is written in the same way, which is $v_{\phi,d} = \frac{v_\phi R}{r_d}$, and $v_\phi = v\sin\phi$. Subsequently, the conservations of energy and angular momentum mentioned so far give

$$v_{r,d} = -v\sqrt{1 - \frac{R^2}{r_d^2}\sin^2\phi + \frac{2e\phi_d}{m_e v^2}}\,. \tag{3.216}$$

Eq. 3.216 is substituted into eq. 3.212. Furthermore, with the variable transformation, $u = \sqrt{\frac{m_e}{2kT_e}}\,v$ and $du = \sqrt{\frac{m_e}{2kT_e}}\,dv$, eq. 3.212 becomes

$$\begin{aligned} P_e(r_d) &= -\frac{R^2}{r_d^2}m_e\pi n_{e,0}\left(\frac{m_e}{2\pi kT_e}\right)^{\frac{3}{2}}\left(\frac{2kT_e}{m_e}\right)^{\frac{5}{2}}\int_{u_1}^{u_2}\int_{\phi_1}^{\phi_2}\exp\left(-u^2\right)u^4\cdot \\ &\quad \sqrt{1 - \frac{R^2}{r_d^2}\sin^2\phi + \frac{e\phi_d}{kT_e u^2}}\,\sin\phi\cos\phi\,d\phi du \qquad (3.217) \\ &= -\frac{R^2}{r_d^2}\frac{n_{e,0}}{\sqrt{\pi}}\,2kT_e\int_{u_1}^{u_2}u^4\exp\left(-u^2\right)\int_{\phi_1}^{\phi_2}\frac{R}{r_d}\sqrt{\left(\frac{r_d}{R}\right)^2\left(1 + \frac{e\phi_d}{kT_e u^2}\right) - \sin^2\phi}\,\cdot \\ &\quad \sin\phi\cos\phi\,d\phi du. \qquad (3.218) \end{aligned}$$

From eq. 3.216, we are determining the ϕ limit in the integration shown in eq. 3.229 for an

electron can glaze a droplet surface by considering $v_{r,d} = 0$, so

$$\begin{aligned} v_{r,d} &= 0 && (3.219)\\ 0 &= -v\sqrt{1 - \frac{R^2}{r_d^2}\sin^2\phi + \frac{2e\phi_d}{m_e v^2}} && (3.220)\\ \sin^2\phi_{crit} &= \left(\frac{r_d}{R}\right)^2\left(1 + \frac{e\phi_d}{kT_e u^2}\right) && (3.221)\\ \phi_{crit} &= \sin^{-1}\left(\pm\frac{r_d}{R}\sqrt{1 + \frac{e\phi_d}{kT_e u^2}}\right). && (3.222) \end{aligned}$$

We define $\phi_{crit,min} = \phi_{crit} = \sin^{-1}\left(\frac{r_d}{R}\sqrt{1 + \frac{e\phi_d}{kT_e u^2}}\right)$ and $\phi_{crit,max} = \sin^{-1}\left(-\frac{r_d}{R}\sqrt{1 + \frac{e\phi_d}{kT_e u^2}}\right) = 2\pi - \phi_{crit}$. About the u limit in the integration, eq. 3.229, u_1 is corresponding to the stopping potential of a charged droplet where the electric field is repulsive and blocks low energy electrons to reach the droplet, while only high energy or speed electrons can reach the droplet. This results in $u_2 \to \infty$. For u_1,

$$\begin{aligned} \frac{1}{2}m_e v_1^2 &= -e\phi_d && (3.223)\\ v_1 &= \sqrt{\frac{-2e\phi_d}{m_e}} && (3.224)\\ u_1 &= \sqrt{\frac{m_e}{2kT_e}}\, v_1 && (3.225)\\ u_1 &= \sqrt{\frac{m_e}{2kT_e}}\sqrt{\frac{-2e\phi_d}{m_e}} && (3.226)\\ u_1 &= \sqrt{\frac{-e\phi_d}{kT_e}}. && (3.227) \end{aligned}$$

Furthermore, due to the symmestries, which is the same as the case of ions and can be seen in figure 3.3, $\int_{\phi_{crit,min}}^{\phi_{crit,max}} = 2 \cdot \int_{\phi_{crit}}^{\pi}$. By the known u and ϕ limits of integration, we adopt

them in eq. 3.229 and then

$$P_e(r_d) = -\frac{R^3}{r_d^3}\frac{n_{e,0}}{\sqrt{\pi}}\,4kT_e\int_{\sqrt{\frac{-e\phi_d}{kT_e}}}^{\infty} u^4\,\exp\left(-u^2\right)\cdot \int_{\phi_{crit}}^{\pi}\sqrt{\left(\frac{r_d}{R}\right)^2\left(1+\frac{e\phi_d}{kT_eu^2}\right)-\sin^2\phi}\,\sin\phi\cos\phi\,d\phi du \tag{3.228}$$

$$= -\frac{R^3}{r_d^3}\frac{n_{e,0}}{\sqrt{\pi}}\,4kT_e\int_{\sqrt{\frac{-e\phi_d}{kT_e}}}^{\infty} u^4\,\exp\left(-u^2\right)\cdot \underbrace{\int_{\phi=\phi_{crit}}^{\pi}\sqrt{\left(\frac{r_d}{R}\right)^2\left(1+\frac{e\phi_d}{kT_eu^2}\right)-\sin^2\phi}\,\sin\phi\,d(\sin\phi)}_{①}\,du. \tag{3.229}$$

Similar to the case of ions, with the variable transformation, $u^2 = c^2 + x^2$ where $x = \sin\phi$ as can be seen in eq. 3.198, comparing the integral form of $\int\sqrt{c^2-x^2}\,xdx = -\frac{1}{3}\left(c^2-x^2\right)^{\frac{3}{2}}$ with term ① in eq. 3.229 makes us know the solution for term ① in eq. 3.229, so

$$① = -\frac{1}{3}\left[\left(\left(\frac{r_d}{R}\right)^2\left(1+\frac{e\phi_d}{kT_eu^2}\right)-\sin^2\phi\right)^{\frac{3}{2}}\right]_{\phi_{crit}}^{\pi} \tag{3.230}$$

$$= -\frac{1}{3}\left(\frac{r_d}{R}\right)^3\left(1+\frac{e\phi_d}{kT_eu^2}\right)^{\frac{3}{2}}. \tag{3.231}$$

This is with the help of eq. 3.222. By substituting term ① in eq. 3.231 into the OML electron pressure shown in eq. 3.229, we acquire

$$P_e(r_d) = \frac{4}{3}\frac{n_{e,0}}{\sqrt{\pi}}\,kT_e\int_{\sqrt{\frac{-e\phi_d}{kT_e}}}^{\infty} u^4\,\exp\left(-u^2\right)\left(1+\frac{e\phi_d}{kT_eu^2}\right)^{\frac{3}{2}}du \tag{3.232}$$

$$= \frac{4}{3}\frac{n_{e,0}}{\sqrt{\pi}}\,kT_e\underbrace{\int_{\sqrt{\frac{-e\phi_d}{kT_e}}}^{\infty} u\,\exp\left(-u^2\right)\left(u^2+\frac{e\phi_d}{kT_e}\right)^{\frac{3}{2}}du}_{②}. \tag{3.233}$$

As can be seen term ② in eq. 3.233, we refers to the integration by parts in eq. 3.206, which is used for term ② of the OML ion pressure illustrated in eq. 3.203, with the variable transformation, $w^2 = u^2 + \frac{e\phi_d}{kT_e}$. The integration by parts technique used for determining term ② in eq. 3.203 in the case of ions can be applied to term ② in eq. 3.233 for the case

of electrons. Thus,

$$
\begin{aligned}
② &= \int_{\sqrt{\frac{-e\phi_d}{kT_e}}}^{\infty} u \exp\left(-u^2\right) \left(u^2 + \frac{e\phi_d}{kT_e}\right)^{\frac{3}{2}} du && (3.234)\\
&= \exp\left(\frac{e\phi_d}{kT_e}\right) \int_0^{\infty} w^4 \exp\left(w^2\right) dw && (3.235)\\
&= \exp\left(\frac{e\phi_d}{kT_e}\right) \left[-\frac{w^3}{2} \exp\left(-w^2\right) - \frac{3}{4} w \exp\left(-w^2\right)\right]_0^{\infty} \\
&\quad + \frac{3}{4} \exp\left(\frac{e\phi_d}{kT_e}\right) \int_0^{\infty} \exp\left(-w^2\right) dw && (3.236)\\
&= \frac{3}{8}\sqrt{\pi} \exp\left(\frac{e\phi_d}{kT_e}\right) && (3.237)
\end{aligned}
$$

with the use of the integral form $\int_0^{\infty} \exp\left(-x^2\right) dx = \frac{\sqrt{\pi}}{2}$. We perform the substitution of eq. 3.237 into eq. 3.233, so

$$
\begin{aligned}
P_e(r_d) &= \frac{4}{3} \frac{n_{e,0}}{\sqrt{\pi}} kT_e \left(\frac{3}{8}\sqrt{\pi} \exp\left(\frac{e\phi_d}{kT_e}\right)\right) && (3.238)\\
&= \frac{1}{2} n_{e,0} kT_e \exp\left(\frac{e\phi_d}{kT_e}\right) && (3.239)\\
&= \frac{1}{2} n_{e,0} kT_e \exp\left(-\Phi_d\right), && (3.240)
\end{aligned}
$$

where $\Phi_d = -\frac{e\phi_d}{kT_e}$. This is the OML electron pressure which valid at $r_d \leq \lambda_D$. Finally, unlike the normal gas pressure, $P = nkT$, it is noticeble that the factor of $\frac{1}{2}$ in $P_i(r_d)$ (see eq. 3.208) and $P_e(r_d)$ (see eq. 3.240) is due to the fact that each ion or electron is absorbed (not reflected) at the droplet surface and thus provides the momentum of $m_i v_r$ or $m_e v_r$ not $2m_i v_r$ or $2m_e v_r$.

Pressure due to neutral recombination

If both positive plasma ion and electron reach a droplet surface, the ion recombines with the electron on the droplet surface and then forms a neutral atom. This not only gives an additional energy but also an inward momentum to the droplet. The latter occurs when the neutral atom re-enters the plasma with the same momentum, this imparts an equal and opposite momentum to the surface. This process is expected to happen at thermal equilibrium with the droplet. All of this is the main features of the neutral recombination process.

M. Coppins suggests in his work [67] the simple formula of a pressure due to a neutral recombination. We start from the steady state assumption that ions and electrons reach a droplet surface with the same rate, so the total current is zero, $\frac{dQ_d}{dt} = 0$. This is used to determine ϕ_d through the OML ion and electron current. We also assume that all ions and electrons recombined at the droplet surface and then re-enter the surrounding plasma. In other words, the rate of ions or electrons reaching the droplet surface is equal to the rate of the re-entering of the neutral atoms into the plasma. Therefore, we choose to determine the pressure due to neutral recombination, P_r, by the use of the electron current (I_e), while we also can start with the ion current (I_i). The OML electron current, I_e, is mentioned in eq. 1.4,

$$I_e = 4\pi r_d^2 n_{e,0} e \sqrt{\frac{kT_e}{2\pi m_e}} \exp\left(\frac{e\phi_d}{kT_e}\right). \tag{3.241}$$

The general electrical current, I, on the droplet surface is

$$I = \mathbf{j} \cdot \mathbf{A} \tag{3.242}$$

$$= 4\pi r_d^2 q \Gamma_r. \tag{3.243}$$

This means that the radial electron flux, $\Gamma_{r,e}$, can be written as

$$\Gamma_{r,e} = -n_{e,0} \sqrt{\frac{kT_e}{2\pi m_e}} \exp\left(\frac{e\phi_d}{kT_e}\right). \tag{3.244}$$

We assume the neutral atom which is formed in the recombination process is in thermal equilibrum with the droplet surface, i.e. the neutrals form a Maxwellian distribution at the temperature T_d (= droplet temperature), therefore the average neutral speed is $\bar{c} = \sqrt{\frac{8kT_d}{\pi m_i}}$, and thus, the pressure due to neutral recombination, P_r, becomes

$$P_r = -m_i \bar{c} \Gamma_{r,e} \tag{3.245}$$

$$= -m_i \sqrt{\frac{8kT_d}{\pi m_i}} \left(-n_{e,0} \sqrt{\frac{kT_e}{2\pi m_e}} \exp\left(\frac{e\phi_d}{kT_e}\right) \right) \tag{3.246}$$

$$= \frac{2}{\pi} n_{e,0} k \sqrt{\frac{m_i T_d T_e}{m_e}} \exp\left(\frac{e\phi_d}{kT_e}\right). \tag{3.247}$$

This corresponds to the formula of P_r in ref. [54]. For future reference, we note that for all

cases of material, this pressure is negligible.

Chapter 4

STABILITY OF A LARGE DROPLET IN A PLASMA

At the beginning of this chapter, the validity of the use of the original Rayleigh stability limit for a plasma system is explored (section 4.1). This chapter then focuses on the derivation of a version of Rayleigh's stability limit for a large, plasma immersed droplet (section 4.2) and the comparisons between the use of OML and MOML theories for determining the droplet stability are provided for three widely known plasma systems, i.e. fusion plasmas in tokamaks (section 4.3.1), low pressure plasmas (section 4.3.2) and high pressure plasmas (section 4.3.3). The overview of the trends of the OML and MOML floating potential with some parameters is also mentioned at the beginning of section 4.3.

4.1 Validity of Rayleigh's droplet stability limit in a plasma

As mentioned in section 3.1, the stability of a charged droplet is associated only with a surface tension and an outward electrostatic force. An infinitesimal perturbation applied on the droplet surface changes the surface area of the droplet. This result in an addition work (or surface enegy) from the surface tension. Furthermore, when the surface area is changed, the surface charge configuration on the droplet also deviates from the initial configuration. As a result of this, the electrostatic potential energy changes. These changes then transform into kinetic energy to drive the motion of the droplet surface. With enough charge, the electrostatic instability (breakup or disintegration) can be initiated.

In the case that a droplet is in a plasma and charged by collecting ions and electrons from the plasma, the droplet is additionally influenced by external pressures, i.e. ion and electron pressures and a pressure due to neutral recombination. At first glance, it looks like the external pressures should stabilise the droplet by opposing very strong electrostatic force. However, the droplet is harder to be compressed in contrast to a bubble. With this reason, the liquid is very nearly incompressible. This means that the liquid density and the volume of the droplet never change. From this, no work is done by external pressure. In other words, in the case of a droplet in a plasma, no work due to either compression or expansion has to be added in the equation of the droplet surface motion calculated by the Lagrange method (see eq. 3.147) because the droplet is incompressible. Thus, the dispersion relation which a droplet is *in a vacuo* can be further used even though a droplet is in a plasma. This leads to the fact that original Rayleigh's stability limit [53, 59] as well as its modified form provided by M. Coppins (2010) [54] are still reasonable for indicating the unstable condition of a charged droplet in a plasma.

4.2 Derivation

In this chapter, we are going to consider the minimum possible droplet radius, $r_{d,min}$ at the regime which $r_{d,min} > \lambda_D$. We use the stability limit shown in eq. 3.164, i.e.

$$r_{d,min} = \frac{\varepsilon_0 \phi_{d,MOML}^2}{4\sigma}, \tag{4.1}$$

combined with the floating potential determined by the modified orbital motion limited (MOML) theory, $\phi_{d,MOML}$, the work of which was done by C.T.N. Willis *et al* [42]. The MOML method is used to determine the floating potential when the droplet radius is larger than the Debye length, $r_d > \lambda_D$. The MOML floating potential can be found by the formula [42],

$$\exp\left(\frac{\phi_{d,MOML}}{T_e[eV]}\right) = \sqrt{\frac{\beta m_e}{m_i}}\left(1 - \frac{\phi_{d,MOML}}{\beta T_e[eV]} + \frac{1}{2\beta}\ln\left(2\pi\frac{m_e}{m_i}(1+\gamma\beta)\right)\right). \tag{4.2}$$

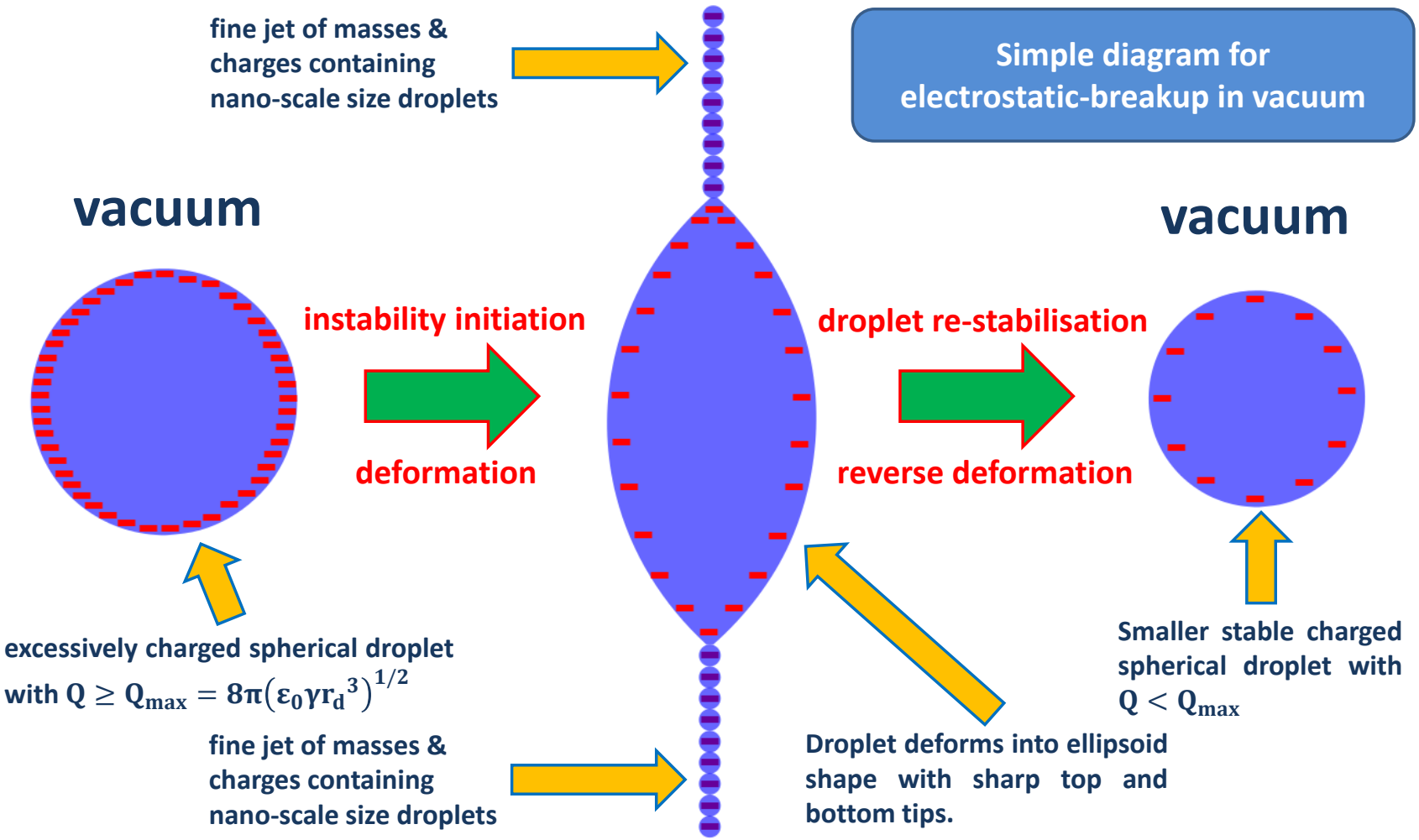


Figure 4.1: The simple picture explaining the main features on the electrostatic breakup of a charged droplet *in a vacuo*. (This picture is drawn by N. Somboonkittichai.)

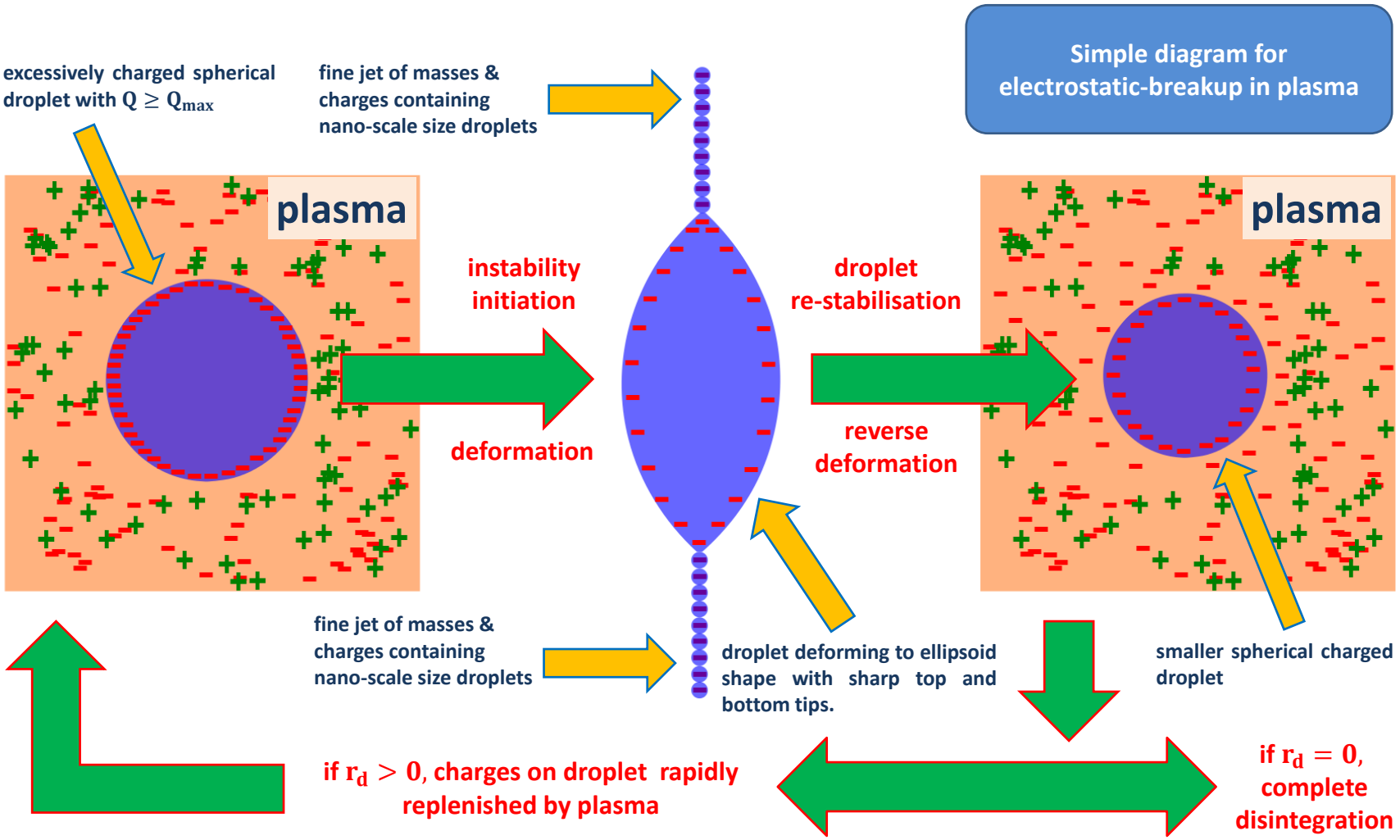


Figure 4.2: The simple picture explaining the main features on the electrostatic breakup of a charged droplet in a misty plasma. (This picture is drawn by N. Somboonkittichai.)

In the MOML formula in eq. 4.2 for a floating potential of a large spherical object, the thin planar sheath is assumed and indicated by the extra term shown by the last term on the right-handed side of eq. 4.2 compared to the OML formula shown in eq. 1.1. We are going to compare $r_{d,min}$ associated with both the OML and the MOML methods under the condition of no electron emissions, so $\delta_{tot} = 0$. The details for $r_{d,min}$ of the OML method can be seen in section 3.2.1.

Based on ref. [54, 67], the comment on the difference between the electrostatic breakup *in a vacuo* and in a misty plasma is that there is no restabilisation occuring for the case of a charged droplet in a plasma. This enhances the droplet disintegration especially in a fusion plasma. This process results in the complete and fast disintegration at a certain droplet radius, as we call $r_{d,min}$. Furthermore, by the comparison between the time scales of evaporation and electrostatic instability stated in [54], the complete electrostatic disintegration of a charged droplet in a misty plasma is much faster than the droplet evaporation process. This implies that there is a cut-off of the possible sizes of droplets which survive in various plasma systems.

The simple pictures of both cases are shown on figures 4.1 and 4.2 for further comparison and understanding.

4.3 Results

In this section, the main objective is to provide the trend of the droplet stability in terms of the plot between the minimum radius ($r_{d,min}$) of a charged droplet before undergoing electrostatic breakup and electron temperature (T_e) for some well-known plasma systems: a fusion plasma in a tokamak; a low temperature and density plasma; and plasma spraying which represents a high pressure plasma system. However, before reaching that point, the characteristics of floating potentials (ϕ_d) calculated by using the OML ($\phi_{d,OML}$) [38–40] and the MOML ($\phi_{d,MOML}$) [42] theories and their comparison need to be clearly justified. First of all, we do not consider the electron emissions, so $\delta_{tot} = 0$. We then use three approximations:

1. Mass of a single proton are the same as that of a single neutron, which equals to

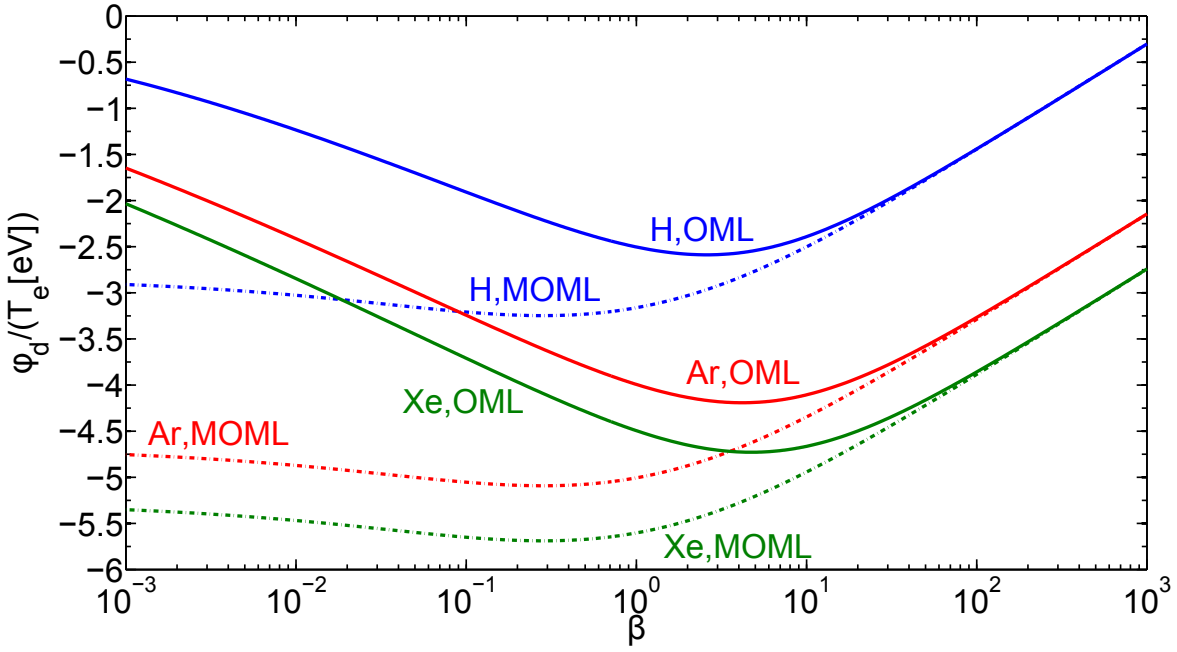


Figure 4.3: The plot between the ratio of ϕ_d and T_e (T_e in eV unit) and β by the OML (——) and MOML (-·-·-) charging model for hydrogen (H), argon (Ar) and xenon (Xe) plasmas.

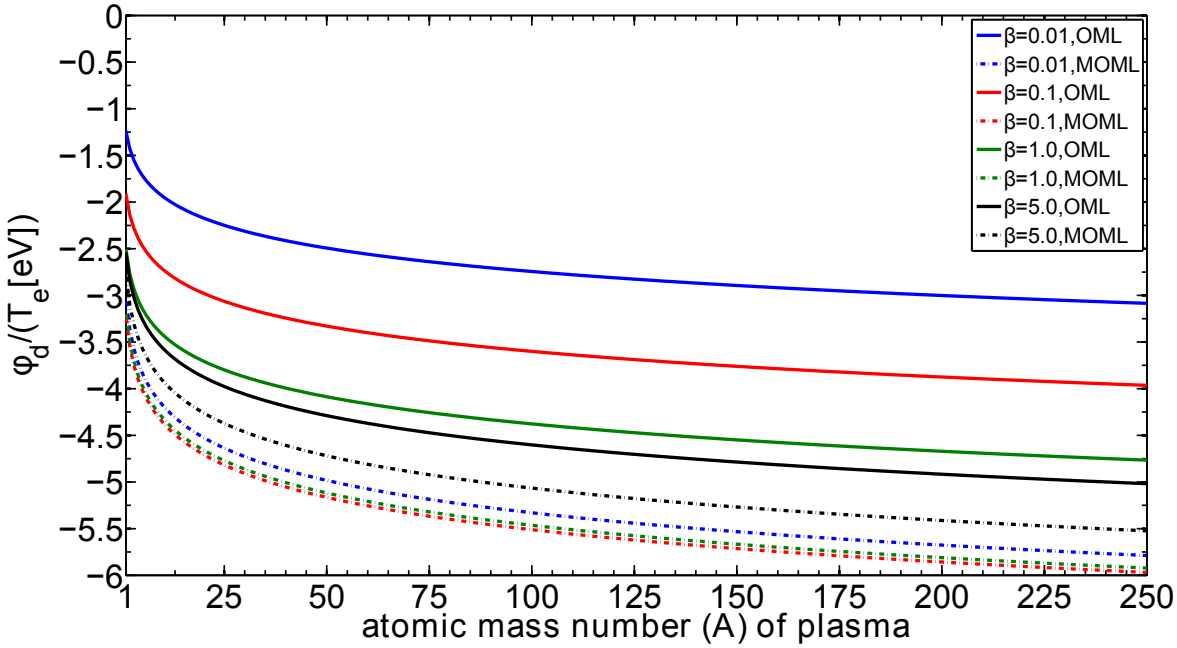


Figure 4.4: The plot between the ratio of ϕ_d and T_e (T_e in eV unit) and atomic mass number (A) by the OML (——) and MOML (-·-·-) charging model for $\beta = 0.01$, 0.1, 1.0, and 5.0.

$m_p = 1.67 \times 10^{-27}$ kg.

2. The conversion of mass to binding energy of the group of protons and neutrons to form a nucleus is negligible.

3. For a singly charged ion, the mass of a single electron is negligible compared to that of a single ion.

Based on the above approximations, the OML and MOML formulas for determining ϕ_d can be written in terms of atomic mass number (A). In other words, for simplicity, we can write

$$m_i \approx A \cdot m_p \,. \tag{4.3}$$

Additionally, not only A but also β, the ratio between ion (T_i) and electron (T_e) temperatures, and T_e control ϕ_d calculated by the OML and the MOML theories. We define a normalized potential, $\Phi_d = \phi_d/T_e[eV]$. Only β and A determine the magnitude of Φ_d. From this, the OML [38–40] and MOML [42] formulas can be written as shown in equation 4.4 and 4.5 below

$$\exp\left(\Phi_{d,OML}\right) = \sqrt{\frac{\beta m_e}{A m_p}}\left(1 - \frac{\Phi_{d,OML}}{\beta}\right) \tag{4.4}$$

$$\exp\left(\Phi_{d,MOML}\right) = \sqrt{\frac{\beta m_e}{A m_p}}\left(1 - \frac{\Phi_{d,MOML}}{\beta} + \frac{1}{2\beta}\ln\left(\frac{2\pi m_e}{A m_p}\left(1+\gamma\beta\right)\right)\right), \tag{4.5}$$

where γ is the ratio of specific heat capacity ($\gamma = 5/3$). We solve equation 4.4 and 4.5 iteratively, e.g. by the Newton method, because they are nonlinear. Their solution lines for these charging models are shown in figure 4.3 and 4.4.

Hydrogen (A=1), argon (A=40), and xenon (A=132) represent small and large plasma ion mass respectively. $\beta = 5.0$ is representative of a tokamak scrape-off layer (SOL) because it has been reported in ref. [71] (see figures 7 and 9 therein) that the ion temperature is larger than the electron temperature (i.e. $\beta > 1.0$ in the SOL). Figure 4.3 illustrates the trends of of $\phi_d/T_e[eV]$ for hydrogen, argon and xenon plasmas. As shown in the figure, the larger plasma ion mass, the more negative of Φ_d. In other words, at any T_e and β, $\phi_{d,OML}$ and $\phi_{d,MOML}$ is more negative compared to the potential of a farway plasma if plasma ion mass is larger. Therefore, in this figure, we can summarise that

$$\phi_{d,OML}(\text{xenon}) < \phi_{d,OML}(\text{argon}) < \phi_{d,OML}(\text{hydrogen}) \tag{4.6}$$

$$\phi_{d,MOML}(\text{xenon}) < \phi_{d,MOML}(\text{argon}) < \phi_{d,MOML}(\text{hydrogen}). \tag{4.7}$$

The $\beta\,(= T_i/T_e)$ values are varied from 0.001 to 1000.0. However, it is very rare to find $\beta >$ 10.0, except from a condition in a SOL plasma where it is possible to have $1.0 \leq \beta < 10.0$. Three regimes, $\beta \ll 1.0, \beta \approx 1.0$, and $\beta \gg 1.0$, are to be considered:

1. $\beta \ll 1.0$

    - In this regime, $\phi_{d,MOML}$ is always more negative than $\phi_{d,OML}$.
    - The ratio of $\phi_{d,MOML}/\phi_{d,OML}$ is larger when a heavier atomic mass number (A) plasma is used. In figure 4.3, in this case, $\phi_{d,MOML}/\phi_{d,OML}$ of hydrogen, argon and xenon are approximately 4.0, 2.8 and 2.67.

2. $\beta \approx 1.0$

    - In this regime, $\phi_{d,MOML}$ is still more negative than $\phi_{d,OML}$. However, the difference between both floating potentials is reduced compared to the case of $\beta \ll 1.0$.
    - The ratio of $\phi_{d,MOML}/\phi_{d,OML}$ is approximately close to the value of 1.25 for every plasmas. In figure 4.3, in this case, $\phi_{d,MOML}/\phi_{d,OML}$ of hydrogen, argon and xenon are approximately 1.3, 1.28 and 1.24.

3. $\beta \gg 1.0$

    - In this regime, the values of $\phi_{d,MOML}$ and $\phi_{d,OML}$ are close to each other. In orther words, they are approximately equal.
    - Because of $\phi_{d,MOML}/\phi_{d,OML} \rightarrow 1.0$, there is no need to change the charging model from OML to MOML in this regime; however, a plasma with $\beta \gg 1.0$ is very rare. Only SOL plasma can have $1.0 < \beta < 10.0$.

Moreover, The values of the floating potential slowly decrease with A for all β values, (excepted at low A, where the decrease is fairly drastic). This means that for the OML and MOML methods, A less influences on the values of the floating potential when A is large enough. Figure 4.4 shows that A significantly affects the $\phi_d/T_e[eV]$ of both charging models and every β values when A is approximately less than 40. This can be indicated by the sharp gradient of $\phi_d/T_e[eV]$.

These details of the floating potential trends for both OML and MOML provide a good overview for understanding the further results of a misty plasma in next sections,

Table 4.1: The values of surface tension (σ) of various droplet materials at given droplet temperatures (T_d)

Droplet materials	σ, N/m	T_d, K	References
tungsten (W)	2.5	3643	selected from table 61 in [72]
molybdenum (Mo)	2.25	2893	selected from table 33 in [72]
nickel (Ni)	1.76	1728	selected from table 35 in [72]
chromium (Cr)	1.63	2123	selected from table 11 in [72]
iron (Fe)	1.547	2500	using empirical formula in table 25 in [72]
beryllium (Be)	1.1	1773	selected from table 4 in [72]
boron (B)	1.06	2373	selected from table 6 in [72]
silicon (Si)	0.833	1683	selected from table 50 in [72]
lithium (Li)	0.318	1000	using empirical formula in table 28 in [72]
aluminium oxide (Al_2O_3)	0.69	2323	selected from table 1 in [73]
silicon oxide (SiO_2)	0.307	2073	selected from table 1 in [73]
water (H_2O)	0.06794	323	table on pages 6-182–6-185 in [74]
ethanol (C_2H_6O)	0.01989	323	table on pages 6-182–6-185 in [74]
n-hexane (C_6H_{14})	0.01533	323	table on pages 6-182–6-185 in [74]

in which three scenarios of selected well-known plasma systems are considered: a fusion plasma in a tokamak (section 4.3.1), a low pressure plasma (section 4.3.2) and a high pressure plasma (section 4.3.3).

4.3.1 Scenario 1: Fusion plasmas in tokamaks

Droplets can be introduced into a fusion plasma generally by two ways: splashing of liquid portion from molten layers on plasma facing materials, and melting of solid dust grains by plasma heating. In a tokamak, we can divide the plasma into two regions by considering magnetic field topology: a core and a scrape-off layer (SOL) plasma. The plasma in SOL is less energetic and more dilute than that in the core. In spite of this, the energy stored in both plasmas is still high enough to melt solid dust grains. In this scenario, we focus on metallic droplets. Moreover, we neglect electron emissions in this scenario. The droplet materials used in this scenario are tungsten (W), iron (Fe), beryllium (Be) and lithium (Li). These materials are well-known for building inner-tokamak tiles for specific purposes. The set-up parameters to determine minimum droplet radius ($r_{d,min}$) in this scenario is summarised and shown in tables 4.1 and 4.2. We assume quasineutral plasma, so ion (n_i) and electron (n_e) densities are equal. Figure 4.5 illustrates the trends of $r_{d,min}$ against T_e with the set-up parameters in tables 4.1 and 4.2.

First of all, the core plasma region and the SOL region should be roughly defined

Table 4.2: The set-up parameters of the fusion plasmas for scenario 1 in section 4.3.1

Droplet materials	W, Fe, Be and Li
Plasmas	singly charged deuterium (D^+)
Ratio of ion and electron tempertaures ($\beta = T_i/T_e$)	0.1, 1.0, 2.5 and 5.0
Electron temepratures (T_e)	1.0–10000.0 eV
Plasma number density ($n = n_i = n_e$)	$10^{18} - 10^{22}\,\mathrm{m}^{-3}$

in terms of T_e and n in order to consider the trends of $r_{d,min}$ against T_e clearly. The core plasma region is roughly in the range of $T_e > 100$ eV and $n > 10^{20}\,\mathrm{m}^{-3}$ and the SOL region is approximately in the range of $T_e < 100$ eV and $n < 10^{20}\,\mathrm{m}^{-3}$. Then, the behaviors of electrostatic breakup that is charaterised by the trends of $r_{d,min}$ and T_e are provided for the SOL and core regions.

1. SOL region ($T_e < 100$ eV and $n < 10^{20}\,\mathrm{m}^{-3}$)

   (a) Figure 4.5 clearly shows that the OML method is always a good approximation of ϕ_d and $r_{d,min}$ because $r_{d,min} \ll \lambda_D$, where λ_D is a Debye length which is controlled by electron temperature and number density, for all droplet materials.

   (b) Practically, it is possible to have a SOL plasma with $T_i > T_e$ and $1.0 < \beta < 10.0$. Therefore, $r_{d,min}$ by the OML and MOML are close to each other; however, the transition from the OML to the MOML method cannot be neglected. In spite of this, in a SOL plasma, which represents by the plasma with $\beta = 2.5$ and 5.0, $r_{d,min}$ by the OML is still less than λ_D, so the OML method still approximates ϕ_d well.

   (c) It is possible to imply that droplets in a plasma should be always stable if they can avoid electrostatic breakup while they are evaporating to the size of 10^{-9} m-scale. This is because the concept of atomic or molecular cluster should be introduced at this scale-size and the concept of material phase is unclear. If this assumption is used, the approximated T_e range of stable droplets for various meterial and β can be shown in table 4.3. The valus of $r_{d,min}$ and ϕ_d are not controlled by plasma number density (n), but n is used to determine the OML validity of charging through the use of a Debye length (λ_D).

   (d) Overall, $r_{d,min}$ by the OML method of all droplet materials are in the order of 10^{-9} - 10^{-7} m.

Droplet materials	T_e, eV	$\beta = T_i/T_e$
tungsten (W)	≤ 10.7	0.1
	≤ 10.2	1.0, 2.5 and 5.0
iron (Fe)	≤ 10.2	0.1
	≤ 9.5	1.0
	≤ 9.0	2.5 and 5.0
beryllium (Be)	≤ 10.0	0.1
	≤ 8.0	1.0, 2.5 and 5.0
lithium (Li)	≤ 6.0	0.1
	≤ 4.5	1.0
	≤ 4.0	2.5 and 5.0

Table 4.3: The approximated electron temperature (T_e) ranges for charged droplets are stable with the various ratio of ion and electron temperatures (β)

.

2. Core region ($T_e > 100$ eV and $n > 10^{20}\,\mathrm{m}^{-3}$)

   (a) In figure 4.5, $r_{d,min} < \lambda_D$ still appears at the edge of a core plasma, i.e. last closed magnetic surface (LCMS), where $T_e \approx$ a few hundreds eV and relative low plasma density compared to that of a core plasma. This means that the OML method is still a good approximation for ϕ_d as well as $r_{d,min}$ at the edge of a core plasma. However, the transition form OML to MOML methods is needed if droplets go deeper into the core plasma. This is because it appears that $r_{d,min} > \lambda_D$ deep in a core plasma where $T_e >$ a few hundred eV and very high plasma density. We need to evaluate ϕ_d by using the linear fitting formula for the transition region from the OML and MOML. Again, these trends are independent of dust grain material.

   (b) When the MOML method is used in a deep core plasma, it is found that $r_{d,min}$ for most metallic materials is of the order 10^{-7} - 10^{-3} m. Moreover, a lithium droplet can electrostatically break up at the size of an order of 10^{-2} m. This shows that electrostatic disintegration can occur at large size-scale, due to the high temperature which encourages a strong charging on the droplet.

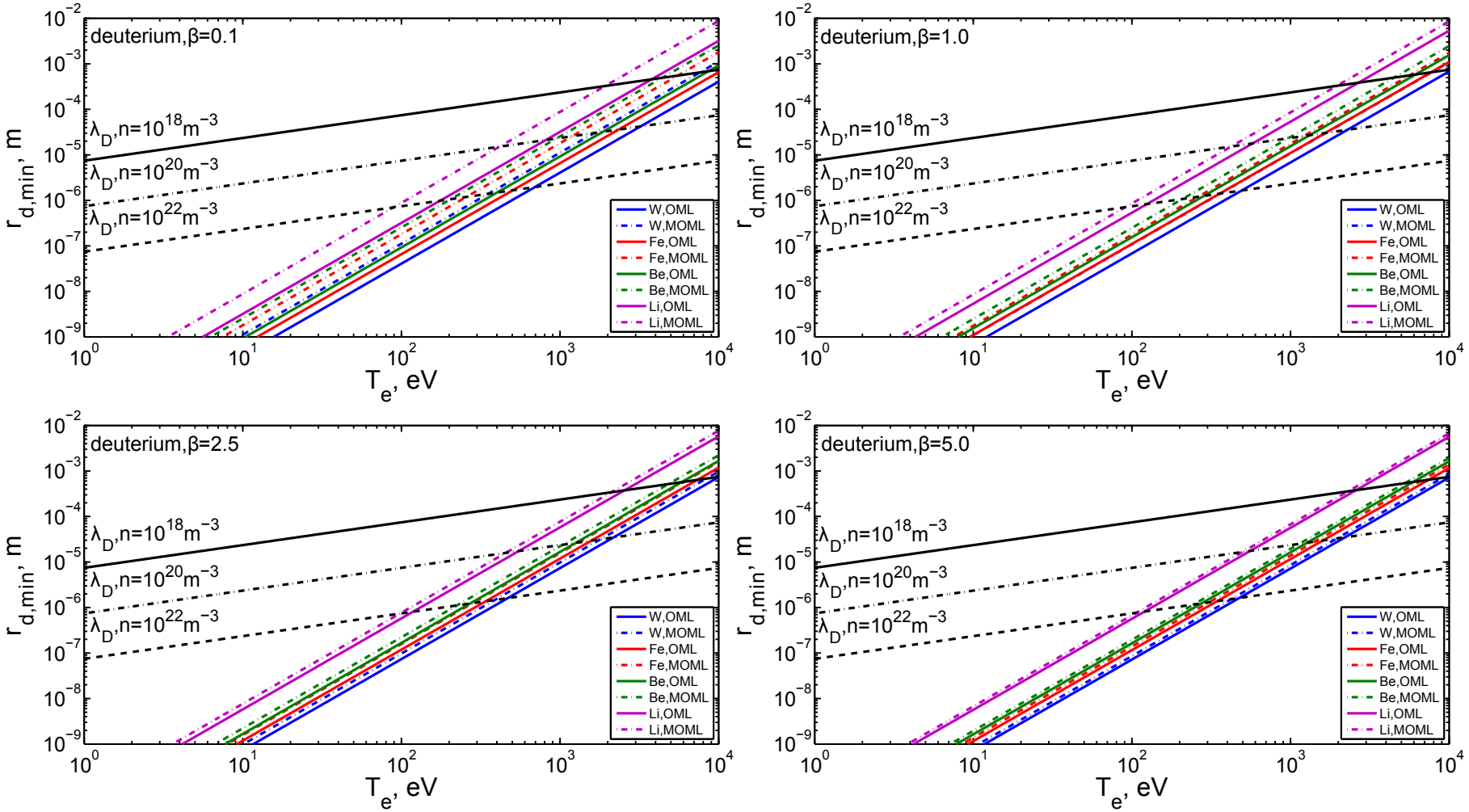


Figure 4.5: Plots of $r_{d,min}$ against T_e under the conditions of fusion plasmas in tokamaks (β = 0.1, 1.0, 2.5 and 5.0, deuterium (D) plasma, $n = 10^{18}, 10^{20}$, and $10^{22}\, m^{-3}$) for some well-known plasma facing materials: tungsten (W); iron (Fe); beryllium (Be); and lithium (Li) and the charging models: OML (——); and MOML (-·-·-) and also the plots of Debye lengths (λ_D), corresponding to $n = 10^{18}$ (——), 10^{20} (-·-·-), and 10^{22} (- - -) m^{-3} and T_e.

A lithium droplet is the easiest but a tungsten droplet is the most difficult to electrostatically disintegrate. This is because $\sigma_{Li} < \sigma_{Be} < \sigma_{Fe} < \sigma_W$, where σ_{Li}, σ_{Be}, σ_{Fe} and σ_W are the surface tensions of lithium, beryllium, iron, and tungsten. Hence, $r_{d,min,Li} > r_{d,min,Be} > r_{d,min,Fe} > r_{d,min,W}$, where $r_{d,min,Li}$, $r_{d,min,Be}$, $r_{d,min,Fe}$, and $r_{d,min,W}$ are the minimum radii of lithium, beryllium, iron, and tungsten droplets determined by the OML or the MOML methods.

4.3.2 Scenario 2: Low pressure plasmas

The plasmas in this case have low temperature and density and are also weakly ionised, where the ratio between ion and electron temperatures, β, is lower than 1.0. The charging on a droplet surface is expected to be weak and then the resulting small electrostatic force on a droplet surface implies that electrostatic breakup is unlikely to occur. Therefore, we have to consider a droplet, the material of which has low surface tension, in order to reduce the pressure due to surface tension, which is always inwards and help to stabilise the charged droplet. In other words, using a low surface tension material for a droplet should be easier for the droplet to disintegrate. The set-up parameters for this scenario can be seen in tables 4.1 and 4.4.

In general, various systems of low pressure plasmas have low temperature and density, the range of which are approximately in $T_e < 10$ eV, $\beta \ll 1.0$ and $n < 10^{16}\,\mathrm{m}^{-3}$. It is unavoidable to use a low surface tension material for a droplet to enhance electrostatic breakup because an electrostatic force on a droplet due to plasma charging is weak. In this scenario, we choose to use water (H_2O), ethanol (C_2H_6O) and n-hexane (C_6H_{14}), which

Droplet materials	water (H_2O)
	ethanol (C_2H_6O)
	n-hexane (C_6H_{14})
Plasmas	singly charged hydrogen (H^+)
	singly charged nitrogen (N^+)
	singly charged argon (Ar^+)
	singly charged xenon (Xe^+)
Ratio of ion and electron tempertaures ($\beta = T_i/T_e$)	0.01
Electron temepratures (T_e)	0.1–10000.0 eV
Plasma number density ($n = n_i = n_e$)	$10^{12} - 10^{16}\,\mathrm{m}^{-3}$

Table 4.4: The set-up parameters of the low pressure plasmas for scenario 2 in section 4.3.2

are the common liquids used in laboratory. They are lower in surface tension than metallic droplets.

The electrostatic breakup trends can be interpreted from the plots between $r_{d,min}$ and T_e in figure 4.6. The trends are

1. Plasma number density $n = 10^{12} - 10^{16}\,\mathrm{m}^{-3}$, electron temperature $T_e < 10$ eV and $\beta = 0.01$ are usual for low pressure plasmas. With these parameters, the OML method is a good approximation for determining a floating potential (ϕ_d) and then minimum radius of a charged droplet ($r_{d,min}$). It can be seen in figure 4.6 that $r_{d,min}$ (for $T_e < 10$ eV) $\ll$ Debye length (λ_D).

2. As we expected, the use of low surface tension materials for droplets can induce electrostatic breakup at lower T_e. This can be seen by comparison between the trends of $r_{d,min}$ and T_e illustrated in figure 4.6 with that of metallic droplets shown in figure 4.5 on the magnitude of $r_{d,min}$ at the same T_e.

3. The use of heavy-mass species for plasmas can increase $r_{d,min}$. This is because as shown in figure 4.3 and 4.4, the use of heavy plasma provides strong charging and this generates strong electrostatic force on a droplet surface. This means that electrostatic breakup is initiated easier and at lower T_e, as shown in figure 4.6.

Overall, in the range of $T_e \approx 1.0 - 10.0$ eV, it is possible to have electrostatic breakup with $r_{d,min} > 10^{-9}$ m; however, below this range, electrostatic breakup cannot happen. In other words, a charged droplet is stable because it has a size equal or lower than 10^{-9} m.

With regards to this study, the best condition to induce electrostatic breakup in laboratory is the use of heavy ion plasmas combined with the use of a low surface tension material for a droplet. Using nitrogen, argon and xenon for a plasma allows electrostatic breakup occur at $r_{d,min} \approx 10^{-7}$ m for ethanol and n-hexane droplets which have lower surface tension than water. In spite of this, it is noticeable that it is rare to have electrostatic breakup at $r_{d,min}$ of order 10^{-6} m although we use water, ethanol and n-hexane droplets, which are low in surface tension, and heavy plasmas, i.e. nitrogen, argon and xenon, instead of hydrogen. This suggests that to help electrostatic breakup occuring at the larger $r_{d,min}$, we need a droplet that has much lower surface tension than n-hexane, need to maximise input power to allow plasma accessing to high temperature and also heavier plasma, e.g.

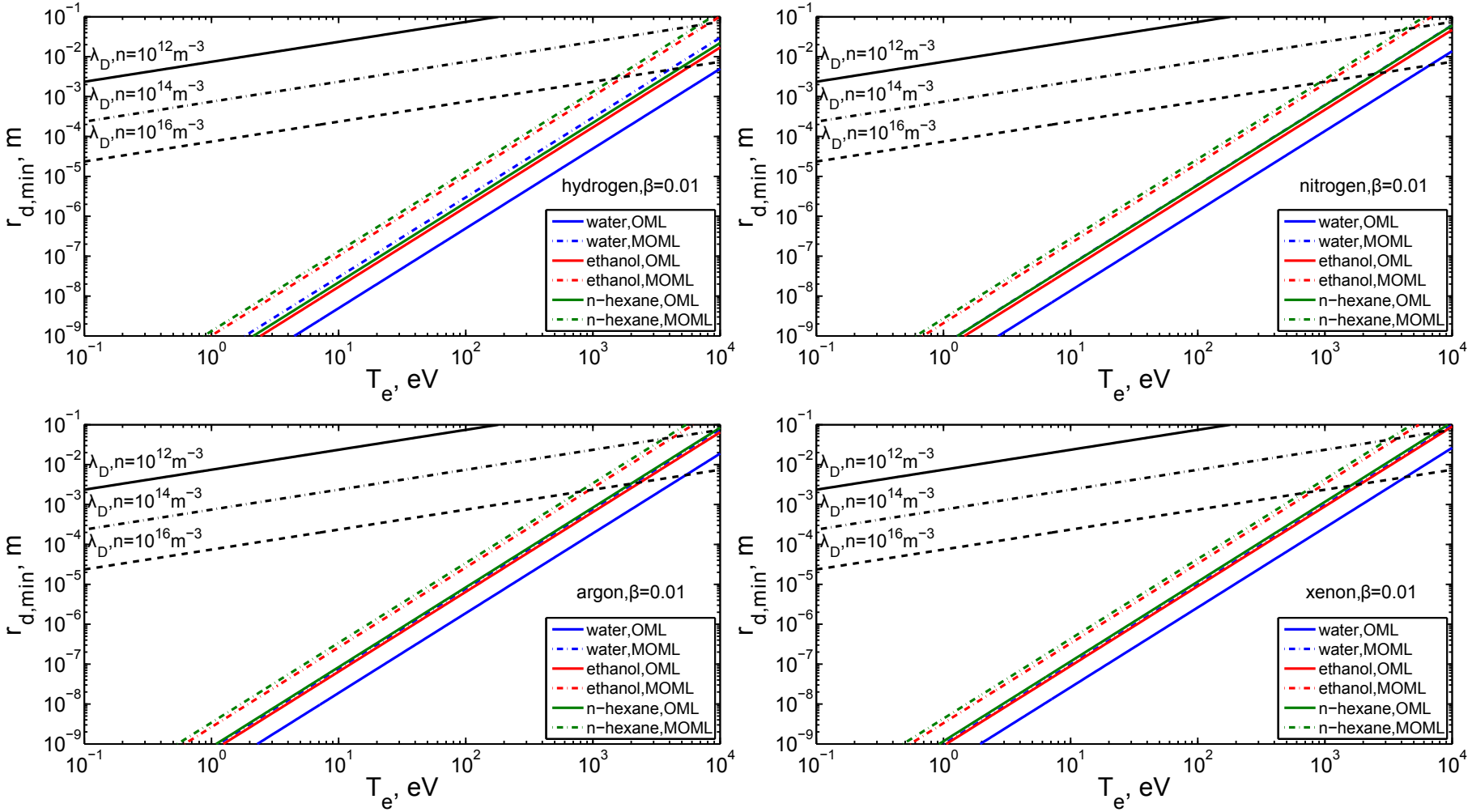


Figure 4.6: Plots of $r_{d,min}$ against T_e under the conditions of low temperature and density plasmas ($\beta = 0.01$, hydrogen (H), nitrogen (N), argon (Ar), and xenon (Xe) plasmas, $n = 10^{12}, 10^{14}$, and $10^{16}\, m^{-3}$) for some low surface-tension materials: water; ethanol; and n-hexane and the charging models: OML (——); and MOML (-·-·-) and also the plots of Debye lengths (λ_D), corresponding to $n = 10^{12}$ (——), 10^{14} (-·-·-), and 10^{16} (- - -) m^{-3} and T_e.

Table 4.5: The set-up parameters of the high pressure plasmas for scenario 3 in section 4.3.3 [76–78]

Droplet materials	Mo, Cr, Al_2O_3 and SiO_2
Plasmas	singly charged hydrogen (H^+) singly charged nitrogen (N^+) singly charged oxygen (O^+) singly charged argon (Ar^+)
Ratio of ion and electron tempertaures ($\beta = T_i/T_e$)	0.1
Electron temepratures (T_e)	0.1–10000.0 eV
Plasma number density ($n = n_i = n_e$)	$10^{23} - 10^{25}\,\mathrm{m}^{-3}$

mercury. However, it has to be noted that the change in floating potential (ϕ_d) by plasma charging, which occurs if atomic mass number (A) is larger than 40 is very slight, (see figure 4.4). This implies that using heavier plasma than xenon may not cause significant improvement.

4.3.3 Scenario 3: High pressure plasmas

Plasma spraying [75] can be exemplified as a high pressure plasma system. It is one of the coating techniques to enhance material properties and endurance of coated surfaces and it is well-known for coating on metallic surfaces. It uses a plasma torch which carries coating powders towards the target surface in a plasma jet. On the way to the surface, the plasma is energetic enough to melt the material powders to be droplets before they coat on the surface. Therefore, a plasma spraying system contains a misty plasma. Its plasma number density can be in $10^{22} - 10^{25}\mathrm{m}^{-3}$, but its electron temperature is usually lower than 10 eV [76].

In this study, we are interested in molybdenum (Mo), chromium (Cr), aluminium oxide (Al_2O_3) and silicon oxide (SiO_2), which are common coating materials, droplets in hydrogen (H), nitrogen (N), oxygen (O) and argon (Ar) plasmas, which are in general used in plasma torch [77]. Table 4.1 shows their surface tensions (σ). Electron temperature is varied from 0.1–10000.0 eV. However, ref. [76, 78] show that ion temperature is lower than electron temeperature by approximately an order of magnitude. Therefore, in this case, we assume that the ratio of ion and electron temperatures (β) = 0.1.

Figure 4.7 shows the trends of $r_{d,min}$ and T_e of various droplets and plasmas. The trends can be summarised as

1. In the case of plasma spraying where $T_e < 10$ eV, the OML method is a good approximation to determine floating potential (ϕ_d) and then $r_{d,min}$ if the plasma number density is lower than an order of $10^{25}\,\mathrm{m}^{-3}$. However, the MOML method and the formula for the intermediate floating potential regime between the OML and MOML methods should be adopted instead if the plasma number density is in an order of $10^{25}\,\mathrm{m}^{-3}$ or more. This is because $r_{d,min} \geq \lambda_D$ approximately, so the OML method is not a good approximation for determining floating potential (ϕ_d) and then $r_{d,min}$. This implies that for plasma systems, which have higher number density than plasma spraying system, e.g. wire array Z-pinch plasmas, the use of MOML cannot be avoided.

2. With the temperature range of plasma spraying, $T_e < 10$ eV, molybdenum (Mo) and chromium (Cr) droplets are stable to the size of an order of 10^{-9} m especially if the light plasmas, i.e. hydrogen, nitrogen and oxygen, are used. This suggests that it is possible to have nano-size metallic droplets to be coated on a surface without undergoing electrostatic breakup on the way towards the surface. However, the stabilities of Al_2O_3 and SiO_3 droplets is reduced and can be only stable to the size of an order of 10^{-9} m at approximately a few eV compared to that in the case of the metallic droplets. In other words, the heavier plasmas, the lower T_e for the nano-scale droplets to survive. This is because of lower surface tension of Al_2O_3 and SiO_2 droplets. To keep the qualities of nano-size Al_2O_3 and SiO_2 droplets from electrostatic breakups before they reach the surface, plasma torch power should be set up to be low, i.e. a few eV. For droplet material considered here, droplets, which are larger than an order of nanometres can avoid electrostatic breakup in plasma torch with the usual conditions, i.e. $n = 10^{22} - 10^{25}\mathrm{m}^{-3}$ and $T_e < 10$ eV.

3. From the point of view of electrostatic breakup, a low A plasma should be used to spray nanoparticle droplets by plasma torch, because it helps in stabilising electrostatic breakup. As can be seen in the case of hydrogen plasma in figure 4.7, most nanoparticle droplets start to breakup at $T_e \geq 10.0$ eV. The stability of nanoparticle spraying is slightly reduced with the heavier plasmas, as can be seen in the case of nitrogen, oxygen and argon plasmas, are used.

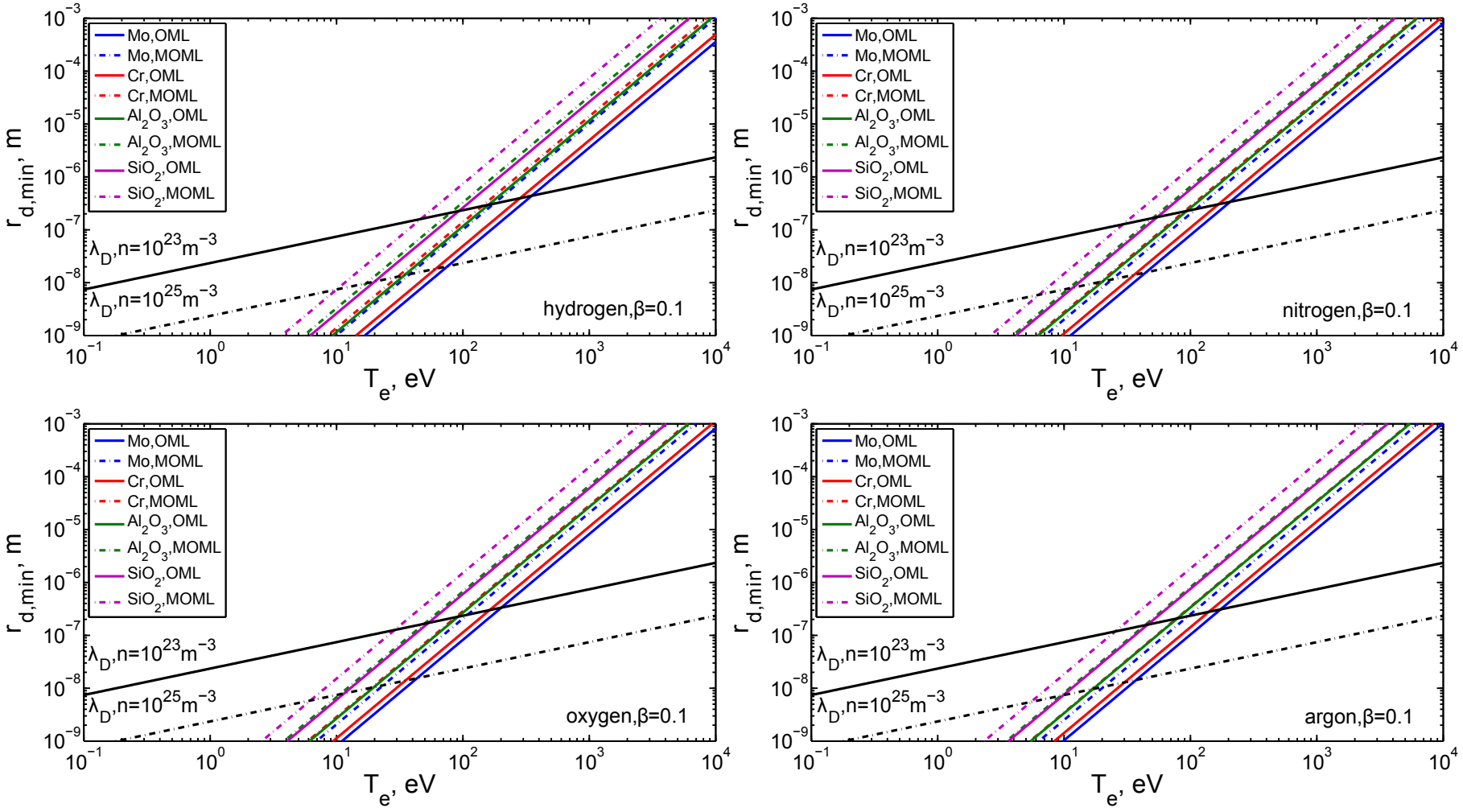


Figure 4.7: Plots of $r_{d,min}$ against T_e under the conditions of a high pressure plasma represented by plasma spraying, ($\beta = 0.1$, hydrogen (H), nitrogen (N), oxygen (O), and argon (Ar) plasmas, $n = 10^{23}$, and $10^{25}\, m^{-3}$) for some coating materials: molybdenum (Mo); chromium (Cr); aluminium oxide (Al_2O_3); and silicon oxide (SiO_2) and the charging models: OML (——); and MOML (-·-·-) and also the plots of Debye lengths (λ_D), corresponding to $n = 10^{23}$ (——), and 10^{25} (- - -) m^{-3} and T_e.

Table 4.6: Summary the appropriate use of charging models in various scenarios

Type of plasmas	charging models
Core plasma	MOML
Last closed magnetic surface (LCMS)	OML
Scrape-off layer (SOL)	OML
Low density and pressure plasmas	OML
Plasma spraying at relatively low density ($n < 10^{25}\,\mathrm{m}^{-3}$)	OML
Plasma spraying at relatively high density ($n \geq 10^{25}\,\mathrm{m}^{-3}$)	MOML

With the usual plasma parameters of plasma spraying, the droplets are stable with the size smaller than 10^{-9} m. However, the droplets become unstable at the electron temperatures of a few eV if low surface tension droplets and heavy plasmas are used. Although, the droplets can breakup at the radius larger than 10^{-9} m, $r_{d,min} \leq 10^{-8}$ m approximately.

4.4 Discussions and conclusions

In section 4.3.1, we conducted some case studies for each type of plasmas: a fusion plasma; low temperature and density plasma; and high pressure plasma, in order to show the trends of $r_{d,min}$ against some parameters, i.e. electron temperature (T_e), the ratio of ion and electron temperatures (β), plasma number density (n), surface tension of various droplet materials (σ) and atomic mass number of various plasma species (A). In this section, we would like to illustrate the expectation of the behaviors of electrostatic breakup in each plasma systems. Table 4.6 summarizes which charging model is used in the corresponding plasma systems. For the case of fusion plasmas in tokamaks shown in scenario 1 in section 4.3.1, the OML method is a good approximation of floating potential (ϕ_d) for the region of scrape-off layer (SOL) and last closed magnetic surface (LCMS), but the MOML method is good for determining ϕ_d in a core plasma.

Figure 4.5 in section 4.3.1 clearly shows that droplets in fusion plasmas are limited on the possible sizes due to the influence caused by electrostatic breakup. Furthermore, the electrostatic breakup process is much faster than the droplet evaporation process [54]. Using this concept helps us to qualitatively predict the additional behaviors of the tokamak dust impurity deposition, which may possibly be observed by camera, and the observations of metallic dust which has survived. In fact, in fusion plasmas, electrostatic breakup influences

metallic dust mainly in 3 ways:

1. Enhancement of dust destruction

   Dust destruction is enhanced. In fact, electrostatic breakup enhances ordinary evaporation. If $r_d > r_{d,min}$, droplets are electrostatically stable. A reduction of the sizes of droplets results from ordinary evaporation. However, when $r_d \leq r_{d,min}$, strong outwards electrostatic force completely breaks a droplet up and then generates many secondary very fine droplets ejecting from the Taylor's cones of the droplet continuously and rapidly. This process is too fast for a droplet to be restabilised by moving to the plasma where the surface electrostatic force is lower. A large amount of secondary droplets gives a significantly large total surface area. This leads to an increase in evaporation rate. In other words, overall, strong evaporation should happen when electrostatic breakup occurs because it increases evaporation rate by plasma heating through the fact that a droplet surface area increases.

2. Dust size cut-off

   Due to the fact that metal can melt in a fusion plasma, droplets can be mixed in the plasma. Metallic dust become molten droplets. The evidence of this is the spherical shape of metallic dust collected after several operations [5]. The spherical shape results from surface tension of liquid and this indicates the existence of misty plasmas in tokamaks. However, the dust collection and characterisation in the dust experiment conducted in the full tungsten ASDEX Upgrade [5] have shown that flakes occur in larger quantities than spherical dust grains. This suggests that the metallic spherical dust grains survive from electrostatic breakup and their size is always larger the minimum droplet size until the termination of tokamaks. The dust experiment [5] also show that the sizes of the observed spherical dust is usually in an order of micrometres and their average size is around a few microns. However, the amount of metallic spherical dust which has a size smaller than 1 μm is lower than that of non-spherical flakes (adding after the PhD viva). Based on electrostatic breakup, $r_{d,min}$ is the minimum size of metallic dust. This minimises the number of spherical dust and their size. If we look in the opposite way, we may use $r_{d,min}$ to estimate the limitation of metallic dust transport by using $r_{d,min}$ to trace back the final positions of discovered dust and then identifying the area covering most dust transport. This may help to

find the plasma setup to reduce the tokamak dust impurity deposition at the desired region and eventually to suppress dust transport into a core plasma. This may also be applied to finding a suitable plasma setup for wall-conditioning by metallic dust grains, e.g. Li dust.

3. Possibility to find nano-scale metallic dust

   In figure 4.5, it is clearly seen that charged droplets with various types of materials are stable towards the size of nm when the electron temperature is lower 10 eV approximately, the temperature of which is usually observed in a SOL plasma near plasma facing surfaces. Therefore, this implies that it is possible to find metallic nano-scale dust grains near plasma facing surfaces if the dust grains can avoid evaporation and electrostatic breakup deep in a fusion plasma. This also implies that it is possible to find the metallic nano-scale dust grains formed by the accumulation of saturated impurity vapour near plasma facing surfaces.

With regards to the case of low pressure plasmas in section 4.3.2, we can summarise that it is difficult to induce electrostatic breakup in this plasma system. In laboratory, plasma can only be discharged with low energy due to the limitation of input power supplies. This results in the weak plasma charging on a droplet which is associated with a weak outward surface electrostatic force. To compensate this and promote electrostatic breakup, we need very low surface tension droplet to reduce inward force that opposes electrostatic force and heavy plasma to increase charging on a droplet. However, it is rare to have electrostatic breakup occuring at $r_{d,min}$ of an order of 10^{-6} m. This means that even though we can induce electrostatic breakup in laboratory plasma, it may be difficult to observe it solely by camera. This implies that more complicated techniques for observing electrostatic breakup in plasma is required. Furthermore, it may be hard to find very low surface tension material for a droplet to allow it to breakup electrostatically at the size of a few micron or larger.

With regards to the case of plasma spraying in section 4.3.3, it is difficult to have electrostatic breakup at the large droplet size which is of an order of micron or larger. The droplets are mostly stable at a few eV. Metallic droplets are more stable because they have higher surface tension and require higher electron temperature to breakup. The study of a misty plasma helps to identify suitable plasma parameters for using plasma spraying to

coat nanoparticle powder without degrading droplets on the way to the surface. In addition, plasma spraying is an example of high pressure plasma systems. If droplets are in wire-array Z pinch plasmas which generally have the same order of plasma number density but electron temperature can be a few tens of eV, they may electrostatically breakup at a size larger than that in plasma spraying with the help of the wire produced plasmas which is normally metallic atom and heavy. In this case, the MOML is needed to determine floating potential ϕ_d and $r_{d,min}$.

Chapter 5

PRESSURE ON A LARGE DROPLET IN A PLASMA

We have seen in chapter 3 that external pressure does not affect electrostatic breakup of a liquid droplet, because the liquid is incompressible. However, it does affect the equilibrium state of the droplet. In this chapter, we consider the effect of the external pressure from the plasma in the equilibrium droplet liquid pressure. Section 5.1 reviews the way to determine various pressures, especially ion and electron pressures, on a large droplet surrounded by a plasma. Section 5.2 shows the way to calculate the liquid pressure on the droplet by the modified Laplace equation (MLE) [79]. Sections 5.3 and 5.4 show and discuss about preliminary results concerning the size-evolution on liquid pressure evaluated by the OML [38–40] and MOML [42] approaches.

5.1 Derivation of pressures on a large droplet in a plasma

In section 3.2.2, we saw on how to calculate a pressure due to surface tension, an electrostatic pressure, ion and electron pressures and a pressure due to neutral recombination for a small droplet in a plasma. In this section, we focus on how to determine those pressures on a large droplet in a plasma, in which the droplet radius is larger than the Debye length, $r_d > \lambda_D$ and the thin sheath is developed. In this case, the OML approach [38–40] cannot be applied.

It is clear that even though we consider a large spherical droplet in a plasma,

the formula to calculate the pressure due to surface tension (P_{st}) (see eq. 3.166) and the electrostatic pressure (P_{es}) (see eq. 3.169) are still valid without the droplet size restriction. The floating potential used in the latter can be conveniently determined by the floating potential formula by the MOML theory [42], i.e. $\phi_{d,MOML}$ in eq. 4.2. The pressure due to neutral recombination (P_r) (see eq. 3.247) can be still used too but the electron current (see eq. 3.241) or the ion current required to calculate the radial particle flux (Γ_r) are calculated from the MOML theory, i.e. we also use $\phi_{d,MOML}$ (see eq. 4.2) instead of that by the OML theory (see eq. 1.1) [38–40]. The main problem is the determination of ion and electron pressures with the presence of the thin sheath around the large droplet.

In a plasma, with regard to a small droplet, there is no concept of a sheath applied to it. In contrast, a thin sheath is developed around a large droplet. With the effect of the pre-sheath, the ions are accelerated to reach the Bohm speed before entering the sheath edge [42]. Moreover, the local ion acceleration by the sheath around the large droplet increase the ions' speed exceeding the Bohm speed on the way to the droplet surface. This affects the magnitudes of the ion momentum flux onto the droplet. The modification of ion current by the thin sheath can be determined by the MOML theory [42]. The concept of the theory is simple because it uses the assumption that the droplet is large enough so that each part of the droplet surface is approximated as a planar surface. Its thin sheath can be adopted a planar wall sheath configuration. The MOML theory (see eq. 4.2) is convenient for evaluating the floating potential without the requirement of knowing the ion-sheath characteristics. In addition, the electron current still obeys the Boltzmann law; however its magnitude deviates from that from the OML theory by the modification of the sheath effect through the ion current in the steady state, $I_e = I_i$. At the steady state, the floating potential sets up and its value is obtained from the steady state charge equation can be seen in eq. 4.2 in section 4.2. Unfortunately, to determine the ion pressure inside the sheath is not a simple task because the ion-sheath characteristics are required, e.g. the ion distribution function at the sheath edge and the droplet surface, to accurately calculate the addition ion pressure gained during the acceleration in the sheath. The ion-sheath characteristics required for accurately evaluating the ion pressure is diffcult to be determined, while electron pressure is rather simpler because electrons always obey the Boltmann's law. As a result, we need to indirectly calculate the ion pressure through the

conservation of the plasma particle momentum fluxes, stress, using an approach suggested by [80]. We first define Γ_i as the total ion pressure (i.e. momemtum flux), determining by

$$\Gamma_i = \int\int\int m_i f_i \mathbf{v_i} \mathbf{v_i} \, d^3v. \tag{5.1}$$

Because ions moves in the sheath and have non-zero drift velocity, this is not just the ion thermal pressure (P_i) but

$$\Gamma_i = P_i + \rho_i \mathbf{u_i} \mathbf{u_i}, \tag{5.2}$$

where $\mathbf{u_i}$ is an ion drift velocity. The two components on the RHS of eq. 5.2 are a thermal pressure; and a dynamic pressure, on the droplet. The ion thermal pressure originates from the random motion and the ion dynamic pressure originates from the drift velocity developed after ions enter the sheath edge. Using the steady state 1-D ion and electron fluid equations of motion (in x direction),

$$\rho_i u_{i,x} \frac{\partial u_{i,x}}{\partial x} = -\frac{\partial P_{i,xx}}{\partial x} + n_i e E_x \tag{5.3}$$

$$-\frac{\partial P_{e,xx}}{\partial x} - n_e e E_x = 0, \tag{5.4}$$

with the 1-D Gauss' law,

$$\frac{\partial E_x}{\partial x} = \frac{(n_i - n_e)e}{\epsilon_0}, \tag{5.5}$$

Rearranging eq. 5.3, 5.4 and 5.5, so

$$\frac{d}{dx}\left(\Gamma_i + P_e - \frac{\varepsilon_0 E^2}{2}\right) = 0 \tag{5.6}$$

$$\Gamma_i + P_e - \frac{\varepsilon_0 E^2}{2} = \text{constant}, \tag{5.7}$$

where Γ_i is the net ion pressure, which has the two components. The term P_e is the electron pressure, which corresponds to the non-drifting Maxwellian distribution everywhere, on the droplet. The term $\frac{\varepsilon_0 E^2}{2}$ is an electrostatic pressure on the droplet. We consider two positions: at the sheath edge (subscripting with se); and at the droplet surface (subscripting

with d). By the use of eq. 5.7, we can write the relationship between the sheath edge and the droplet surface as

$$\left(\Gamma_i + P_e - \frac{\varepsilon_0 E^2}{2}\right)_{se} = \left(\Gamma_i + P_e - \frac{\varepsilon_0 E^2}{2}\right)_d . \tag{5.8}$$

At the sheath edge, we neglect the electric field because it is very small, $E_{se} \to 0$, while a strong electric field is developed in the sheath. Moreover, the OML approach for determining the ion momentum flux, the ion pressure, is approximately valid upto the sheath edge, which corresponds to the assumption used in the MOML theory [42]. Hence, the LHS of eq. 5.8 can be determined by the OML ion and electron pressures shown in eq. 3.208 and 3.240 in section 3.2.2 but the potential is of the sheath edge, ϕ_{se}, found by the use of the MOML theory (see eq. 4.2) combined with the assumption of the planar sheath mentioned in ref. [42] (see section 4.2), rather than the floating potential,

$$\phi_{se} = \phi_{d,MOML} - \frac{T_e[eV]}{2} \ln\left(2\pi \frac{m_e}{m_i}(1+\gamma\beta)\right). \tag{5.9}$$

By substituting eq. 5.9 into eq. 3.208 and 3.240, we can determine ion and electron momentum fluxes or pressures at the sheath edge. At RHS of eq. 5.8, we can find the electrostatic pressure by the use of eq. 3.169 shown in section 3.2.2 combined with $\phi_{d,MOML}$, so

$$\left(\frac{\varepsilon_0 E^2}{2}\right)_d = \frac{\varepsilon_0 \phi_{d,MOML}^2}{2 r_d^2}, \tag{5.10}$$

where r_d is the droplet radius. Hence, we can find the sum of ion and electron pressures on the large droplet by eq. 5.8,

$$(\Gamma_i + P_e)_{d,MOML} = \Gamma_{i,se} + P_{e,se} + \frac{\varepsilon_0 \phi_{d,MOML}^2}{2 r_d^2}, \tag{5.11}$$

where the expressions of $\Gamma_{i,se}$ and $P_{e,se}$ are referred to eq. 3.208 and 3.240, so the ion and

elctron pressures at the sheath edge are

$$\Gamma_{i,se} = \frac{1}{2} n_{i,0} k T_i \left(2 \left(\frac{2}{3} \hat{\Phi}_{se} + 1 \right) \sqrt{\frac{\hat{\Phi}_{se}}{\pi}} + \exp\left(\hat{\Phi}_{se} \right) \operatorname{erfc}\left(\sqrt{\hat{\Phi}_{se}} \right) \right) \tag{5.12}$$

$$P_{e,se} = \frac{1}{2} n_{e,0} k T_e \exp\left(-\Phi_{se} \right), \tag{5.13}$$

where $\Phi_{se} = -\frac{e\phi_{se}}{kT_e}$ and $\hat{\Phi}_{se} = -\frac{e\phi_{se}}{kT_i}$ and the potential at the sheath edge (ϕ_{se}) can be seen in eq. 5.9.

5.2 Modified Laplace Equation (MLE)

The Laplace equation is defined as a hydrostatic pressure balance equation. The original Laplace equation is basically

$$P_{inwards} = P_{outwards}, \tag{5.14}$$

where $P_{inwards}$ and $P_{outwards}$ are total inwards and outwards pressures, respectively. We categorize a pressure due to surface tension (P_{st}), an ion pressure (Γ_i), an electron pressure (P_e) and a neutral recombination pressure (P_r) as inwards pressures. In contrast, we categorize an electrostatic pressure (P_{es}) and a resultant liquid pressure (P_{liq}) as outwards pressures. From this, we can write the modified Laplace equation (MLE) [79] by substituting the pressures mentioned above into the original Laplace equation, eq. 5.14, as

$$P_{st} + \Gamma_i + P_e + P_r = P_{es} + P_{liq}. \tag{5.15}$$

To find the resultant liquid pressure (P_{liq}), the MLE, shown in eq. 5.15, need to be rearranged and then

$$P_{liq} = P_{st} + \Gamma_i + P_e + P_r - P_{es}. \tag{5.16}$$

The pressure due to surface tension and the electrostatic pressure depend on the droplet size, i.e. $P_{st} \propto \frac{1}{r_d}$ and $P_{es} \propto \frac{1}{r_d^2}$ but the ion and electron pressures and the pressure due to neutral recombination do not depend on the droplet size. We substitute eq. 3.166 for the

pressure due to surface tension and eq. 3.169 for the electrostatic pressure into the MLE (see eq. 5.16), so the liquid pressure is

$$P_{liq} = \Gamma_i + P_e + P_r + \frac{2\sigma}{r_d} - \frac{\varepsilon_0 \phi_d^2}{2r_d^2}. \tag{5.17}$$

We can also define an external pressure (P_{ext}) as $P_{ext} = \Gamma_i + P_e + P_r$.

5.3 Results and discussions

We consider the variation of liquid pressure as a droplet evaporates and r_d falls. We assume that the droplet starts to evaporate from $r_d = 10^{-3}$ m^{-3}. We compare the liquid pressures for the small droplet ($P_{liq,S}$) determined by the net pressures indicated by the OML theory [38–40] (see section 3.2.2) and the large droplet ($P_{liq,L}$) by the MOML theory [42] (see section 5.1). We find that the pressure due to recombination (P_r) is very small compared to other pressures, so we neglect it in this section. We also use eq. 5.17 for finding the liquid pressure on the droplet of both cases, so

$$P_{liq,S}(r_d) = \Gamma_{i,d,OML} + P_{e,d,OML} + \frac{2\sigma}{r_d} - \frac{\varepsilon_0 \phi_{d,OML}^2}{2r_d^2} \tag{5.18}$$

$$P_{liq,L}(r_d) = (\Gamma_i + P_e)_{d,MOML} + \frac{2\sigma}{r_d} - \frac{\varepsilon_0 \phi_{d,MOML}^2}{2r_d^2} \tag{5.19}$$

$$= \Gamma_{i,se} + P_{e,se} + \frac{2\sigma}{r_d}. \tag{5.20}$$

where $\Gamma_{i,d,OML}$, $P_{e,d,OML}$ and $\frac{\varepsilon_0 \phi_{d,OML}^2}{2r_d^2}$ are the ion, electron and electrostatic pressures on the small droplet, discussed in section 3.2.2, with the use of the OML floating potential, $\phi_{d,OML}$. $(\Gamma_i + P_e)_{d,MOML}$ and $\frac{\varepsilon_0 \phi_{d,MOML}^2}{2r_d^2}$ are the sum of ion and electron pressures and the electrostatic pressure on the large droplet and $\Gamma_{i,se}$ and $P_{e,se}$ are the ion and electron momemtum fluxes or pressures at the sheath edge derived in section 5.1 with the use of

Table 5.1: The set-up parameters of the works shown in figures 5.1-5.3

Droplet materials	W, Be, Li, and n-hexane (C_6H_{14})
Plasma	singly charged hydrogen (H^+)
Ratio of ion and electron tempertaures ($\beta = T_i/T_e$)	1.0
Electron temepratures (T_e)	1.0, 10.0, 100.0 and 1000.0 eV
Plasma number density ($n_i = n_e = n$)	10^{16}, 10^{20}, and 10^{24} m^{-3}

the MOML idea and the conservation of momemtum flux. The surface tension term, $\frac{2\sigma}{r_d}$, is valid for both small and large droplets. The transition of the pressure model for small to large droplet occurs at $r_d \to \lambda_D$. It is interesting to note that for a large droplet, the electrostatic term ($\propto \phi_d^2$) cancels from the equilibrium condition (see eq. 5.20), but still plays a crucial role in determining electrostatic stability (see chapter 4). The study of the liquid droplet on different droplets in various plasma set-ups can be summarised in table 5.1, which are also used to produce figures 5.1-5.3. We also note that figures 5.1, 5.2 and 5.3 represent low, medium and dense plasmas, respectively. In addition, we find that Γ_i is always much larger than P_e.

For the low density plasma shown in figure 5.1, P_{ext} is not significant because Γ_i is very small. Even though T_e is high but n is too low, it is not effective to enhance P_{ext}. From this, $P_{liq} \approx \frac{2\sigma}{r_d} - \frac{\varepsilon_0 \phi_d^2}{2r_d^2}$. For $r_d \gg r_{d,min}$, the pressure due to surface tension term ($\frac{2\sigma}{r_d}$) dominates but For $r_d \to r_{d,min}$, the electrostatic pressure term ($\frac{\varepsilon_0 \phi_d^2}{2r_d^2}$) dominates and tends to take over P_{st}. In general, we use the OML $P_{liq,S}$ for $r_d < \lambda_D$ but change to use the MOML $P_{liq,L}$ for $r_d > \lambda_D$. As can be seen from figure 5.1, the OML $P_{liq,S}$ can be applied to determine P_{liq} without the model transition.

For the medium and high density plasmas in figures 5.2 and 5.3, we start to see the contribution of P_{ext} to P_{liq}. With regard to $n = 10^{20}$ m^{-3} shown in figure 5.2, for $T_e < 100$ eV and only for the low surface tension droplet, i.e. n-hexane, with $r_d > 10^{-5}$ m, P_{ext} deviates P_{liq} from the effect of P_{st}. To extend this trend to metal droplets, i.e. W, Be and Li, we require $T_e > 100eV$. The difference between the OML $P_{liq,S}$ and the MOML $P_{liq,L}$ is clearly seen for $T_e = 1000$ eV. At that point, all types of droplets are not dominated by only P_{st} but by $P_{st} + P_{ext}$. This flattens P_{liq}. Moreover, the MOML $P_{liq,L}$ is lower than the OML $P_{liq,S}$ for large r_d, so at that range, the latter overestimates the first. However, at $r_d \to \lambda_D$, the MOML $P_{liq,L}$ is higher than the OML $P_{liq,S}$, so the latter underestimates the first. If the droplet tends to breakup near $r_d \to \lambda_D$, it can access higher P_{liq}, for example, the beryllium droplet in the plasma with $n = 10^{20}$ m^{-3} and $T_e = 1000$ eV in figure 5.2. Therefore, the transition of the liquid pressure model is required. The above trends can be applied to the case of $n = 10^{24}$ m^{-3} (dense plasma) shown in figure 5.3 for all T_e and droplet materials. In addition, the case of $T_e > 100$ eV becomes the extreme case.

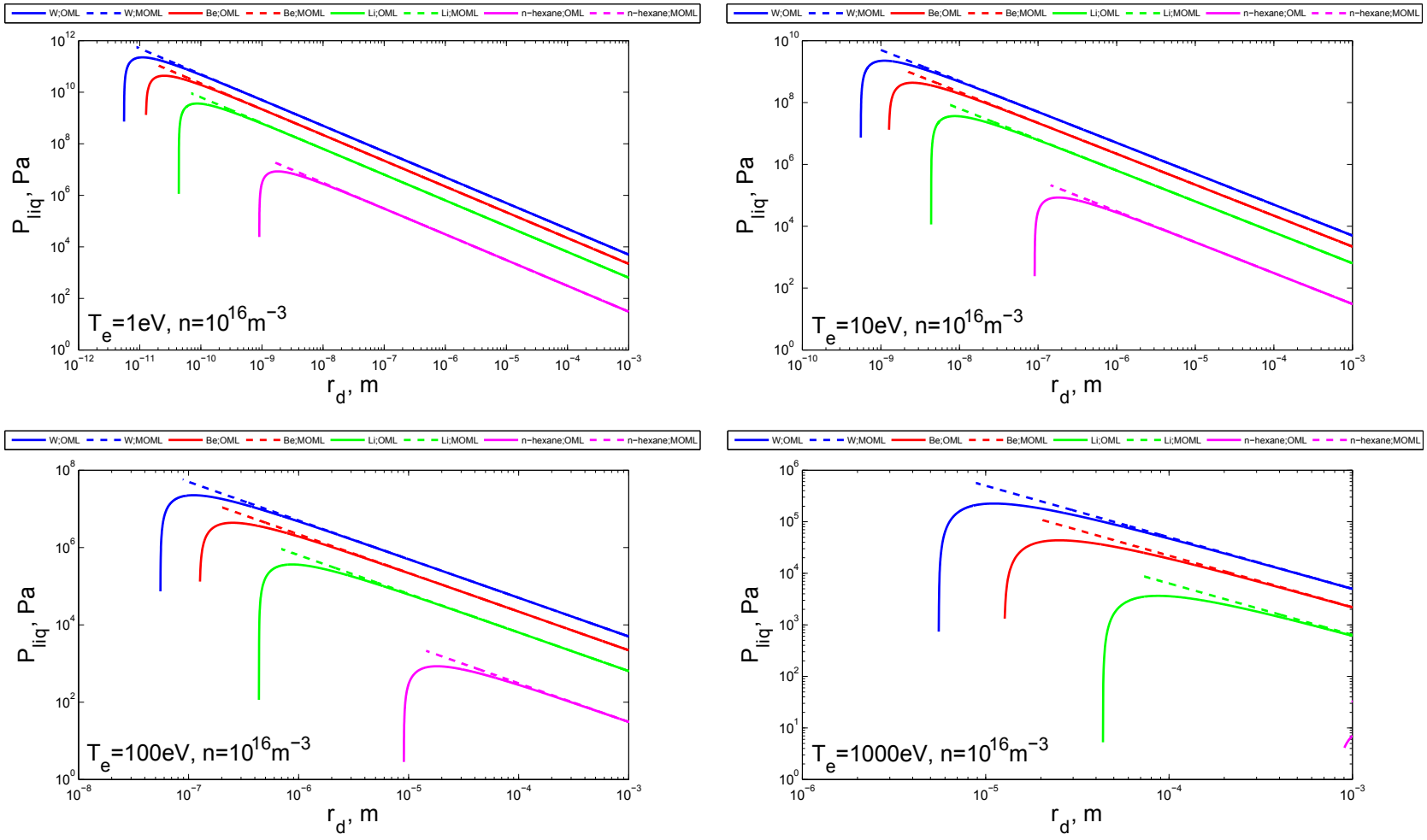


Figure 5.1: The figure shows the trends of liquid pressures when the droplets allow evaporation, where the tungsten (W), beryllium (Be), lithium and n-hexane droplets are in the plasma of $n = 10^{16}$ m^{-3} and $T_e = 1 - 1000$ eV. The solid lines correspond to OML. The dashed lines correspond to MOML.

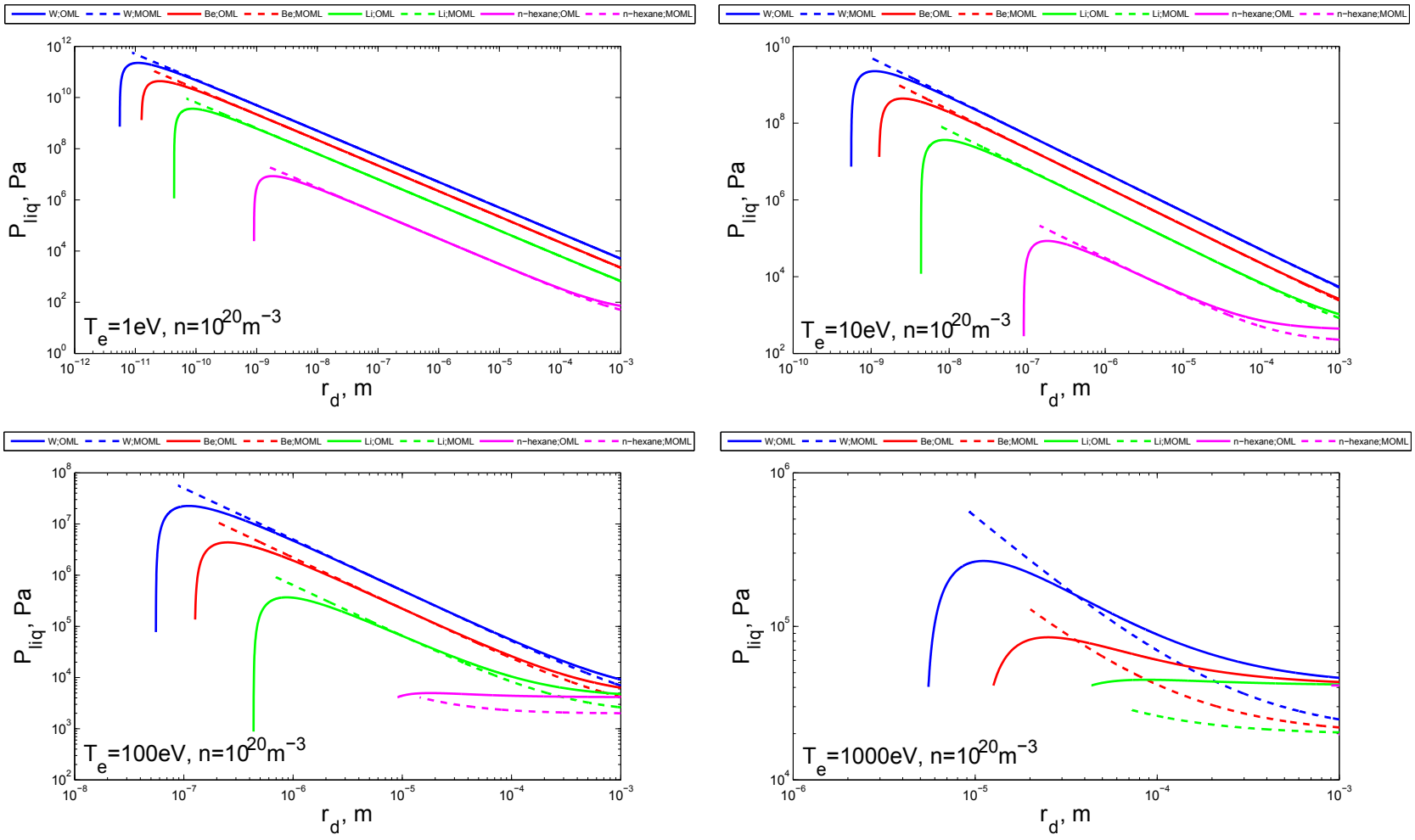


Figure 5.2: The figure shows the trends of liquid pressures when the droplets allow evaporation, where the tungsten (W), beryllium (Be), lithium and n-hexane droplets are in the plasma of $n = 10^{20}$ m^{-3} and $T_e = 1 - 1000$ eV. The solid lines correspond to OML. The dashed lines correspond to MOML.

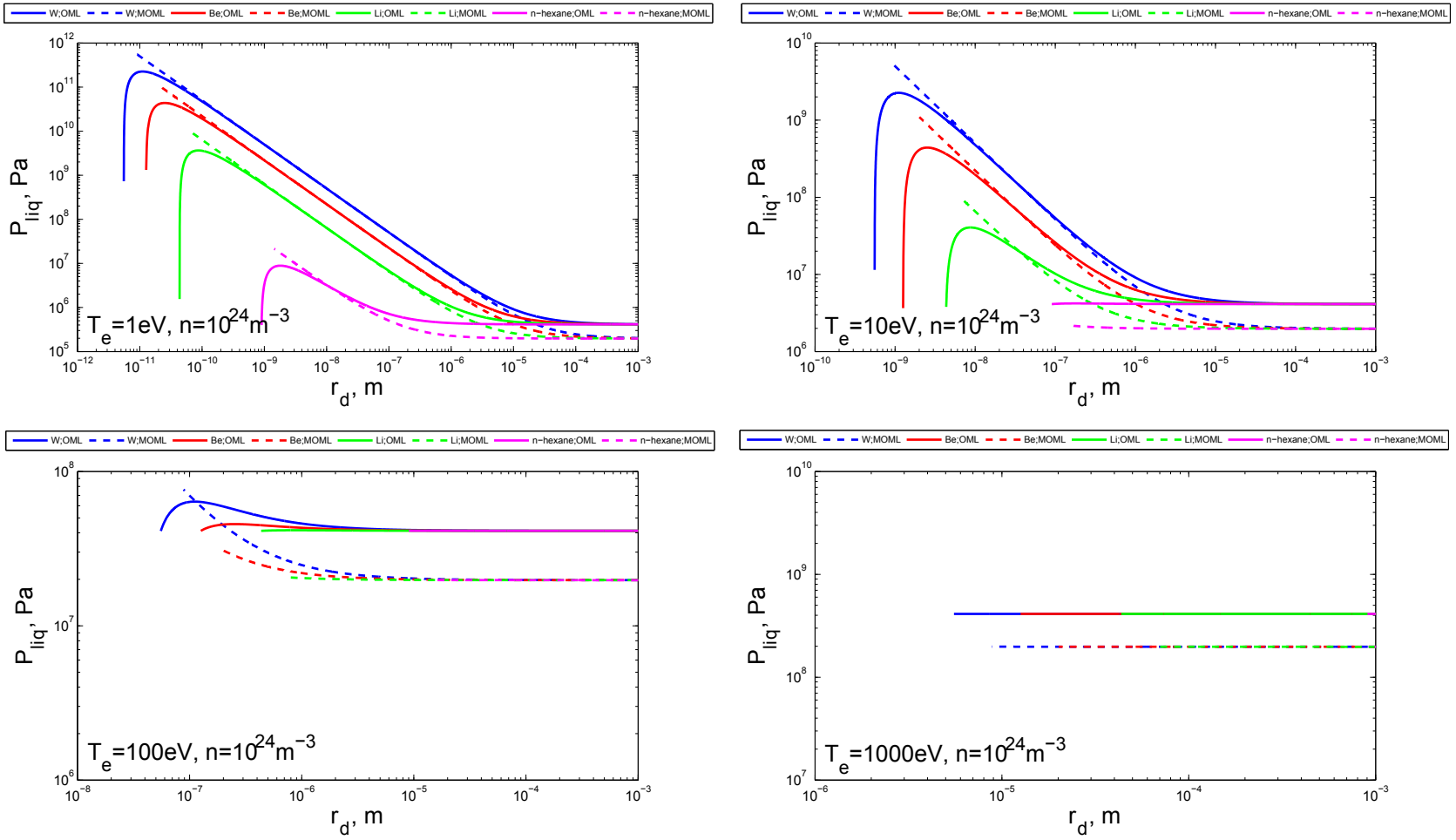


Figure 5.3: The figure shows the trends of liquid pressures when the droplets allow evaporation, where the tungsten (W), beryllium (Be), lithium and n-hexane droplets are in the plasma of $n = 10^{24}$ m^{-3} and $T_e = 1 - 1000$ eV. The solid lines correspond to OML. The dashed lines correspond to MOML.

This leads to the possibility that $P_{ext} = \Gamma_i + P_e$ dominates P_{liq}. The P_{st} and P_{es} are much lower for large r_d and cancel each other when r_d falls to $r_{d,min}$. Therefore, these two pressures are important only for determining the electrostatic stability of the droplet in this condition.

It appears that if a droplet can avoid electrostatic breakup and reach very small r_d, it can access $P_{liq} \gg 1$ atm by the contribution of either P_{st}, for non-extreme plasma parameters, or $P_{st} + P_{ext}$ for extreme ones. We notice that at $T_e < 100$ eV, $P_{liq} \gg 1$ atm and at $T_e > 100$ eV, $P_{liq} < 1$ atm. This is because the droplet potential, ϕ_d, is proportional to T_e. Thus increase T_e, increase the outward electrostatic term in the modified Laplace equation. In general, the higher surface tension, the higher P_{liq}. Moreover, P_{ext} does not contribute to the equibrium condition but only the electrostatic instability.

5.4 Conclusions

We find that P_{liq} is generally dominated by P_{st} except the high n and T_e which causes P_{liq} depends on $P_{st} + P_{ext}$. The droplet can reach $P_{liq} \gg 1$ atm if $T_e < 100$ eV and $P_{liq} < 1$ atm if $T_e > 100$ eV.

The summary above reflects in the influence on the behavior of the molten metallic dust grains in tokamaks. With the consideration of figure 5.2, the SOL plasma ($T_e < 100$ eV) allows metallic droplet to reach very high P_{liq} and triggers electrostatic breakup at very small r_d, i.e. $r_{d,min} < 0.01$ micron approximately. In contrast, the core plasma ($T_e > 100$ eV) does not allow metallic droplet to reach very high P_{liq} but keep it to be ~ 1 atm. This can affect the pressure-variation properties of the droplet material , e.g. boiling temperature (T_{boil}).

In chapter 6, we study a charged bubble in a plasma. The bubble can be introduced in a fusion plasma via a superheating which transforms a droplet to a vapor bubble. By the use of the study in this chapter, we can relate the situation how a droplet that avoids electrostatic breakup can transform to a bubble. This is crucial because the electrostatic stability of the droplet and the bubble are different and their stability limits are too. We consider a 1-μm W droplet in the SOL plasma. The droplet are stable and reach $P_{liq} > 1$ atm. This results in an increase in T_{boil} with respect to the liquid-vapor P-T diagram which is derived from the Clausius-Clapeyron equation. The T_{boil} indicates the maximum

temperature that the droplet can have at a certain liquid pressure, which is equal to a saturated vapor pressure. If the droplet in the SOL rapidly moves to the core, for instance across the edge transport barrier in the ELMy H-mode operation, P_{liq} and T_{boil} of the droplet are reduced due to the high n and T_e. As a result, the rapid reduction of P_{liq} causes a sudden reduction in T_{boil} and then a droplet becomes superheated and transforms to a bubble. Subsequently, this should provide the superheated vapour explosion [81, 82] which deposits impurities. If with some mechanism the droplet passes across the edge transport barrier but then turns back into the SOL where T_{boil} is higher, explosive boiling is not triggered and the droplet temperature continues to rise normally.

Chapter 6

A BUBBLE IN A PLASMA

This chapter presents an entirely new postulated phenomenon: plasma bubbles. There are plasma immersed cavities, possibly contain vapor and which can carry charges on their surfaces. Section 6.1 introduces the possibilities to find bubbles in tokamak plasmas. Section 6.2 gives the detail of the modification applied to the original Rayleigh's limit [53] for determining the electrostatic instability of a charged bubble in a plasma. Sections 6.3 and 6.4 show and discuss the preliminary results of the trends of bubble instability under the effect of external pressure.

6.1 A charged bubble in a plasma

Because tokamak plasmas are so hot that they can boil metals, e.g. plasma facing surfaces, then bubbles can be generated in a molten layer (see figure 3 in ref. [16] and figures 1 and 4 in ref. [24]) and subsequently it is possible for them to transport into the plasma. They may transport together with droplets from the molten layer. The bubbles produced from the boiled molten layer should be in forms of vapor enveloped by thin layers of liquid. Unlike a droplet, inside a bubble, it has vapour filling, so it can be compressible.

Moreover, a droplet can be superheated. It is found that a superheated droplet can have a space filling inside with vapor (see figures 9 and 11 in ref. [81] and figures 7 and 10 in ref. [82]). The superheated droplet can be achieved by boiling temperature variation caused by rapid changing in liquid (net) pressure on a droplet [81]. This can be due to the sharp gradients of plasma parameters, i.e. the plasma number density and temperature, which the droplet is passing through. This results in a significant drop of the droplet boiling

temperature because the liquid pressure, which is equal to the saturated vapor pressure, is decreased. From this, the superheated droplet evolves to the bubble. The superheating may exist in tokamak plasma backgrounds, e.g. the edge transport barrier's plasma number density and temperature during operating in the ELMy H-mode. The bubble is compressible, in other words, the volume of the bubble can be changed. This implies that to study the electrostatic stability of a charged bubble in a plasma, Rayleigh's limit has to be modified by taking into account the work done by external pressure, i.e. ion and electron pressures and a pressure due to neutral recombination, which the original Rayleigh's limit omitted. A similar approach was used for a completely different situation by J. Tempere *et al* (2001) [83] who adopted Rayleigh's model with the appropriate modification for studying the evolution of a multielectron bubble in a liquid helium.

6.2 Electrostatic stability limit of a charged bubble in a plasma

In the previous sections, the electrostatic instability of a charged droplets is discussed. Chapter 3 reviews Rayleigh's stability analysis for a charged droplet and also the electrostatic stability limit for a small droplet in a plasma and chapter 4 considers the electrostatic instability of a large droplet in various plasma systems. However, the approaches mentioned in the previous sections, which are for a charged droplet in a plasma, require some modifications before using for studying a charged bubble in a plasma.

In this section, the electrostatic instability of a charged bubble is discussed. Similar to the charged droplet, surface tension contracts inwardly on the bubble surface. In equlibrium, surface tension balances the outward electrostatic force. Electrostatic breakup occurs when electrostatic force start to be larger than surface tension. The infinitesimal surface perturbation changes the surface energy via the change in the surface area and also the electrostatic potential energy through the change in surface charge density. A crucial point which causes the stability limit of a charged droplet different from that of a charged bubble is the fact that the bubble is compressible. Therefore, there is no constraint related to incompresibility for the case of a bubble in a misty plasma. This leads to the fact that the infinitesimal surface perturbation can change the bubble volume. As a result, the additional work done by external pressure needs to be considered for determining the electrostatic stability limit of a charged bubble in a misty plasma.

To determine the electrostatic stability limit of a charged bubble in a plasma, we start from the use of the Lagrange equation [64] in eq. 3.142 with the Lagrangian, $\mathcal{L}$,

$$\mathcal{L} = \Delta(\mathrm{KE}) - \Delta(\mathrm{PE}), \tag{6.1}$$

where Δ(KE) and Δ(PE) are the changes in the total kinetic energy and the total potential energy. We can use Δ(KE) indicated in eq. 3.141,

$$\Delta(\mathrm{KE}) = 2\pi\rho R^3 \sum_{\ell=1}^{\infty} \frac{\dot{\xi}_\ell^2}{\ell(2\ell+1)}. \tag{6.2}$$

However, Δ(PE) has to be re-derived. It has to note that we follow all variables defined in chapter 3. We start from the droplet radius perturbation,

$$r = R + \sum_{\ell=1}^{\infty} \xi_\ell(t) P_\ell(\cos\theta), \tag{6.3}$$

where R is the original or unperturbed radius and replaces ξ_0 to ensure the change in the bubble volume. Note that there will in general be an $\ell = 0$ mode, but we assume it is always stable. Following the way to evaluate the surface area perturbation from eq. 3.3 to eq. 3.35, we get the perturbed surface area of the bubble (A),

$$A = 4\pi R^2 + 2\pi \sum_{\ell=1}^{\infty} \frac{\left(\ell^2+\ell+2\right)\xi_\ell^2}{2\ell+1}. \tag{6.4}$$

The change in the surface energy ($\Delta(\mathrm{PE})_\mathrm{s}$) is

$$\Delta(\mathrm{PE})_\mathrm{s} = 4\pi\sigma \sum_{\ell=1}^{\infty} \frac{\left(\ell^2+\ell+2\right)\xi_\ell^2}{2\ell+1}. \tag{6.5}$$

Note that the factor of 2 in the RHS of eq. 6.5 are introduced because the bubble has an inner and outer surface. For the change in the electrostatic potential energy $\Delta(\mathrm{PE})_\mathrm{E}$, we can use eq. 3.119

$$\Delta(\mathrm{PE})_\mathrm{E} = -\frac{Q^2}{8\pi\varepsilon_0} \sum_{\ell=1}^{\infty} \frac{(\ell-1)\xi_\ell^2}{(2\ell+1)R^3} \tag{6.6}$$

directly. We introduce the additional work done by all external pressures ($\mathrm{W_{ext}}$), i.e. ion

and electron pressures, a pressure due to neutral recombination and a neutral pressure, as the extra term, specific for the charged bubble in a plasma or any medium, in $\Delta(\mathrm{PE})$. The work (W) done by the system (bubble) in response of W_{ext} are

$$\begin{aligned} W &= -W_{ext} && (6.7)\\ &= P_{ext}\Delta V && (6.8)\\ &= P_{ext}\left(4\pi R\sum_{\ell=1}^{\infty}\frac{\xi_\ell^2}{2\ell+1}\right), && (6.9)\end{aligned}$$

where ΔV is the change in the bubble volume from the surface perturbation (see eq. 3.52), which can be evaluated by replacing ξ_0 with R and following eq. 3.42 to eq. 3.53. Therefore, $\Delta(\mathrm{PE})$ is

$$\begin{aligned} \Delta(\mathrm{PE}) &= \Delta(\mathrm{PE})_{\mathrm{s}} + \Delta(\mathrm{PE})_{\mathrm{E}} + W && (6.10)\\ &= 4\pi\sigma\sum_{\ell=1}^{\infty}\frac{\left(\ell^2+\ell+2\right)\xi_\ell^2}{2\ell+1} - \frac{Q^2}{4\pi\epsilon_0}\sum_{\ell=1}^{\infty}\frac{(\ell-1)\,\xi_\ell^2}{(2\ell+1)\,R^3} + 4\pi RP_{ext}\sum_{\ell=1}^{\infty}\frac{\xi_\ell^2}{2\ell+1} && (6.11)\end{aligned}$$

Hence, the Lagrangian ($\mathcal{L}$) is

$$\begin{aligned} \mathcal{L} &= 2\pi\rho R^3\sum_{\ell=1}^{\infty}\frac{\dot{\xi}_\ell^2}{\ell(2\ell+1)} - 4\pi\sigma\sum_{\ell=1}^{\infty}\frac{\left(\ell^2+\ell+2\right)\xi_\ell^2}{2\ell+1} + \frac{Q^2}{4\pi\epsilon_0}\sum_{\ell=1}^{\infty}\frac{(\ell-1)\,\xi_\ell^2}{(2\ell+1)\,R^3}\\ &\quad -4\pi RP_{ext}\sum_{\ell=1}^{\infty}\frac{\xi_\ell^2}{2\ell+1} && (6.12)\end{aligned}$$

We follow the way to calculate the Lagrange equation (see eq. 3.142) from eq. 3.145 to eq. 3.148, we get

$$\frac{d^2\xi_\ell}{dt^2} + \frac{\ell\xi_\ell}{\rho R^3}\left(2\sigma\left(\ell^2+\ell+2\right) - \frac{(\ell-1)\,Q^2}{16\pi^2\epsilon_0 R^3} + 2RP_{ext}\right) = 0. \qquad (6.13)$$

After substituting $\xi_\ell(t) \propto \exp(i\omega t)$, we obtain the dispersion relation for the charged bubble in a plasma,

$$\omega^2 = \frac{\ell}{\rho R^3}\left(2\sigma\left(\ell^2+\ell+2\right) - \frac{(\ell-1)\,Q^2}{16\pi^2\epsilon_0 R^3} + 2RP_{ext}\right). \qquad (6.14)$$

The electrostatic stability limit of the charged bubble in a misty plasma is defined at $\omega^2 = 0$,

$$2\sigma\left(\ell^2+\ell+2\right) - \frac{(\ell-1)\,Q^2}{16\pi^2\epsilon_0 R^3} + 2RP_{ext} \;=\; 0. \tag{6.15}$$

After a few rearrangement, we obtain

$$Q^2_{max} \;=\; 32\pi^2\epsilon_0\sigma R^3\frac{\left(\ell^2+\ell+2\right)}{\ell-1} + \frac{32\pi^2\epsilon_0 P_{ext}R^4}{\ell-1} \tag{6.16}$$

$$\;=\; \frac{32\pi^2\epsilon_0 R^3}{\ell-1}\left(\sigma\left(\ell^2+\ell+2\right)+RP_{ext}\right) \tag{6.17}$$

Eq. 6.17 is the general form of the electrostatic stability limit of the charged bubble with the presence of external pressure. The instabiliy occurs if the bubble surface charges exceed the amount corresponding to that in eq. 6.17. To use the stability limit in a misty plasma, we require a slight modification of eq. 6.15 in terms of the floating potential by the substitution of $Q_{max} = 4\pi\epsilon_0 r_{d,crit}\phi_d$, which is a spherical self-capacitance in a vacuum. We define $r_{d,crit}$ for the critical bubble radius to initiate the electrostatic breakup, therefore eq. 6.15 can be re-written into

$$2P_{ext}r^2_{d,crit} + 2\sigma\left(\ell^2+\ell+2\right)r_{d,crit} - \epsilon_0\phi_d^2\left(\ell-1\right) \;=\; 0, \tag{6.18}$$

and using the root finding formula, we obtain

$$r_{d,crit} \;=\; \frac{-2\sigma\left(\ell^2+\ell+2\right)+\sqrt{4\sigma^2\left(\ell^2+\ell+2\right)^2+8\left(\ell-1\right)\epsilon_0\phi_d^2P_{ext}}}{4P_{ext}}. \tag{6.19}$$

6.3 Results and discussions

In section 6.2, the derivation was conducted to find the formula for the critical radius of a bubble ($r_{d,crit}$) in a plasma, the radius at which an excessively charged bubble starts to electrostatically breakup (see eq. 6.19), which can be written in

$$r_{d,crit} \;=\; \frac{-2\sigma\left(\ell^2+\ell+2\right)+\sqrt{4\sigma^2\left(\ell^2+\ell+2\right)^2+8\left(\ell-1\right)\epsilon_0\phi_d^2P_{ext}}}{4P_{ext}}, \tag{6.20}$$

Table 6.1: The set-up parameters of the works shown in figures 6.1-6.5

Bubble materials	W, Fe, Be, Li, and n-hexane (C_6H_{14})
Plasma	singly charged hydrogen (H^+)
Ratio of ion and electron tempertaures ($\beta = T_i/T_e$)	1.0
Electron temepratures (T_e)	10.0, 100.0, 1000.0 and 10000.0 eV
Plasma number density ($n_i = n_e = n$)	10^{13}, 10^{16}, 10^{19}, 10^{22} and 10^{25} m^{-3}

where $P_{ext} = \Gamma_i + P_e + P_r$ is a net external pressure. The formula is a function for surface tension, the bubble floating potential (ϕ_d), the net external pressture (P_{ext}) and the mode number of the infinitesimal surface perturbation (ℓ) introduced by Legendre polynomials. To understanding the formula, we note that $r_{d,crit} = 0$ if $\ell = 1$ or no charge is on the bubble, which results in $\phi_d = 0$. Furthermore, if $P_{ext} \to 0$, we can show that

$$r_{d,crit} = \frac{2\epsilon_0\phi_d^2\,(\ell-1)}{\sigma\,(\ell^2+\ell+2)}, \tag{6.21}$$

which determines the electrostatic stability of the charged bubble in a vacuum or a dilute gas. We notice that the maxmum value of $\frac{(\ell-1)}{(\ell^2+\ell+2)}$ occurs at $\ell = 3$, i.e. the minimum stable bubble size is given by

$$r_{d,crit} = \frac{2\epsilon_0\phi_d^2}{7\sigma}. \tag{6.22}$$

As we decrease the bubble size below $r_{d,crit}$, we find, surprisingly, that the first mode to be unstable is $\ell = 3$, in contrast to the droplet case where $\ell = 2$ (see section 3.2.1). However, we expect that the presence of plasma should deviate the most basic mode from $\ell = 3$ to $\ell \neq 3$. In other words, it is possible to initiate the electrostatic breakup of an charged bubble with $r_{d,crit}$ of the mode $\ell \neq 3$. The shape of electrostatic deformation is even more complex. To see how P_{ext} affect the most basic $r_{d,crit}$ value, we plot several figures, whose setups are shown in table 6.1, to investigate this.

Figures 6.1-6.5 are plotted for considering critical radius of charged bubbles at various mode numbers of infinitesimal surface perturbation. We use only the OML floating potential [38–40] for ϕ_d (see eq. 1.1). We vary plasma number densities and temperatures and selected materials for bubbles, i.e. tungsten, iron, beryllium, lithium and n-hexane. Plasma number densities are ranged from $n = 10^{13} - 10^{25}\mathrm{m}^{-3}$, which cover most conditions

of well-known plasma systems, i.e. low pressure plasmas, tokamak scrape-off layer (SOL) and core plasmas and high pressure plasmas, e.g. plasma torch used in plasma spraying and wire array z-pinch plasmas. This is also applicable for electron temperatures, ranged from $T_e = 10.0 - 10000.0$ eV; however, $\beta = 1.0$, where ion and electron temperatures are equal ($T_i = T_e$) is only considered in this study. The surface tensions of those bubble materials can be seen table 4.1. Only hydrogen plasma is used in the study. Hence, we focus on the effect on a charged bubble in a plasma through: surface tension (σ); plasma number density (n); electron temperature (T_e). This causes nearly the highest magnitude of negative floating potential (see figure 4.3), where electric field on the bubble surfaces is large and help to initiate the instability easier.

We consider figures 6.1-6.5. We discover that with the final term in the RHS of eq. 6.19 shifts the most basic mode from $\ell = 3$ to higher ℓ. The term is linearly proportional to n but nonlinearly propotional to T_e with higher order. Therefore, after consider all figures, we can see that the the most basic mode is shifted by the final term in the RHS of eq. 6.19 through the effects from T_e in P_{ext} and ϕ_d and the relatively high value of n. With the same plasma parameters, the mode shift for the bubble with the lower surface tension is more influenced by the final term in the RHS of eq. 6.19. This results in that the most basic mode occurs at higher ℓ (adding after the PhD viva).

In figure 6.5, we see that the n-hexane bubble is easiest to be electrostatically broken up because n-hexane is low in surface tension. Therefore, for every ℓ, the associated $r_{d,crit}$ are the highest. (The lower $r_{d,crit}$, the higher stability.) In contrast, considering figures 6.1 - 6.4, the metallic bubbles are harder to undergo electrostatic breakup unless the bubble is very small or n and T_e are so high. Among the metals in this study, the tungsten bubble is hardest to undergo electrostatic breakup because the lowest $r_{d,crit}$ for every ℓ.

We plot figure 6.6 by choosing the n-hexane bubble because of its lowest surface tension. We select hydrogen (H^+), argon (Ar^+) and xenon (Xe^+) to represent light, medium and heavy plasmas. The $T_e = 10.0$ and 100.0 and $n = 10^{13}$ and $10^{25}\mathrm{m}^{-3}$ are considered. We see that the lighter plasma, the greater in stability and the lower $r_{d,crit}$ of all ℓ. This can be explained by the use of figure 4.4. The more negative floating potential can be achieved by the heavier plasma. The electric field of the bubble is stronger and encourages the electrostatic breakup. Moreover, if n and T_e are high and their values are the same for

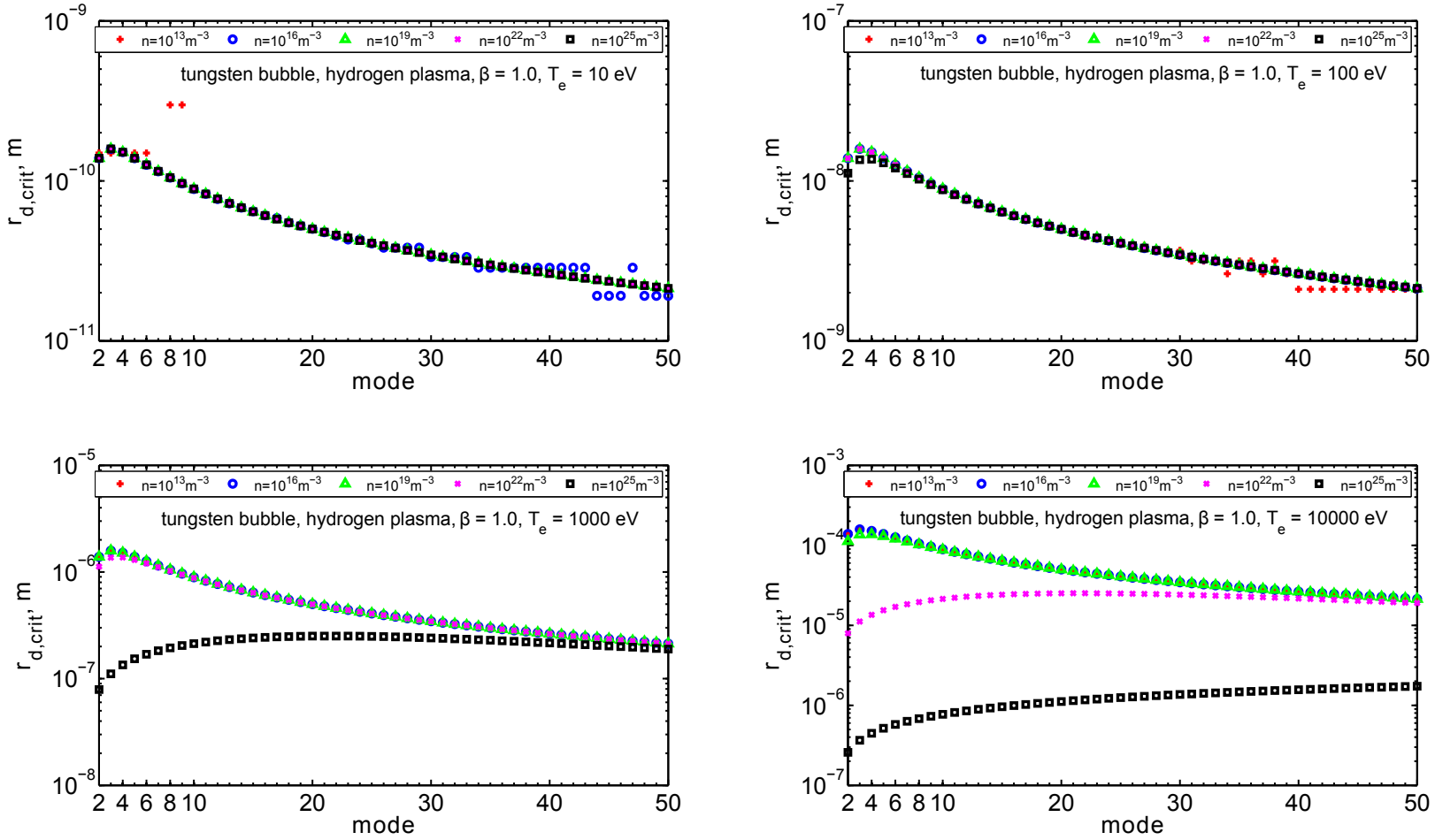


Figure 6.1: The plots of a critical radius ($r_{d,crit}$) of a charged tungsten (W) bubble and mode number (ℓ) of the surface perturbation in hydrogen (H^+) plasma with $\beta = 1.0$, $T_e = 10.0, 100.0, 1000.0$ and 10000.0 eV and plasma number density ($n_i = n_e = n$) = 10^{13}, 10^{16}, 10^{19}, 10^{22} and 10^{25} m^{-3}.

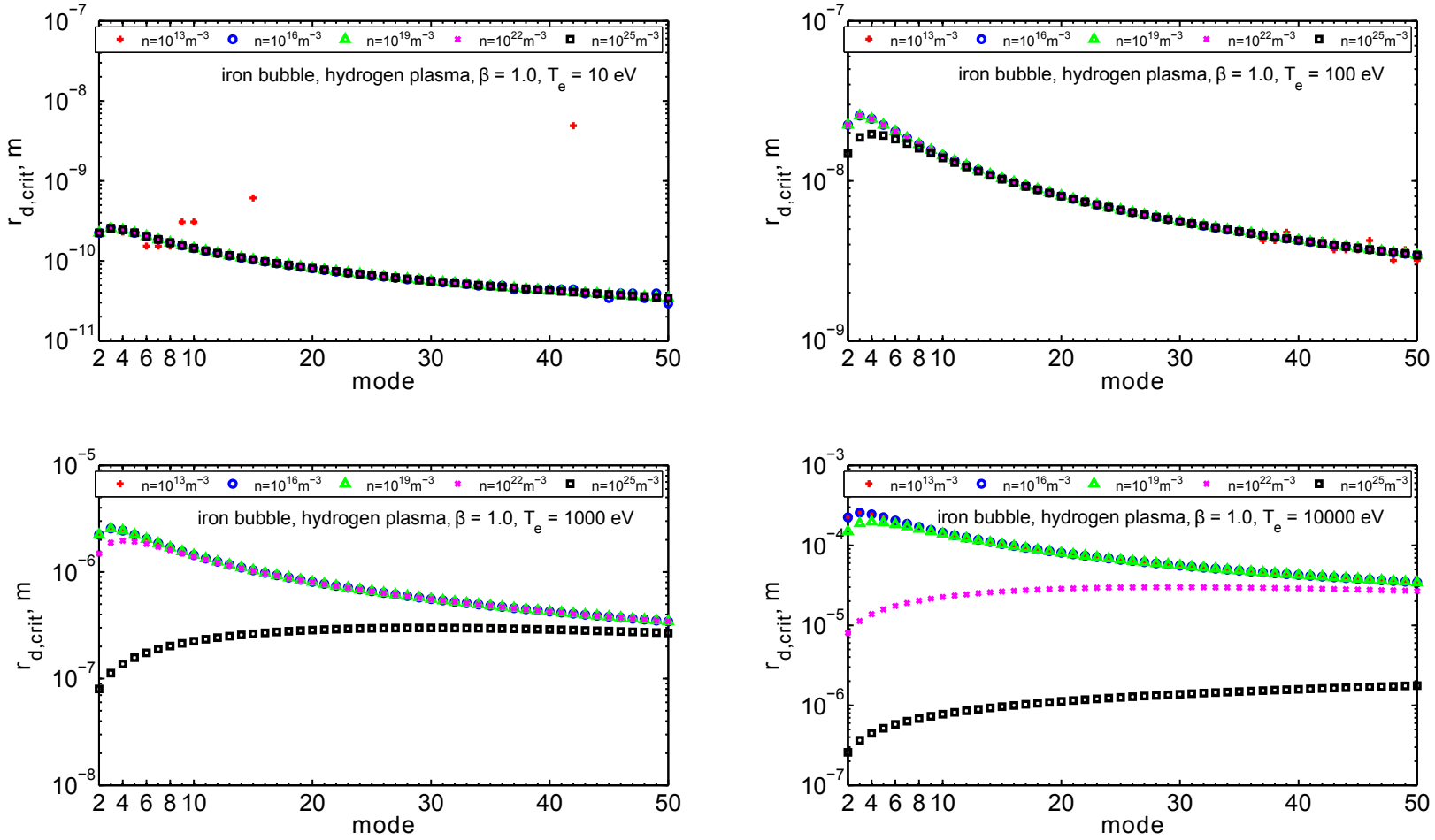


Figure 6.2: The plots of a critical radius ($r_{d,crit}$) of a charged iron (Fe) bubble and mode number (ℓ) of the surface perturbation in hydrogen (H^+) plasma with $\beta = 1.0$, $T_e = 10.0, 100.0, 1000.0$ and 10000.0 eV and plasma number density ($n_i = n_e = n$) = 10^{13}, 10^{16}, 10^{19}, 10^{22}. and 10^{25} m^{-3}

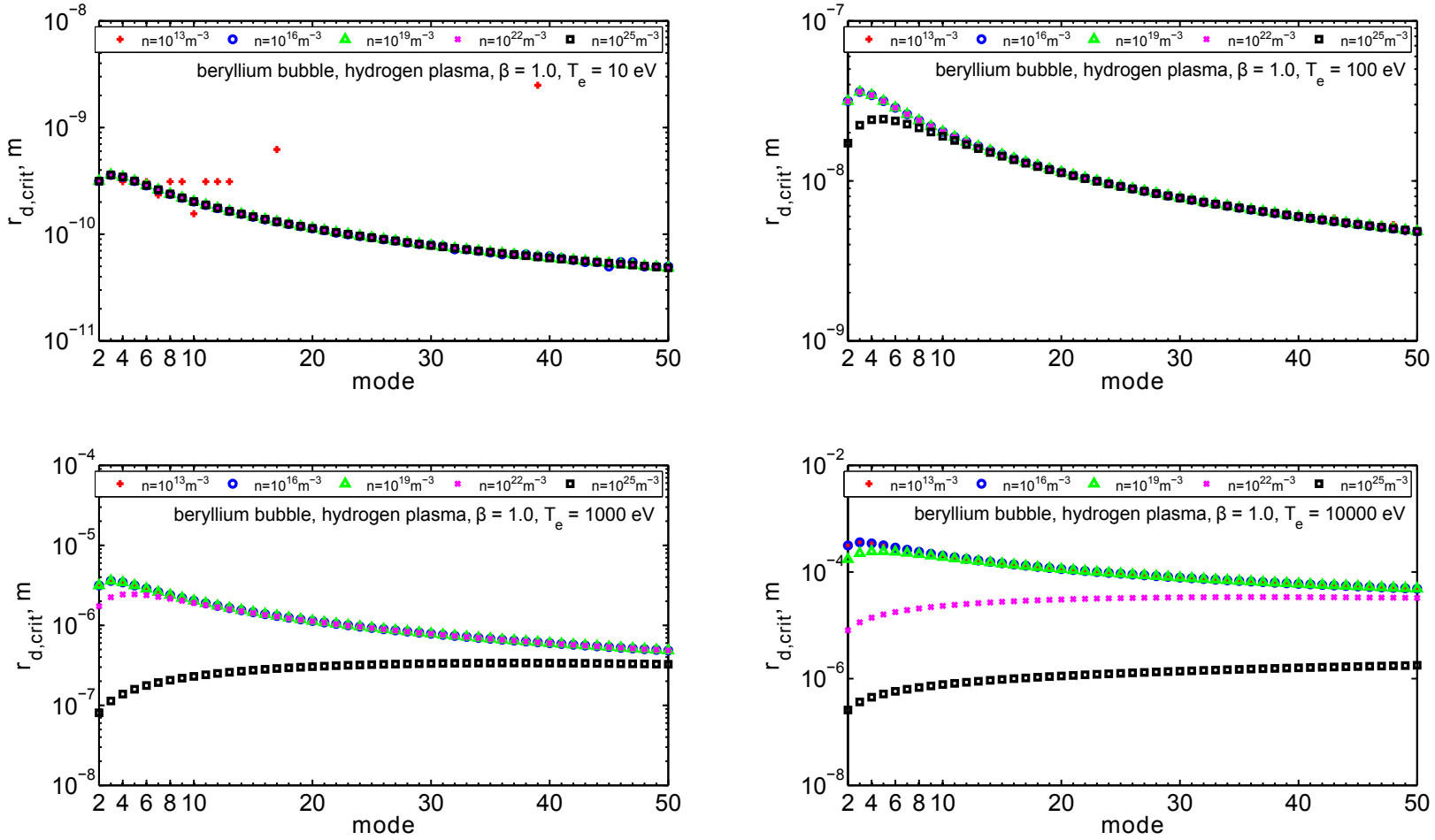


Figure 6.3: The plots of a critical radius ($r_{d,crit}$) of a charged beryllium (Be) bubble and mode number (ℓ) of the surface perturbation in hydrogen (H^+) plasma with $\beta = 1.0$, $T_e = 10.0, 100.0, 1000.0$ and 10000.0 eV and plasma number density ($n_i = n_e = n$) = 10^{13}, 10^{16}, 10^{19}, 10^{22}. and 10^{25} m^{-3}

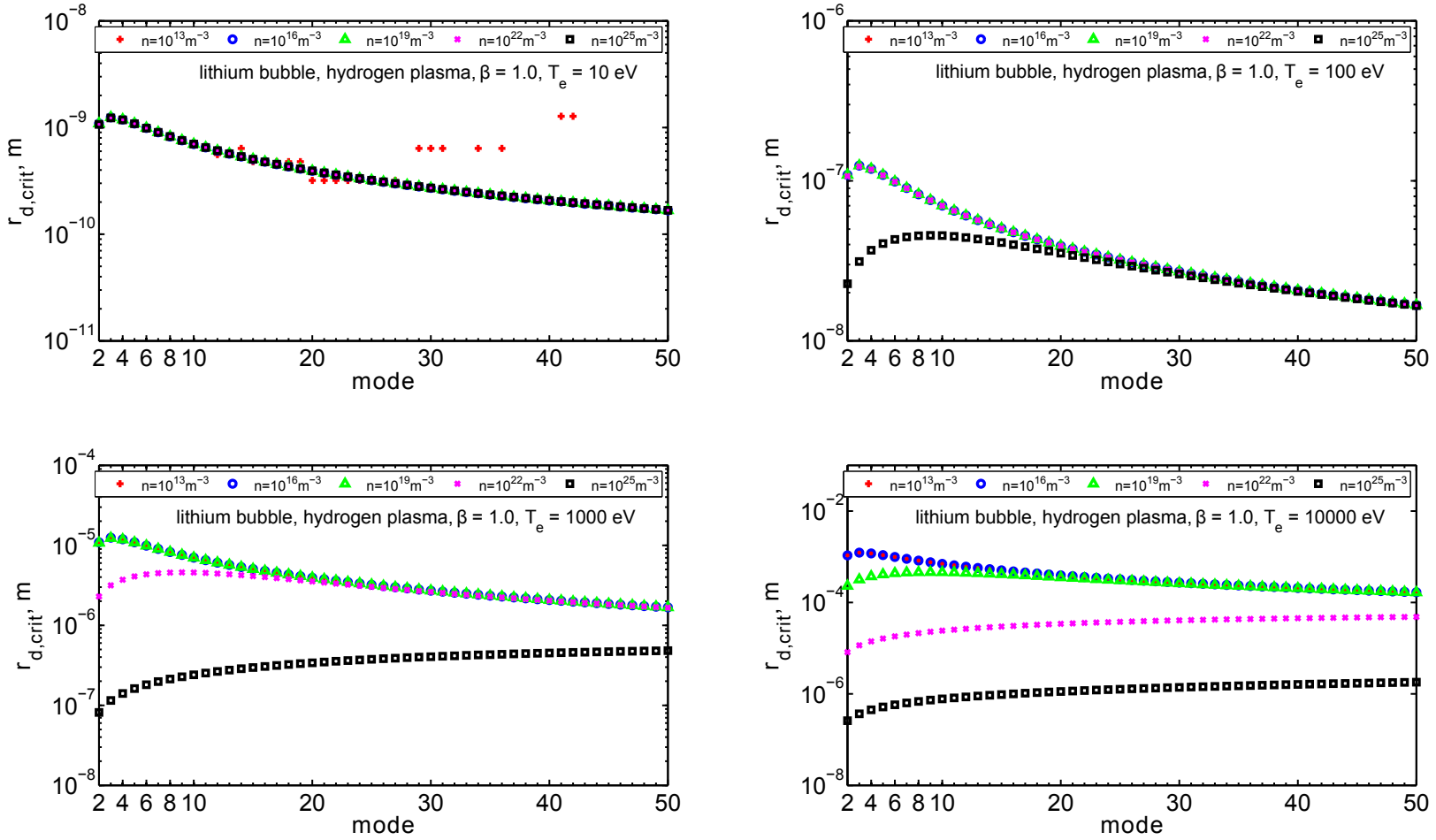


Figure 6.4: The plots of a critical radius ($r_{d,crit}$) of a charged lithium (Li) bubble and mode number (ℓ) of the surface perturbation in hydrogen (H^+) plasma with $\beta = 1.0$, $T_e = 10.0, 100.0, 1000.0$ and 10000.0 eV and plasma number density ($n_i = n_e = n$) = 10^{13}, 10^{16}, 10^{19}, 10^{22}. and 10^{25} m^{-3}

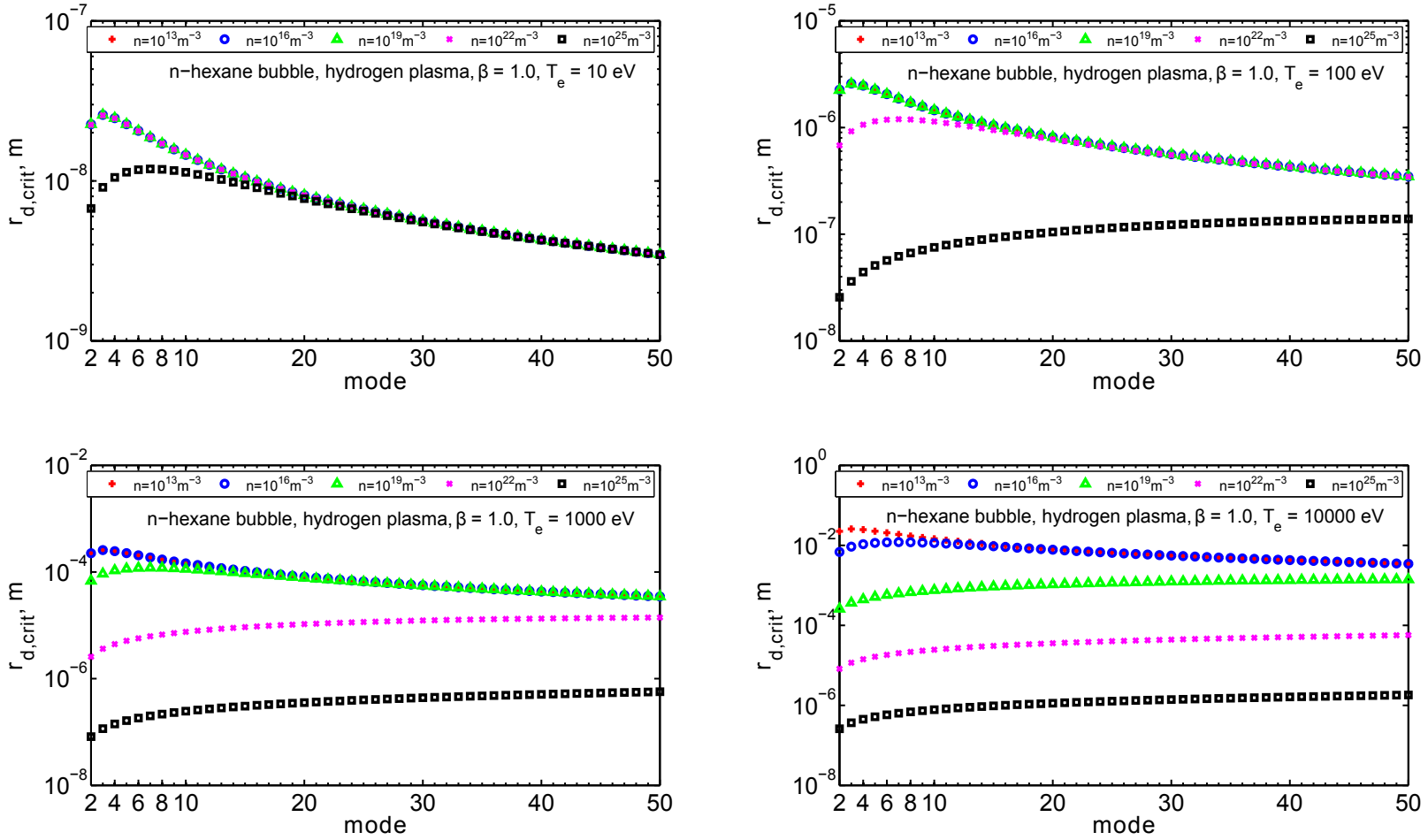


Figure 6.5: The plots of a critical radius ($r_{d,crit}$) of a charged n-hexane (C_6H_{14}) bubble and mode number (ℓ) of the surface perturbation in hydrogen (H^+) plasma with $\beta = 1.0$, $T_e = 10.0, 100.0, 1000.0$ and 10000.0 eV and plasma number density ($n_i = n_e = n$) = 10^{13}, 10^{16}, 10^{19}, 10^{22} and 10^{25} m^{-3}.

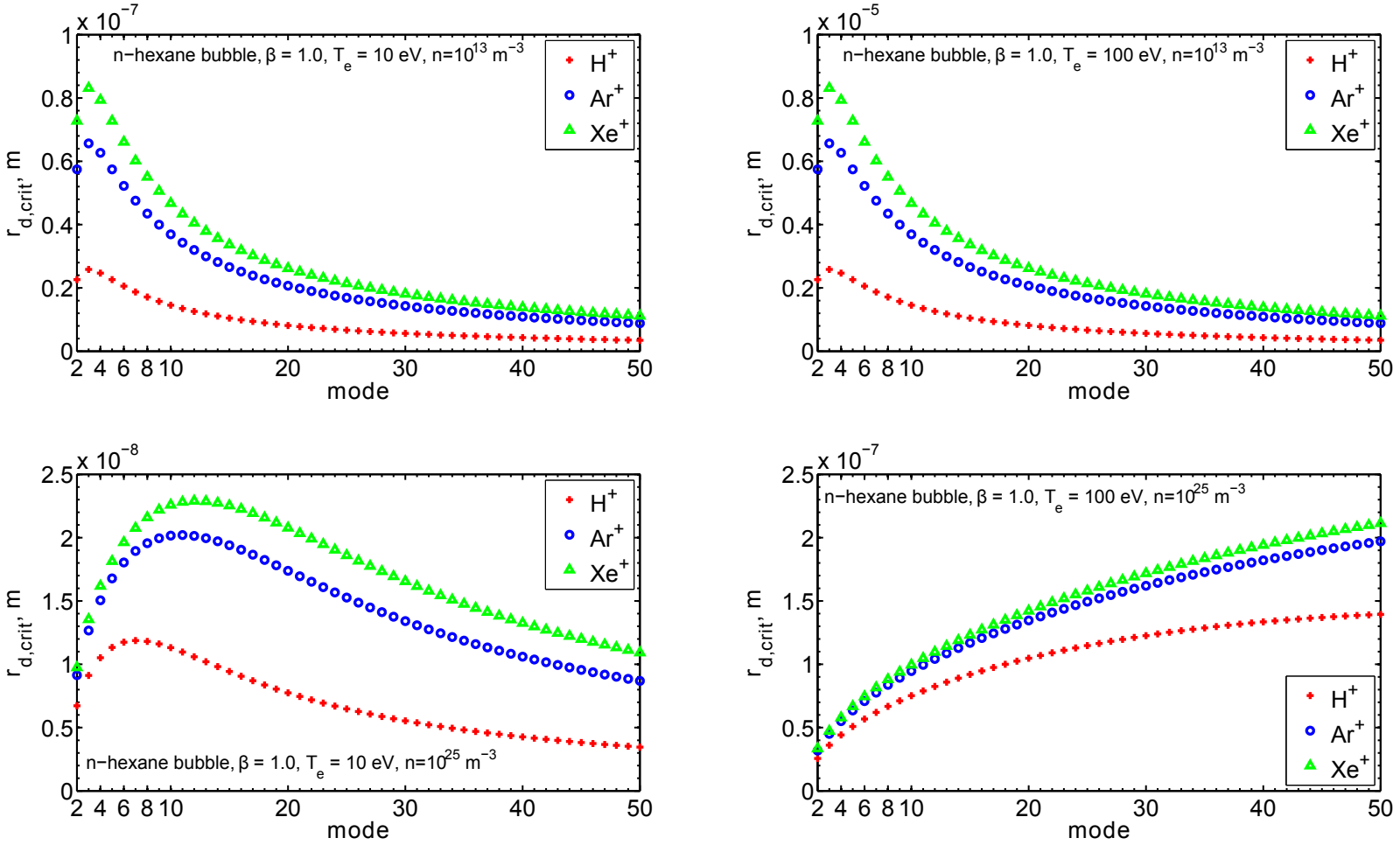


Figure 6.6: The plots of a critical radius ($r_{d,cri}$) of a charged n-hexane (C_6H_{14}) bubble and mode number (ℓ) of the surface perturbation in hydrogen (H^+), argon (Ar^+) and xenon (Xe^+) plasmas with $\beta = 1.0$, $T_e = 10.0$ and 100.0 eV and plasma number density ($n_i = n_e = n$) = 10^{13} and 10^{25} m^{-3}.

all plasmas, it appears that the shift of the most basic mode is further to the higher ℓ if the plasma is heavier.

6.4 Conclusions

The electrostatic stability limit of a charged bubble is determined at the mode $\ell = 3$ for a low density medium and can be $\ell > 3$ by strong P_{ext} and ϕ_d if the bubble is in a plasma. Surface tension, electron temeprature, plasma number density and mass of a plasma ion control the stability. Strong surface tension stabilises but high electron temperature, plasma number density and large plasma ion mass destabilise the charged bubble.

The use of the physics of a charged bubble in a plasma can be applied on the motion of superheated molten droplets as they cross the edge transport barrier in the ELMy H-mode plasma. The sudden drop in boiling temperature causes superheating and the rapid formation of a bubble. Electrostatic disintegration of the bubble by the mechanism described here enhancing the superheated bubble's vapour explosion [81, 82] would cause localized impurity deposition this region. By these two effects, the impurity deposition in a fusion plasma should be more serious and especially affect the H-mode operation.

Another issue is related to dust voids formed in a dusty plasma in microgravity [84]. As can be seen in figure 11 in ref. [84], a dust void is generally in the form of the steady state dynamic structure. The boundary of the void is well-determined and charged by the plasma particles. Its ends eject the charged dust formed in the boundary out of the structure. Many ejected dust forms the circulation next to the void which should later give the chance for them to come back in the boundary and enchance charging. It looks like a steady state dynamic structure. Compared to the electrostatic breakup of a charged bubble where the bubble boundary are also charged and well-determined, we may adopt the physics of the electrostatic breakup of a charged bubble to study a dust void, which we call it a plasma bubble, in a simpler way. In some ways, we may use the physics of the electrostatic stability analysis for a charged bubble to determine e.g. an effective void surface tension or a void interface attractive force and a stability of the void structure etc.

Chapter 7

FUTURE WORK

Our studies in this thesis focus on the metallic dust grains which are produced in metallic tokamaks. ITER [1–3] is planned to have the beryllium first wall and the tungsten divertors. To test the efficiency of the use of those metallic surfaces, JET with ITER-like wall [1–3], ASDEX Upgrade with full-tungsten surfaces [4–6] and Tore-Supra with the WEST divertors [7, 8] adopt the ITER related metallic surfaces. Not only ITER but also these tokamaks should produce a large amount of metallic dust grains. To accurately understand their behaviors, we require dust simulations. We hope that our study of misty plasma should help the dust simulations more accurately. Therefore, one of our main future works is to apply the knowledge of misty plasma into DTOKS [9–13], dust transport code, to specifically study metallic dust grain motion.

With regard to high velocity dust grains, we may extend our work to investigate the effects from the variation of the material properties and the aspect-ratio of the tokamak to enhance or suppress the high velocity dust grains.

The stability limit of a large droplet in a plasma is based on the use of a vacuum capacitance to related charges with floating potential. This is for simplicity; however, for more accuracy, we should add the term $\exp\left(-r_d/\lambda_D\right)$ into the vacuum capacitance to change it to the capacitance in a plasma.

The study in the thesis provides the model of ion and electron pressures and the stability limit for a small and large droplet. However, we should work more on the determination of these values in the transition from small to large droplet. A possibility should be related to the use of the transition region, suggested in C.T.N. Willis *et al* (2010)

[41], of OML [38–40] to MOML [42] to determine a floating potential on the droplet. Then, we should acquire the ion and electron pressures and the stability limit at the transition region. We can relate the two models continuously.

We have studied a charged droplet in a plasma in terms of stability limit ($r_{d,min}$) and equilibrium condition determining liquid pressure (P_{liq}); however the droplet we consider is at rest. Practically, the droplet can move in the plasma, e.g. due to a tokamak plasma rotation. The electrostatic breakup should be coupled with e.g. the instability of flow-induced droplet breakup [68] and some instability of a droplet moved in a non-uniform field. The electrostatic stability limit changes. We also expect an asymmetric plasma flow, so the droplet may not in equilibrium but the shear flow and rotation may contribute an additional deformation to the charged droplet. This may perturb the original charge configuration and then exhibit unusual forms of electrostic breakup.

With regard to a charged bubble in a plasma, we have 2 aspects about this issue. Dust voids [84] show the steady state dynamic structure which is comparable to that of electrostatic breakup. We may be able to apply the physics of misty plasma to determine some parameters of dust voids e.g. effective surface tension or interface attractive force. Superheated droplets may occur at the edge transport barrier and then they transform to bubbles. The superheated bubble has its own instability which then produces vapour explosion [81, 82]. Adding electrostatic effects on it should enhance the vapour explosion in the way that the impurity deposition should be rapid and more localized at a certain position. To confirm this, we may use DTOKS to simulate metallic dust in the time dependent plasma profiles, which includes ELMs' physical model, and the physics of the electrostatic disintegration of a charged bubble in a plasma.

(adding after the PhD viva to the first paragraph in chapter 7 as agreed with the examiners.)

Furthermore, lithium inner-surfaces have been recently tested for reducing wall recycling and improving tokamak confinement. Introducing lithium into the tokamak chamber can be achieved by using liquid lithium surfaces [85–89] and wall conditioning by artificial lithium dust injection [90–92]. As a result, an increase in the amount of lithium droplets in the chamber is expected because the melting temperature of lithium is relatively low. To understand the motion of lithium droplets and the appropriate plasma condition re-

quired for lithium-dust wall conditioning in a tokamak, we can perform a computational dust simulation by the use of the improved DTOKS with misty plasma physics.

Bibliography

[1] Paméla, Matthews, G.F., Philipps, V., Kamendje, R. & JET-EFDA Contributors. (2007) An ITER-like wall for JET. *Journal of Nuclear Materials*, 363-365, 1-11.

[2] Matthews, G.F., Edwards, P., Greuner, H., Loving, A., Maier, H., Mertens, Ph., Philipps, V., Riccardo, V., Rubel, M., Ruset, C., Scmidt, A., Villedieu, E. & JET-EFDA contributors to the ITER-like Wall Project. (2009) Current status of the JET ITER-like Wall Project. *Physica Scripta*, T138, 014030.

[3] Matthews, G.F., Beurskens, M., Brezinsek, S., Groth, M., Joffrin, E., Loving, A., Kear, M., Mayoral, M.-L., Neu, R., Prior, P., Riccardo, V., Rimini, F., Rubel, M., Sips, G., Villedieu, E., de Vries, P., Watkins, M.L. & EFDA-JET contributors. (2011) JET ITER-like wall—overview and experimental programme. *Physica Scripta*, T145, 014001.

[4] Gruber, O., Sips, A.C.C., Dux, R., Eich, T., Fuchs, J.C., Herrmann, A., Kallenbach, A., Maggi, C.F., Neu, R., Pütterich, T., Schweinzer, J., Stober, J. & the ASDEX Upgrade Team. (2009) Compatibility of ITER scenarios with full tungsten in ASDEX Upgrade. *Nuclear Fusion*, 49, 115014.

[5] Endstrasser, N., Rohde, V., Balden, M., Humrickhouse, P., von Toussaint, U., Braams, B.J., Chung, H.-K., Neu, R. & the ASDEX Upgrade team. (2011) Comparative study of the dust particle population sampled during four consecutive campaigns in full-tungsten ASDEX Upgrade. *Physica Scripta*, T145, 014021.

[6] Neu, R., Kallenbach, A., Balden, M., Bobkov, V., Coenen, J.W., Drube, R., Dux, R., Greuner, H., Herrmann, A., Hobirk, J., Höhnle, H., Krieger, K., Kočan, M., Lang, P., Luni, T., Maier, H., Mayer, M., Müller, H.W., Potzel, S., Pütterich, T., Rapp, J.,

Rohde, V., Ryter, F., Schneider, P.A., Schweinzer, J., Sertoli, M., Stober, J., Suttrop, W., Sugiyama, K., van Rooij, G., Wischmeier, M. & ASDEX Upgrade Team. (2013) Overview on plasma operation with a full tungsten wall in ASDEX Upgrade. *Journal of Nuclear Materials*, 438,S34-S41.

[7] Grosman, A., Bucalossi, J., Doceul, L., Escourbiac, F., Lipa, M., Merola, M., Missirlian, M., Pitts, R.A., Samaille, F. & Tsitrone, E. (2013) The WEST programme: Minimizing technology and operational risks of a full actively cooled tungsten divertor on ITER. *Fusion Engineering and Design*, 88, 497-500.

[8] Doceul, L., Bucalossi, J., Larroque, S., Lipa, M., Portafaix, C., Saille, A., Samaille, F., Soler, B., Ferlay, F. & Verger, J.M. (2013) Design, integration and feasibility studies of the Tore-Supra West divertor structure. *Fusion Engineering and Design*, 88, 814-817.

[9] Martin, J.D., Coppins, M. & Counsell, G.F. (2005) Motion and lifetime of dust grains in a tokamak plasma. *Journal of Nuclear Materials*, 337-339, 114-118.

[10] Martin, J.D., Bacharis, M., Coppins, M., Counsell, G.F. & Allen, J.E. (2008) Modelling dust transport in tokamaks. *Europhysics Letters*, 83, 65001.

[11] Bacharis, M., Coppins, M. & Allen, J.E. (2010) Dust in tokamaks: An overview of the physical model of the dust in tokamaks code. *Physics of Plasmas*, 17, 042505.

[12] Bacharis, M., Coppins, M. & Allen, J.E. (2010) Critical issues for modeling dust transport in tokamaks. *Physical Review E*, 82, 026403.

[13] Bacharis, M., Coppins, M., Fundamenski, W. & Allen, J.E. (2012) Modelling of tungsten and beryllium dust in ITER. *Plasma Physics and Controlled Fusion*, 54, 085010.

[14] Wesson, J. (1997) *Tokamaks*. Oxford Engineering Science Series - 48, 2nd edition, New York, Oxford University Press.

[15] Federici, G., Skinner, C.H., Brooks, J.N., Coad, J.P., Grisolia, C., Haasz, A.A., Hassanein, A., Philipps, V., Pitcher, C.S., Roth, J., Wampler, W.R. & Whyte, D.G. (2001) Plasma-material interactions in current tokamaks and their implications for next step fusion reactors. *Nuclear Fusion*, 41, 1967-2137.

[16] Nakamura, K., Suzuki, S., Tanabe, T., Dairaku, M., Yokoyama, K., & Akiba, M. (1998) Disruption erosions of the various kinds of tungsten. *Fusion Engineering and Design*, 39-40, 295-301.

[17] Stangeby, P.C. (2000) *The Plasma Boundary of Magnetic Fusion Devices*. Bristol, Institute of Physics Publishing.

[18] Herrmann, A., Balden, M., Laux, M., Krieger, K., Müller, H.W., Pugno, R., Rohde, V. & ASDEX Upgrade team. (2009) Arcing in ASDEX Upgrade with a tungsten first wall. *Journal of Nuclear Materials*, 390-391, 747-750.

[19] Rohde, V., Endstrasser, N., Toussaint, U.v., Balden, M., Lunt, T., Neu, R., Hakola, A., Bucalossi, J. & ASDEX Upgrade Team. (2011) Tungsten erosion by arcs in ASDEX upgrade. *Journal of Nuclear Materials*, 415, 546-550.

[20] Rohde, V., Balden, M., Endstrasser, N., von Toussaint, U. & ASDEX Upgrade Team. (2013) Arc erosion on W plasma facing components in ASDEX Upgrade. *Journal of Nuclear Materials*, 438, S800-S804.

[21] Rudakov, D.L., Chrobak, C.P., Doerner, R.P., Krasheninnikov, Moyer, R.A., Umstadter, K.R., Wampler, W.R. & Wong, C.P.C. (2013) Arcing and its role in PFC erosion and dust production in DIII-D. *Journal of Nuclear Materials*, 438, S805-S808.

[22] Winter, J. (1998) Dust in fusion—experimental evidence, possible sources and consequences. *Plasma Physics and Controlled Fusion*, 40, 1201-1210.

[23] Linke, J., Rubel, M., Malmberg, J.A., Drake, J.R., Duwe, R., Penkalla, H.J., Rödig, M., & Wessel, E. (2001) Carbon particles emssion, brittle destruction and co-deposit formation: experience from electron beam experiments and controlled fusion devices. *Physica Scripta*, T91, 36-42.

[24] Linke, J., Akiba, M., Duwe, R., Lodato, A., Penkalla, H.-J., Rödig, M. & Schöpflin, K. (2001) Material degradation and particle formation under transient thermal loads. *Journal of Nuclear Materials*, 290-293, 1102-1106.

[25] Winter, J. & Gebauer, G. (1999) Dust in magnetic confinement fusion devices and its impact on plasma operation. *Journal of Nuclear Materials*, 266-269, 228-233.

[26] Winter, J. (2000) Dust: A new challange in nuclear fusion research? *Physics of Plasmas*, 7, 3862-3866.

[27] Rohde, V., Balden, M., Lunt, T. & the ASDEX Upgrade Team. (2009) Dust investigations at ASDEX Upgrade. *Physica Scripta*, T138, 014024.

[28] Pestchanyi, S., Garkusha, I., Makhlaj, V. & Landman, I. (2011) Estimation of the dust production rate from the tungsten armour after repetitive ELM-like heat loads. *Physica Scripta*, T145, 014062.

[29] Sharpe, J.P., Rohde, V., The ASDEX-Upgrade Experiment Team, Sagara, A., Suzuki, H., Komori, A., Motojima, O. & The LHD Experimental Group. (2003) Characterization of dust collected from ASDEX-Upgrade and LHD. *Journal of Nuclear Materials*, 313-316, 455-459.

[30] Smolik, G.R., Merrill, B.J. & Wallace, R.S. (1992) Implications of beryllium : steam interactions in fusion reactors. *Journal of Nuclear Materials*, 191-194, 153-157.

[31] Sharpe, J.P., Petti, D.A. & Bartels, H.-W. (2002) A review of dust in fusion devices: Implications for safety and operational performance. *Fusion Engineering and Design*, 63-64, 153-163.

[32] Andrew, P., Brennan, P.D., Coad, J.P., Ehrenberg, J., Gadeberg, M., Gibson, A., Hillis, D.L., How, J., Jarvis, O.N., Jensen, H., Lässer, R., Marcus, F., Monk, R., Morgan, P., Orchard, J., Peacock, A., Pearce, R., Pick, M., Rossi, A., Schild, P., Schunke, B. & Stork, D. (1999) Tritium retention and clean-up in JET. *Fusion Engineering and Design*, 47, 233-245.

[33] Maddaluno, G., Giacomi, G., Rufoloni, A. & Verdini, L. (2007) Deuterium retention and surface modification of tungsten macrobrush samples exposed in FTU tokamak. *Journal of Nuclear Materials*, 363-365, 1236-1240.

[34] Skinner, C.H. & Federici, G. (2006) Is carbon a realistic choice for ITER's divertor? *Physica Scripta*, T124, 18-22.

[35] Ivanova, D., Rubel, M., Philipps, V., Freisinger, M., Huang, Z., Penkalla, H., Schweer, B., Sergienko, G., Sundelin, P. & Wessel, E. (2009) Survey of dust formed in the TEXTOR tokamak: structure and fuel retention. *Physica Scripta*, T138, 014025.

[36] Tanaka, Y., Smirnov, R.D., Pigarov, A.Yu., Takenaga, H., Asakura, N., Uesugi, Y. & Ohno, N. (2011) Simulation of dynamics of carbon dust particles in the JT-60U tokamak. *Journal of Nuclear Materials*, 415, S1106-S1110.

[37] Krasheninnikov, S.I., Smirnov, R.D. & Rudakov, D.I. (2011) Dust in magnetic fusion devices. *Plasma Physics and Controlled Fusions*, 53, 083001.

[38] Allen, J.E. (1992) Probe theory - the oribital motion approach. *Physica Scripta*, 45, 497-503.

[39] Kennedy, R.V. & Allen, J.E. (2003) The floating potential of spherical probes and dust grains. II: Orbital motion theory. *Journal of Plasma Physics*, 69(6), 485-506.

[40] Shukla, P.K. & Mamun, A.A. (2002) *Introduction to Dusty Plasma Physics*. Bristol, Institute of Physics Publishing.

[41] Willis, C.T.N., Coppins, M., Bacharis, M. & Allen, J.E. (2010) The effect of dust grain size on the floating potential of dust in a collisionless plasma. *Plasma Sources Science and Technology*, 19, 065022.

[42] Willis, C.T.N., Coppins, M., Bacharis, M. & Allen, J.E. (2012) Floating potential of large dust grains in a collisionless flowing plasma. *Physical Review E*, 85, 036403.

[43] Hoffman, J.D. (2001) *Numerical Methods for Engineers and Scientists*. 2nd edition, New York, Marcel Dekker.

[44] Castaldo, C., Ratynskaia, S., Pericoli, V., de Angelis, U., Rypdal, K., Pieroni, L., Giovannozzi, E., Maddaluno, G., Marmolino, C., Rufoloni, A., Tuccillo, A., Kretschmer, M. & Morfill, G.E. (2007) Diagnostics of fast dust perticles in tokamak edge plasmas. *Nuclear Fusion*, 47, L5-L9.

[45] Ratynskaia, S., Castaldo, C., Rypdal, K., Morfill, G., de Angelis, U., Pericoli-Ridolfini, V., Rufoloni, A. & Giovannozzi, E. (2008) Hypervelocity dust impacts in FTU scrape-off layer. *Nuclear Fusion*, 48, 015006.

[46] Morfill, G., Räth, C., Li, Y.-F., Hu, J.S., Ling, B.L., Gao, X. & Horányi, M. (2009) Dust capture experiment in HT-7. *New Journal of Physics*, 11, 113041.

[47] Tang, M., Hu, J.S., Li, J.G., Li, Y.-F., Morfill, G. & Ashikawa, N. (2011) Recent researches on dust in EAST and HT-7 tokamaks. *Journal of Nuclear Materials*, 415, S1094-S1097.

[48] Proverbio, L.I., Lazzaro, E., Ratynskaia, S., Castaldo, C., de Angelis, U., Grosso, G. & De Angeli, M. (2011) The dynamics of ferromagnetic dust particles in the FTU tokamak. *Plasma Physics and Controlled Fusion*, 53, 115013.

[49] Zagorski, R., Romanelli, F. & Pieroni, L. (1996) A self-consistent analysis of the impurity dynamics on the FTU tokamak. *Nuclear Fusion*, 36, 873-880.

[50] Lazzaro, E., Private Communications.

[51] Chapman, I.T., Hender, T.C., Saarelma, S., Sharapov, S.E., Akers, R.J., Conway, N.J. & the MAST team. (2006) The effect of toroidal plasma rotation on sawteeth in MAST. *Nuclear Fusion*, 46, 1009-1016.

[52] Chappuis, Ph., Tsitrone, E., Mayne, M., Armand, X., Linke, H., Bolt, H., Petti, D. & Sharpe, J.P. (2001) Dust characterization and analysis in Tore-Supra. *Journal of Nuclear Materials*, 290-293, 245-249.

[53] Lord Rayleigh (1882) On the equlibrium of liquid conducting masses charged with electricity. *Philosophical Magazine*, 14, 184-186.

[54] Coppins, M. (2010) Electrostatic breakup in a misty plasma. *Physical Review Letters*, 104, 065003.

[55] Taylor, G. (1964) Disintegration of water drops in an electric field. *Proceedings of the Royal Society of London. Series A, Mathematical and Physical Sciences*, 280, 383-397.

[56] Duft, D., Lebius, H., Huber, B.A., Guet, C. & Leisner, T. (2002) Shape oscillations and stability of charged microdroplets. *Physical Review Letters*, 89(8), 084503.

[57] Duft, D., Achtzehn, T., Müller, R., Huber, B.A. & Leisner, T. (2003) Rayleigh jets from levitated microdroplets. *Nature*, 421, 128.

[58] Lord Rayleigh (1879) On the capillary phenomena of jets. *Proceedings of the Royal Society of London*, XXIX, 71-97.

[59] J.W.S., Baron Rayleigh (1945) *The Theory of Sound Vol. 2.* 2nd edition, New York, Dover Publications; London, Constable and Company.

[60] Hendricks, C.D. & Schneider, J.M. (1963) Stability of a conducting droplet under the influence of surface tension and electrostatic forces. *American Journal of Physics*, 31, 450-453.

[61] Peters, J.M.H. (1980) Rayleigh's electrified water drops. *European Journal of Physics*, 1, 143-146.

[62] Landau, L.D. & Lifshitz, E.M. (2004) *Fluid Mechanics.* Course of theoretical physics vol. 6, 2nd edition, Amsterdam, Elsevier/Butterworth-Heinemann.

[63] Jackson, J.D. (1999) *Classical Electrodynamics.* 3rd edition, New York, John Wiley & Sons.

[64] Taylor, J.R. (2005) *Classical Mechanics.* Sausalito, California, University Science Books.

[65] Achtzehn, T., Müller, R., Duft, D. & Leisner, T. (2005) The coulomb instability of charged microdroplets: Dynamics and scaling. *The European Physical Journal D*, 34, 311-313.

[66] Giglio, E., Gervais, J., Rangama, J., Manil, B., Huber, B. A., Duft, D., Müller, R., Leisner, T. & Guet, C. (2008) Shape deformations of surface-charged microdroplets. *Physical Review E*, 77, 036319.

[67] Coppins, M., Private Communications.

[68] Frohn, A. & Roth, N. (2000) *Dynamics of Droplets.* Berlin and London, Spinger.

[69] Adam, N.K. (1941) *The Physics and Chemistry of Surfaces.* 3rd edition, London, Oxford University Press.

[70] Defay, R. & Prigogine, I. (1966) *Surface Tension and Adsorption.* Longmans.

[71] Kočan, M., Genrich, F.P., Kendl, A., Müller, H.W. & the ASDEX Upgrade Team. (2012) Ion temperature fluctuations in the ASDEX Upgrade scrape-off layer. *Plasma Physics and Controlled Fusion*, 54, 085009.

[72] Keene, B.J. (1993) Review of data for the surface tension of pure metals. *International Materials Reviews*, 38(4), 157-192.

[73] Kingery, W.D. (1959) Surface tension of some liquid oxides and their temperature coefficients. *Journal of the American Ceramic Society*, 42(1), 6-10.

[74] Haynes, W.M., Lide, D.R. 1928- & Bruno, T.J. (2012) *CRC Handbook of Chemistry and Physics: A Ready-reference Book of Chemical and Physical Data*. 93rd edition (2012-2013), London, Boca Raton Fla.

[75] Heimann, R.B. (2008) *Plasma Spray Coating: Principles and Applications* 2nd edition, Weinheim, Wiley-Vch.

[76] Schütze, A., Jeong, J.Y., Babayan, S.E., Selwyn,, G.S. & Hicks, R.F. (1998) The atmospheric-pressure plasma jet: A review and comparison to other plasma sources. *IEEE Transactions on Plasma Science*, 26(6), 1685-1694.

[77] Pfender, E. (1988) Fundamental studies associated with the plasma spray process. *Surface and Coatings Technology*, 34, 1-14.

[78] Kim, H.J. & Hong, S.H. (1995) Comparative measurements on thermal plasma jet characteristics in atmospheric and low pressure plasma sprayings. *IEEE Transactions on Plasma Science*, 23(5), 852-859.

[79] Somboonkittichai, N. (2012) *Pressure of liquid metal droplets in tokamak plasmas, July 2-6, 2012, Stockholm, Sweden*. The 39$^{\text{th}}$ European Physical Society (EPS) Conference on Plasma Physics and the 16$^{\text{th}}$ International Congress on Plasma Physics.

[80] Allen, J.E. & Coppins, M., Private Communications.

[81] Shepherd, J.E. & Sturtevant, B. (1982) Rapid evaporation at the superheat limit. *Journal of Fluid Mechanics*, 121, 379-402.

[82] Park, H.-C., Byun, K.-T. & Kwak, H.-Y. (2005) Explosive boiling of liquid droplets at their superheat limits. *Chemical Engineering Science*, 60, 1809-1821.

[83] Tempere, J., Silvera, I.F. & Devreese, J.T. (2001) Effect of pressure on statics, dynamics, and stability of multielectron bubbles. *Physical Review Letters*, 87(27), 275301.

[84] Shukla, P.K. & Eliasson, B. (2009) *Colloquium*: Fundamentals of dust-plasma interactions. *Reviews of Modern Physics*, 81, 25-44.

(adding after the PhD viva as agreed with the examiners.)

[85] Evtikhin, V.A., Lyublinski, I.E., Vertkov, A.V., Mirnov, S.V., Lazarev, V.B., Petrova, N.P., Sotnikov, S.M., Chernobai, A.P., Khripunov, B.I., Petrov, V.B., Prokhorov, D.Yu. & Korzhavin, V.M. (2002) Lithium divertor concept and results of supporting experiments. *Plasma Physics and Controlled Fusion*, 44, 955-977.

[86] Mirnov, S.V., Azizov, E.A., Evtikhin, V.A., Lazarev, V.B., Lyublinski, I.E., Vertkov, A.V. & Prokhorov, D.Yu. (2006) Experiments with lithium limiter on T-11M tokamak and applications of the lithium capillary-pore system in future fusion reactor devices. *Plasma Physics and Controlled Fusion*, 48, 821-837.

[87] Mirnov, S. (2009) Plasma-wall interactions and plasma behavior in fusion devices with liquid lithium plasma facing components. *Journal of Nuclear Materials*, 390-391, 876-885.

[88] Majeski, R., Berzak, L., Gray, T., Kaita, R., Kozub, T., Levinton, F., Lundberg, D.P., Manickam, J., Pereverzev, G.V., Snieckus, K., Soukhanovskii, V., Spaleta, J., Stotler, D., Strickler, T., Timberlake, J., Yoo, J. & Zakharov, L. (2009) Performance projections for the lithium tokamak experiment (LTX). *Nuclear Fusion*, 49, 055014.

[89] Ren, J., Hu, J.S., Zuo, G.Z., Sun, Z., Li, J.G., Ruzic, D.N. & Zakharov, L.E. (2014) First results of flowing liquid lithium limiter in HT-7. *Physica Scripta*, T159, 014033.

[90] Kuteev, B.V., Sergeev, V.Yu., Krylov, S.V., Skokov, V.G. & Timokhin, V.M. (2010) Conceptual analysis of a tokamak reactor with lithium dust jet. *Nuclear Fusion*, 50, 075001.

[91] Kuteev, B.V., Sergeev, V.Yu., Timokhin, V.M., Skokov, V.G., Krylov, S.V., Bykov, A.S., Notkin, G.E., Kislov, A.Ya., Tilinin, G.T. & Petrov, V.S. (2011) Dust technologies for magnetic fusion. *Journal of Nuclear Materials*, 415, S1073-S1076.

[92] Sergeev, V.Yu., Kuteev, B.V., Bykov, A.S., Krylov, S.V., Skokov, V.G. & Timokhin, V.M. (2012) Lithium technologies for edge plasma control. *Fusion Engineering and Design*, 87, 1765-1769.

Appendix A

Symbols

ϕ_d	a floating potential on a dust grain or a liquid droplet in V.
r_d	a dust or a droplet radius in m.
T_i	an ion temperature of a plasma in K and $T_i[eV]$ in eV.
T_e	an electron temperature of a plasma in K and $T_e[eV]$ in eV.
T	a temperature in K or $T[eV]$ in eV.
T_d	a dust temperature in K.
β	the ratio between an ion and an electron temperatures of a plasma, $\frac{T_i}{T_e}$.
Φ_d	a ratio between ϕ_d and T_e $(= -\frac{e\phi_d}{kT_e})$.
$\hat{\Phi}_d$	a ratio between ϕ_d and T_i $(= -\frac{e\phi_d}{kT_i} = \frac{\Phi_d}{\beta})$.
k	a Boltzmann constant.
n_i	an ion number density of a plasma in m^{-3}.
n_e	an electron number density of a plasma in m^{-3}.
n	a number density in m^{-3}.
$n_{i,0}$	a faraway ion number density, unperturbed by a dust floating potential, ϕ_d, in m^{-3}.
$n_{e,0}$	a faraway electron number density, unperturbed by a dust floating potential, ϕ_d, in m^{-3}.
m_i	a single ion mass in kg.
m_e	a single electron mass in kg.
m_p	a single proton mass in kg.
λ_D	a debye length of a plasma in m.
A,	atomic mass number.

γ	a ratio of specific heat capacity used in MOML, which equal $\frac{5}{3}$.
$r_{d,min}$	a minimum size in radius of a liquid droplet where electrostatic breakup initiates in m.
$r_{d,crit}$	a critical size in radius of a bubble where electrostatic breakup initiates in m.
Q, q	charges in C.
Q_d	a dust or a droplet charges in C.
ε_0	the permittivity of free space.
R	an unperturbed or an original droplet radius in m.
σ	a surface tension in N/m.
r	a perturbed droplet radius or an arbitrary radius in m, a radial cooridinate in a spherical coordinate system or a tokamak minor radius of a position (in m).
θ	a polar coordinate in a spherical coordinate system.
ϕ	an azimuthal coordinate in a spherical coordinate system.
P_ℓ	The ℓ^{th}-order of Legendre polynomials.
ξ_ℓ	a magnitude of the ℓ^{th} mode perturbation controlled by Legendre polynomials.
$\mathbf{v}$	a velocity vector in m/s.
ϕ_v	a velocity potential.
m	a mass in kg.
V	a volume in m^3.
ρ	a mass density in kg/m^3.
$\mathbf{E}$	an electric field.
ϕ_E	an electrostatic potential in V.
Δ(KE)	a total change in a kinetic energy.
Δ(PE)	a total change in a potential energy.
$\mathcal{L}$	a Lagrangian ($= \Delta(\text{KE}) - \Delta(\text{PE})$).
ω	an angular frequancy of a surface wave.
C	a capacitance.
Γ	a particle flux.
Γ_r	the radial component of a particle flux.
e	an elementrary charge in C.

v	a total magnitude of a velocity or a speed in m/s.
$\mathbf{v_d}$	a dust velocity vector.
P	a pressure in Pa.
P_{liq}	a liquid pressure in Pa.
P_{vap}	a vapour pressure in Pa.
P_i	an ion pressure in Pa.
Γ_i	a net ion momentum flux or pressure which results from the sum of ion thermal pressure (P_i) and ion dynamic pressure.
P_e	an electron pressure in Pa.
P_r	a pressure due to neutral recombination in Pa.
P_{st}	a pressure due to a surface tension in Pa.
P_{es}	an electrostatic pressure in Pa.
$P_{inwards}$	a total inwards pressure.
$P_{outwards}$	a total outwards pressure.
$\Gamma_{p,i}$	a net ion momentum flux or pressure which results from the sum of ion thermal pressure and ion dynamic pressure.
λ_D	a (electron) Debye length.
α	a surface charge density in C/m^2.
$\bar{c}_e$	an electron thermal speed $\left(= \sqrt{\frac{8kT_e}{\pi m_e}}\right)$.
$\bar{c}$	a thermal speed $\left(= \sqrt{\frac{8kT}{\pi m}}\right)$
Q_{net}	a net energy on a dust grain.
Ξ_{net}	a net energy flux on a dust grain.
m_d	a mass of a dust grain in kg.
ρ_d	a dust material density in kg/m^3.
c	a specific heat capacity.
$\mathbf{B}$	a magnetic field.
$\mathbf{g}$	a gravitational acceleration in m/s^2.
$\mathbf{F_{id}}$	a net ion drag force.
$\mathbf{F_{id,s}}$	a scattered ion drag force.
$\mathbf{F_{id,c}}$	a collected ion drag force.

A_{cs}	the OML cross-section area.
L_v	a latent heat of vaporization.
R_0	a major radius of a tokamak in m.
r_w	a minor radius of the wall position in m.
r_a	a minor radius of the LCMS position in m.
r_0	a minor radius of zero electric field in m.
λ_T	a temperature decay length.
λ_n	a number density decay length.
E	a magnitude of an electric field in V/m.
B	a magnitude of a magnetic field in T.
ϵ_n	the coefficient of normal restitution.
ϵ	the coefficient of isotropic restitution.
$v_\perp$	a normal component of a velocity in m/s.
T_0	a central plasma temperature in eV.
T_a	an LCMS plasma temperature in eV.
n_0	a central plasma number density in m^{-3}.
n_a	an LCMS plasma number density in m^{-3}.
B_0	a central toroidal magnetic field in T.
B_a	an LCMS poloidal magnetic field in T.
E_0	a peak value of a radial electric field in a core plasma in V/m.
E_a	a peak value of a radial electric field in a SOL plasma in V/m.
$v_{p,\phi}$	the toroidal component of a plasma flow speed.
r^*	a velocity drop-point position.
ζ_a	$\frac{r}{r_a}$.
ζ	$\frac{r}{r_w}$.
ζ_0	$\frac{r}{r_0}$.
Q_{max}	a maximum charge initiated electrostatic breakup.
W_{ext}	a work done by all external pressures.
T_{boil}	a boiling temperature.
η	a launching direction.

Appendix B

Abbreviations

MCF	Magnetically confined fusion.
LCMS	Last closed magnetic surface, the edge of confined plasma in an MCF tokamak.
SOL	Scrape-off layer, outwardly beyond LCMS.
OML	Orbital motion limited.
MOML	Modified orbital motion limited.
MLE	Modified Laplace equation, a pressure balance eqaution.
ELMs	Edge localized modes instability.
DTOKS	Dust transport code developed at Imperial College London.
THE	Thermionic electron emission.
SEE	Secondary electron emssion.
COR	Coefficient of restitution.
LHS	Left-hand side.
RHS	Right-hand side.